From the holdings of the Department of Special Collections , Princeton University Library, Princeton, NJ

These documents are either in the public domain, or can only be used for educational and research purposes (Fair use) as per U.S. Copyright law (text below). By accessing this file, all users agree that their use falls in the public domain or within fair use as defined by the copyrightlaw. We do not charge any permission or usage fees for the publication of images of material inour collections, including those provided by Princeton University Library, via our website, catalog, or directly from staff.For more information regarding copyright, credit, and citation please review the information onthe Copyright, Credit and Citation Guidelines page of our website.
https://library.princeton.edu/special-collections/policies/copyright-credit-and-citation-guidelines. If you have any questions, including how to order higher-quality images from the collection, contact Special Collections Public Services via our Ask Us! Form. https://library.princeton.edu/special-collections/ask-us

---

Doctoral Dissertations, 2011-2026 Astrophysical Sciences

2014

Electromagnetic and Radiative Properties of Neutron Star Magnetospheres

Li, Jason G.

Princeton, NJ : Princeton University

---

http://arks.princeton.edu/ark:/88435/dsp01mp48sc90j

U.S. Copyright law: The copyright law of the United States (Title 17, §108, United States Code) governs the making of photocopies or other reproductions of copyrighted material. Under certain conditions specified in the law, libraries and archives are authorized to furnish a photocopy or other reproduction. One of these specified conditions is that the photocopy or reproduction is not to be used for any purpose other than private study, scholarship, or research. If a user makes a request for, or later uses, a photocopy or reproduction for purposes in excess of fair use that user may be liable for copyright infringement. This institution reserves the right to refuse to accept a copying order if, in its judgment, fulfillment of the order would involve a violation of copyright law. https://www.copyright.gov/title17/title17.pdf

Electromagnetic and Radiative Properties of Neutron Star Magnetospheres

Jason G. Li

A Dissertation
Presented to the Faculty
of Princeton University
in Candidacy for the Degree
of Doctor of Philosophy

Recommended for Acceptance
by the Department of
Astrophysical Sciences

Adviser: Anatoly Spitkovsky

January 2014

© Copyright by Jason G. Li, 2014.

All rights reserved.

I certify that I have read this thesis and that in my opinion it is fully adequate, in scope and in quality, as a dissertation for the degree of Doctor of Philosophy.

Anatoly Spitkovsky
(Adviser)

I certify that I have read this thesis and that in my opinion it is fully adequate, in scope and in quality, as a dissertation for the degree of Doctor of Philosophy.

Roman Rafikov

I certify that I have read this thesis and that in my opinion it is fully adequate, in scope and in quality, as a dissertation for the degree of Doctor of Philosophy.

James Stone

Approved for the Princeton University Graduate School:

Dean of the Graduate School

Man can do all things if he will

- LEON BATTISTA ALBERTI

Abstract

Magnetospheres of neutron stars are commonly modeled as either devoid of plasma in "vacuum" models or filled with perfectly conducting plasma with negligible inertia in "force-free" models. While numerically tractable, neither of these idealized limits can simultaneously account for both the plasma currents and the accelerating electric fields that are needed to explain the morphology and spectra of high-energy emission from pulsars. In this work we improve upon these models by considering the structure of magnetospheres filled with resistive plasma. We formulate Ohm's Law in the minimal velocity fluid frame and implement a time-dependent numerical code to construct a family of resistive solutions that smoothly bridges the gap between the vacuum and force-free magnetosphere solutions. We further apply our method to create a self-consistent model for the recently discovered intermittent pulsars that switch between two distinct states: an "on", radio-loud state, and an "off", radio-quiet state with lower spin-down luminosity. Essentially, we allow plasma to leak off open field lines in the absence of pair production in the "off" state, reproducing observed differences in spin-down rates. Next, we examine models in which the high-energy emission from gamma-ray pulsars comes from reconnecting current sheets and layers near and beyond the light cylinder. The reconnected magnetic field provides a reservoir of energy that heats particles and can power high-energy synchrotron radiation. Emitting particles confined to the sheet naturally result in a strong caustic on the skymap and double peaked light curves for a broad range of observer angles. Interpulse bridge emission likely arises from interior to the light cylinder, along last open field lines that traverse the space between the polar caps and the current sheet. Finally, we apply our code to solve for the magnetospheric structure of merging neutron star binaries. We find that the scaling of electromagnetic luminosity with orbital angular velocity varies between the power 4 for nonspinning stars and the power 1.5 for rapidly spinning millisecond pulsars near contact. Our derived scalings and magnetospheres can be used to help

understand electromagnetic signatures from merging neutron stars to be observed by Advanced LIGO.

Acknowledgments

It is my pleasure to thank my adviser, Anatoly Spitkovsky, for teaching me how to attack interesting unsolved problems in astrophysics. I would also like to thank all of the professors, postdoctoral fellows, and students in Princeton and elsewhere that I have collaborated with or interacted with over the past five years, including Sasha Tchekhovskoy, Jerry Ostriker, Jeremy Goodman, Jim Stone, Roman Rafikov, Yan-Fei Jiang, Xue-Ning Bai, and many others. Next, I would like to thank the staff in Peyton Hall and at the PICSciE-OIT TIGRESS High Performance Computing Center and Visualization Laboratory for their assistance. Last but not least, I would like to thank my family, including my parents Jane and Guanghai, and brothers Timmy and Randy, and friends, for their support over the years.

Contents

Abstract **v**

Acknowledgments **vii**

1 Introduction **1**

1 Observations 1

2 Magnetosphere Cartoons 3

3 Plasma Supply 6

4 Numerical Method 8

5 Applications 10

Bibliography 11

2 Resistive Solutions for Pulsar Magnetospheres **14**

1 Introduction 14

2 Resistive Electrodynamics 15

2.1 Resistive Current Derivation 18

3 Numerical Simulations 21

3.1 Numerical effects on spin-down power 33

4 Discussion 35

Bibliography 41

3 On the Spin-Down of Intermittent Pulsars **43**

1 Introduction 43

2 Setup 45

3 Results 47

4 Discussion . . . 52
Bibliography . . . 55

4 High-Energy Radiation from Current Sheets and Current Layers in Pulsar Magnetospheres 57

1 Introduction . . . 57
2 Numerics . . . 60
3 Current Sheet . . . 61
4 Particle Motion . . . 66
5 Toy Models of Current Sheet Emission . . . 69
5.1 Overview . . . 69
5.2 Light Cylinder Region . . . 71
5.3 Wind zone . . . 73
6 Current Layer . . . 75
7 Combined Current Layer and Current Sheet Skymaps . . . 77
8 Discussion . . . 80
Bibliography . . . 86

5 Electromagnetic Properties of Binary Neutron Star Magnetospheres 90

1 Introduction . . . 90
2 Setup . . . 91
3 Results . . . 94
3.1 2D Magnetosphere Illustrations . . . 94
3.2 3D Magnetosphere Illustrations . . . 99
3.3 Extended Magnetosphere Shape . . . 107
3.4 Electromagnetic Luminosity . . . 108
3.5 Luminosity Dependence on Inclination Angle . . . 120
3.6 Angular Dependence of Poynting Flux . . . 124
4 Discussion . . . 126

Bibliography 130

6 Conclusion **133**

Bibliography 136

List of Figures **137**

List of Tables **147**

Chapter 1

Introduction

1 Observations

Pulsars were first discovered as pulsating radio sources (Hewish et al., 1968) and soon afterwards associated with spinning magnetized neutron stars (Gold, 1968). Radio emission is thought to come from near the magnetic poles, and hence an appropriately oriented observer will see radio pulses at the frequency of the pulsar spin. Figure 1.1 shows light curves for 7 pulsars seen in radio through γ-rays. Radio emission processes are not well understood, in part because total energy output in radio bands is very small, and are beyond the scope of this thesis. The γ-ray emission can be quite significant, however, and represents a more tractable problem. It is particularly interesting at present because the Fermi γ-ray Space Telescope (GST) has recently discovered > 100 new γ-ray pulsars. Figure 1.2 gives characteristic light curves from the Vela pulsar in radio and a number of different γ-ray bands. Emission is strongly double peaked, with a small phase offset between the radio and first γ-ray peak, and bridge emission between the γ-ray peaks.

Periods have been measured for thousands of pulsars, and measurements are in fact precise enough to measure the time derivative of the periods. Figure 1.3 shows a $\mathrm{P} - \dot{\mathrm{P}}$ diagram for a large population of pulsars, with the period P on the horizontal axis and the time derivative of the period $\dot{\mathrm{P}}$ on the vertical axis. Ordinary pulsars with periods $\mathrm{P} \sim 1$ s cluster in the center of the diagram, and the recycled millisecond pulsars that are spun up by accretion inhabit the bottom left portion of the diagram. Ordinary pulsars are not observed in the bottom right portion of the diagram after they age past a death line, as the fields and rotation are no longer strong enough to generate the plasma that produces radio emission.

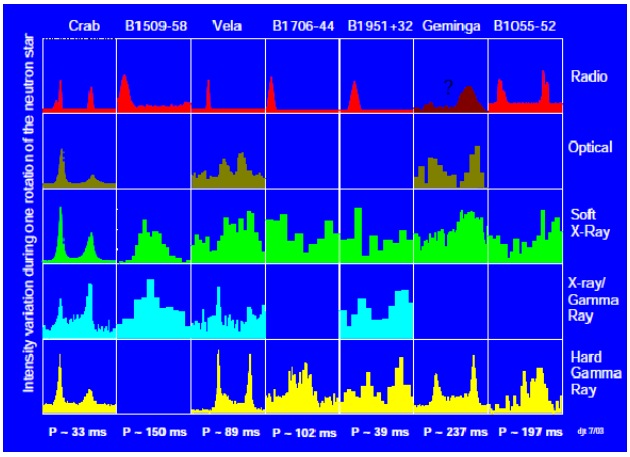

Figure 1.1: Light curves for 7 pulsars in radio through γ-rays. Image courtesy Thompson (2004).

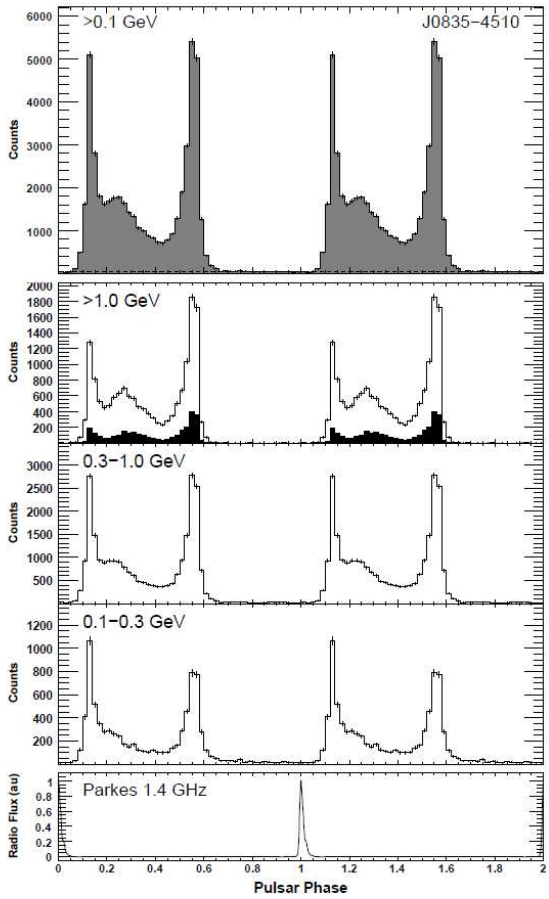

Figure 1.2: Radio and γ-ray light curves for the Vela pulsar from the Fermi GST (Abdo et al., 2010). γ-ray light curves have a characteristic double-peaked shape.

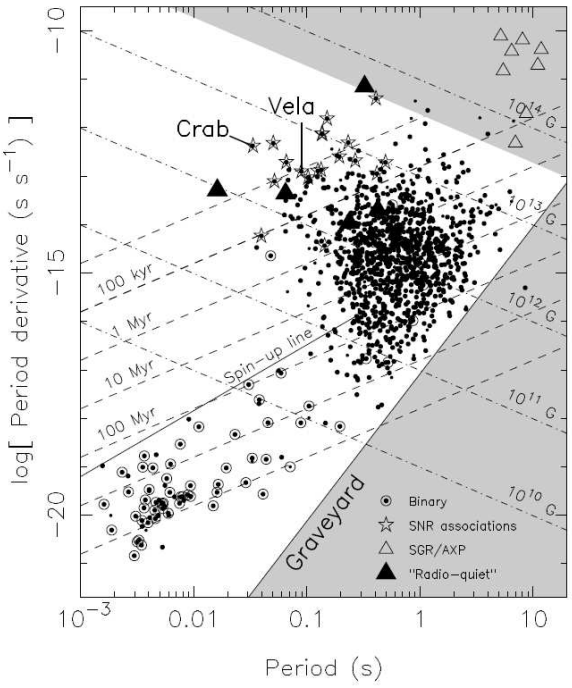

Figure 1.3: $P - \dot{P}$ diagram for a large population of ordinary and millisecond pulsars (Cordes et al., 2004).

2 Magnetosphere Cartoons

To first order, the magnetic field of the pulsar is a dipole, and the pulsar spins down due to magnetodipole radiation (Gunn & Ostriker, 1969). The dipole radiation has luminosity

$$L = \frac{2}{3}\frac{\mu^2\Omega^4}{c^3}\sin^2(\alpha), \tag{1.1}$$

where μ is the strength of the magnetic dipole, Ω is the angular velocity of the star, and α is the inclination angle between the rotation axis and the magnetic moment. This dipole radiation can be thought of as the ejection of toroidal magnetic field. Figure 1.4 shows magnetic field lines in the equatorial plane of an orthogonal rotator. There is an induced electric field out of the page, and an outward directed Poynting flux $\mathbf{S} = (c/4\pi)\mathbf{E} \times \mathbf{B}$ carrying off electromagnetic energy.

The real environment surrounding the pulsar, which is usually called the magnetosphere, has significant differences from this vacuum picture, however. The rotation of the pulsar induces

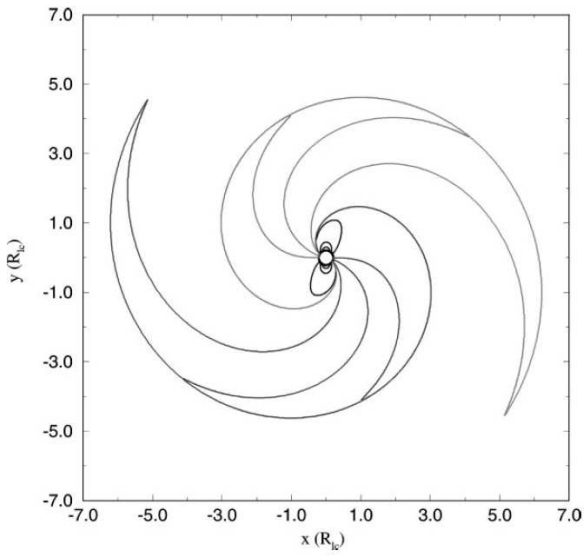

Figure 1.4: Vacuum magnetic fields in the equatorial plane of an orthogonal rotator (Michel & Li, 1999). The ejection of wound up toroidal field carries off electromagnetic energy.

strong electric fields that can strip particles off the stellar surface and accelerate them to ultrarelativistic velocities. These particles pair produce off the super-strong magnetic fields and populate the pulsar magnetospheres with abundant plasma. The standard cartoon of a magnetosphere filled with abundant plasma was first proposed by Goldreich & Julian (1969). In this picture the electric field is no longer the induction electric field in vacuum, but is rather the corotation electric field

$$\mathbf{E} = -\frac{1}{c}(\mathbf{\Omega} \times \mathbf{r}) \times \mathbf{B}. \tag{1.2}$$

The physical interpretation is that the abundant plasma is forced to corotate with the magnetic field lines as they sweep around with the pulsar. Figure 1.5 provides an illustration of the Goldreich-Julian model (see also Sturrock 1971). The closed magnetic field line region extends to the light cylinder $R_{\rm LC} = c/\Omega$, and field lines crossing the light cylinder open up to infinity. A large-scale poloidal current circuit forms, with electrons flowing out but current flowing in along open field lines, and current flowing out through an equatorial current sheet. From Gauss's Law it

follows that the Goldreich-Julian charge density is

$$\rho_{\rm GJ} = \frac{1}{4\pi}\nabla \cdot \mathbf{E} \approx -\mathbf{\Omega} \cdot \mathbf{B}/2\pi c, \tag{1.3}$$

where $\mathbf{B}$ is the dipole field. A null charge surface exists where $\mathbf{\Omega} \cdot \mathbf{B} = 0$, and separates net positively charged plasma near the equator from net negatively charged plasma near the poles. Charge carriers of both signs are produced by the pair cascade and are present throughout the magnetosphere, with multiplicity (Lyubarsky, 1995)

$$\kappa = ne/\rho_{\rm GJ} \approx 10^4, \tag{1.4}$$

where n is the plasma number density and e is the electron/positron charge. The energy density of the abundant plasma is still subdominant to the energy in magnetic fields, however. The ratio of the electromagnetic energy flux to the particle kinetic energy flux is (Lyubarsky, 1995)

$$\sigma_M = \frac{S}{n\gamma mc^3} \approx 10\frac{B_1}{10^{12}{\rm G}}\left(\frac{R_*}{10^6{\rm cm}}\right)^3\left(\frac{1{\rm s}}{\rm P}\right)^2, \tag{1.5}$$

where m is the mass of particles, γ their Lorentz factor, R_* is the neutron star radius, and B_1 the surface magnetic field strength. It is hence safe to ignore plasma inertia and pressure, and dynamics should be governed by the force-free equation,

$$\rho\mathbf{E} + \mathbf{j} \times \mathbf{B} = 0. \tag{1.6}$$

The Goldreich-Julian model is, strictly speaking, a cartoon, as the backreaction of plasma currents on the magnetic field structure are not included. It nevertheless remained a state-of-the-art model for three decades because of the difficulty of obtaining a self-consistent solution for the magnetospheric field structure satisfying equation 1.6. The full pulsar solution satisfying equation 1.6 was not developed until quite recently, by Contopoulos et al. (1999) in 2D,

and by Spitkovsky (2006) in 3D. We describe the plasma currents in force-free solutions in more detail in the following section.

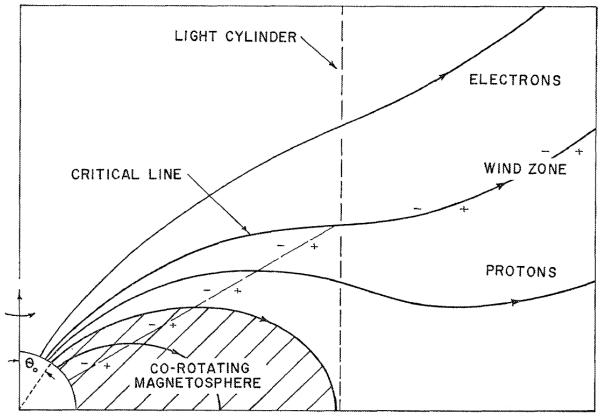

Figure 1.5: Goldreich-Julian model of a pulsar magnetosphere filled with abundant plasma (Goldreich & Julian, 1969). Field lines open up beyond the light cylinder, and the electric field is the corotation field.

3 Plasma Supply

The presence of plasma affects all magnetospheric properties. Although this fact has been well appreciated since the early days of pulsar research, the ability to quantitatively model plasma effects has emerged mainly in the last decade. Generally speaking, the models of pulsar magnetospheres can be classified according to the amount of plasma supply they assume. At one extreme is the vacuum magnetosphere, which is modeled with the magnetic field of a spinning inclined dipole in vacuum (Deutsch, 1955; Michel & Li, 1999). As this solution has no plasma, it has no possibility of producing any pulsar-like emission. However, the fact that this field is described by an analytic formula has made it the most widely used framework for calculating pulsar properties. For example, the characteristic spin-down energy loss which yielded the fiducial pulsar field strength of 10^{12}G or the polarization sweep of the rotating-vector model (Radhakrishnan & Cooke, 1969) are guided by the vacuum field shape. Slot-gap and outer gap models of gamma-ray emission from pulsars are also based on this field (Cheng et al., 1986; Dyks et al., 2004). The next order of approximation is models that allow plasma emission from the

surface of the star. These include the original charge-separated model of Goldreich & Julian (1969), and the space charge-limited models with pair formation (e.g., Ruderman & Sutherland, 1975; Arons & Scharlemann, 1979). These models envision both the regions where plasma shorts out the accelerating electric fields and the vacuum-like regions where acceleration is present (so-called "gaps"). This approach allows for more realism in studying plasma creation and acceleration, but at the price of being decoupled from the global structure of the magnetosphere, as the modification of the vacuum field due to plasma currents is typically not included. Finally, the models that concentrate on the global magnetospheric properties assume that abundant plasma exists throughout the magnetosphere and in the wind. This plasma shorts out the accelerating electric fields and provides the corotation of field lines with the star. Such models include the relativistic magnetohydrodynamic (MHD) description of the magnetosphere and its limit for low-inertia magnetically-dominated plasmas, the "force-free" description. Which of these different regimes is applicable to real pulsars may ultimately depend on the physics of plasma supply in the magnetosphere.

Previous to our work, quantitative solutions of the global magnetospheric structure existed only for the vacuum limit (Deutsch, 1955; Michel & Li, 1999) and for the limit of abundant plasma in force-free electrodynamics (see Contopoulos et al. 1999; Gruzinov 2005; Timokhin 2006; McKinney 2006; Parfrey et al. 2012; Palenzuela 2013 for aligned rotators, and Spitkovsky 2006; Kalapotharakos & Contopoulos 2009; Pétri 2012 for pulsars with arbitrary inclinations) or ideal magnetohydrodynamics (Komissarov 2006 in 2D; Tchekhovskoy et al. 2013 in 3D). Real pulsar magnetospheres likely combine elements from both limits, with regions of pair production and abundant plasma, but also various accelerating gaps and strong current sheets causing local violations of the ideal MHD constraint, $\mathbf{E} \cdot \mathbf{B} = 0$. Including such non-ideal effects into our understanding of the magnetosphere would significantly enhance our ability to calculate pulsar emission properties. In particular, the ideal force-free models that do include the effects of plasma currents on the magnetospheric field structure lack any accelerating fields by construction and thus cannot fully predict the morphology and spectra of high-energy emission from γ-ray pulsars.

One way to reintroduce accelerating electric fields in the magnetosphere is to allow finite resistivity of the plasma. Several formulations of resistive force-free equations have been proposed, most notably by Lyutikov (2003) and Gruzinov (2007, 2008). In resistive MHD, the Ohm's law can be unambiguously defined in the proper frame of the fluid by relating the current in that frame to the electric field through $\mathbf{j}_{\text{fluid}} = \sigma \mathbf{E}_{\text{fluid}}$, where σ is plasma conductivity (see, e.g., Lichnerowicz, 1967; Palenzuela et al., 2009). In the force-free system, however, the fluid velocity along the magnetic field is unknown, and only the transverse velocity can be obtained from the electromagnetic fields. This introduces some freedom in prescribing the Ohm's law in the force-free picture. In the prescription proposed by Lyutikov (2003), the parallel velocity along the field was taken to be zero and the method reduces to vacuum at low conductivity. In Strong-Field Electrodynamics (Gruzinov, 2007, 2008), the Ohm's law was formulated in the frame that moves along the field lines with such speed that the charge density in that frame vanishes. Despite the fact that such a frame formally exists only in space-like regions, the Strong-Field Electrodynamics prescription appears to give smooth numerical solutions throughout the magnetosphere (Gruzinov, 2011), and, most importantly, does not explode in current sheets where magnetic fields can go through zero. Both formulations are arbitrary, however, because the real fluid velocity does not have to follow either frame assumption. As an additional constraint, it is useful, therefore, to construct a resistive formulation that reproduces physical solutions expected at the extremes of very large and very small conductivity of the plasma, namely the force-free limit ($\sigma \to \infty$) and the limit of vacuum electromagnetism ($\sigma \to 0$). In this work we present a resistive prescription that generalizes these schemes and combines the correct limiting behavior of Lyutikov's scheme with the current sheet stability of Gruzinov's formulation. We then apply this prescription to numerically calculate the structure of resistive magnetospheres for pulsars.

4 Numerical Method

We employ a parallel three-dimensional numerical code (Spitkovsky, 2006) that implements the finite difference time-domain scheme (FDTD, Taflove & Hagness, 2005) to evolve electromagnetic

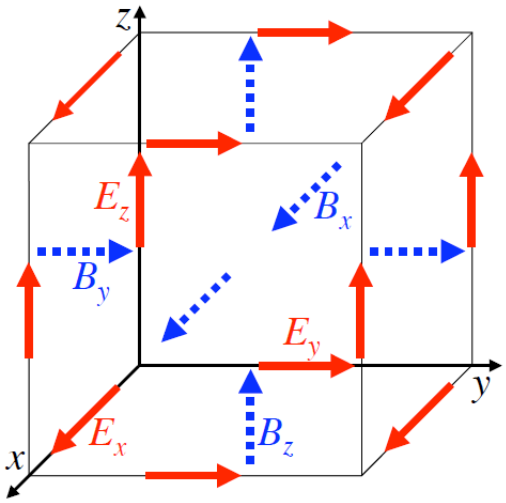

Figure 1.6: Cartesian Yee cell used in FDTD methods. **E** is defined on cell edges and and **B** on cell faces to simplify the calculation of numerical curls. Image courtesy Werner & Cary (2007).

fields from Maxwell's equations,

$$\partial_t \mathbf{E} = c\nabla \times \mathbf{B} - 4\pi \mathbf{j},$$
$$\partial_t \mathbf{B} = -c\nabla \times \mathbf{E}. \tag{1.7}$$

Electric and magnetic fields are decentered on the Cartesian Yee mesh, as in standard FDTD and illustrated in Figure 1.6. **E** is defined on cell edges and and **B** on cell faces. This is done to facilitate the computation of numerical curls of **E** and **B** when evolving Maxwell's equations. Instead of the leapfrog time integration typically used in FDTD, we employ a third order Runge-Kutta integrator as in Spitkovsky (2006). This is done to remove the interpolation in time that would otherwise be needed to bring the **E** and **B** fields to the same time step when computing the source current. The exact method for prescribing **j** will be prescribed in Chapter 2. Boundary conditions depend on the problem of interest and are described individually for each application of our code.

5 Applications

We apply our method to solve a number of problems in neutron star magnetosphere theory. Chapter 2 derives our resistive force-free method and presents a continuum of solutions that smoothly transitions between the vacuum and ideal force-free pulsar magnetosphere solutions. It is based on work presented in Li et al. (2012b). The plasma conductivity naturally allows us to vary the magnetospheric plasma supply. We use this property to construct a model for the spin-down of intermittent pulsars, pulsars that switch between distinct states with different spin-down luminosities and different radio emission properties. This model, presented in Chapter 3, is based on work published in Li et al. (2012a). Finite plasma conductivity also allows us to study the effects of accelerating electric fields on the magnetospheric structure. Chapter 4 explores high-energy emission from γ-ray pulsars, focusing on emission from two regions with strong parallel electric fields that can accelerate particles to high energies: magnetospheric current sheets and current layers. This work will be published in Li et al. (in prep.). Chapter 5 presents another application of our numerical method, the study of binary neutron star magnetospheres. We explore the basic magnetospheric structure and electromagnetic luminosity of binary systems that can be observed by the next generation of gravitational wave detectors: Advanced LIGO and Advanced Virgo. Our work on high-energy emission from γ-ray pulsar current sheets also suggests a possible mechanism that can generate the precursor emission seen in some short-duration γ-ray bursts (Troja et al., 2010). This work on binary neutron star magnetospheres will be published in Li & Spitkovsky (in prep.). Finally, Chapter 6 summarizes our work and touches on the future outlook of neutron star magnetosphere theory.

Bibliography

Abdo, A. A., Ackermann, M., Ajello, M., Atwood, W. B., Axelsson, M., Baldini, L., Ballet, J., Barbiellini, G., Baring, M. G., Bastieri, D., & et al. 2010, ApJS, 187, 460

Arons, J. & Scharlemann, E. T. 1979, ApJ, 231, 854

Cheng, K. S., Ho, C., & Ruderman, M. 1986, ApJ, 300, 500

Contopoulos, I., Kazanas, D., & Fendt, C. 1999, ApJ, 511, 351

Cordes, J. M., Kramer, M., Lazio, T. J. W., Stappers, B. W., Backer, D. C., & Johnston, S. 2004, New A Rev., 48, 1413

Deutsch, A. J. 1955, Annales d'Astrophysique, 18, 1

Dyks, J., Harding, A. K., & Rudak, B. 2004, ApJ, 606, 1125

Gold, T. 1968, Nat, 218, 731

Goldreich, P. & Julian, W. H. 1969, ApJ, 157, 869

Gruzinov, A. 2005, Physical Review Letters, 94, 021101

—. 2007, ArXiv e-prints

—. 2008, ArXiv e-prints

—. 2011, ArXiv e-prints

Gunn, J. E. & Ostriker, J. P. 1969, Nat, 221, 454

Hewish, A., Bell, S. J., Pilkington, J. D. H., Scott, P. F., & Collins, R. A. 1968, Nat, 217, 709

Kalapotharakos, C. & Contopoulos, I. 2009, A&A, 496, 495

Komissarov, S. S. 2006, MNRAS, 367, 19

Li, J. & Spitkovsky, A. in prep.

Li, J., Spitkovsky, A., & Tchekhovskoy, A. 2012a, ApJ, 746, L24

—. 2012b, ApJ, 746, 60

—. in prep.

Lichnerowicz, A. 1967, Relativistic Hydrodynamics and Magnetohydrodynamics

Lyubarsky, Y. E. 1995, Physics of pulsars

Lyutikov, M. 2003, MNRAS, 346, 540

McKinney, J. C. 2006, MNRAS, 368, L30

Michel, F. C. & Li, H. 1999, Phys. Rep., 318, 227

Palenzuela, C. 2013, MNRAS, 431, 1853

Palenzuela, C., Lehner, L., Reula, O., & Rezzolla, L. 2009, MNRAS, 394, 1727

Parfrey, K., Beloborodov, A. M., & Hui, L. 2012, MNRAS, 423, 1416

Pétri, J. 2012, MNRAS, 424, 605

Radhakrishnan, V. & Cooke, D. J. 1969, Astrophys. Lett., 3, 225

Ruderman, M. A. & Sutherland, P. G. 1975, ApJ, 196, 51

Spitkovsky, A. 2006, ApJ, 648, L51

Sturrock, P. A. 1971, ApJ, 164, 529

Taflove, A. & Hagness, S. 2005, Computational Electrodynamics: The Finite-Difference Time-Domain Method, 3rd edn. (Norwood, MA: Artech House)

Tchekhovskoy, A., Spitkovsky, A., & Li, J. G. 2013, MNRAS, 435, L1

Thompson, D. J. 2004, in Astrophysics and Space Science Library, Vol. 304, Cosmic Gamma-Ray Sources, ed. K. S. Cheng & G. E. Romero, 149

Timokhin, A. N. 2006, MNRAS, 368, 1055

Troja, E., Rosswog, S., & Gehrels, N. 2010, ApJ, 723, 1711

Werner, G. R. & Cary, J. R. 2007, Journal of Computational Physics, 226, 1085

Chapter 2

Resistive Solutions for Pulsar Magnetospheres

1 Introduction

In the resistive force-free picture of the pulsar magnetosphere, the magnetized neutron star is thought to be surrounded by an abundant massless plasma with finite conductivity, so that not all accelerating fields are shorted out. For simplicity and as a proof of principle, we only consider here the unrealistic case of constant conductivity throughout space. More complicated prescriptions will be studied in subsequent chapters. Our finding is that using our formulation of the resistive force-free electrodynamics we can construct a family of magnetospheres that smoothly transition from the Deutsch vacuum solution to the ideal force-free magnetosphere as the conductivity of the plasma is increased. Such intermediate magnetospheres possess interesting properties that we discuss in this chapter. We study the variation of the spin-down power with magnetic inclination angle as a function of plasma conductivity and relate it to physical conditions such as the effective potential drop on the open field lines. In Section 2 we discuss the derivation of the resistive force-free prescription, in Section 3 we describe our code for solving the equations and present sample magnetospheric solutions. Discussion and potential applications to pulsar physics are in Section 4.

2 Resistive Electrodynamics

We describe here our prescription for resistive current as used in our numerical code. Ohm's Law is defined in the fluid rest frame. In this frame the electric and magnetic fields are parallel; otherwise, there would be a particle drift across magnetic field lines. The laboratory frame can be connected to the fluid rest frame through two boosts. One boost is in the $\mathbf{E} \times \mathbf{B}$ direction in the lab frame and brings the electric field parallel to the magnetic field. The other boost is along the parallel electric and magnetic fields and transforms the 4-current to the fluid rest frame while leaving the electric and magnetic fields parallel. We choose a simple Ohm's Law to relate the current and electric field in the fluid frame: $\mathbf{j}_{\rm fluid} = \sigma \mathbf{E}_{\rm fluid}$, where σ is the plasma conductivity. More general formulations of the Ohm's Law that take into account time-dependent currents, inertial effects, pressure, and the Hall effect have been derived (see e.g., Meier, 2004). It is likely safe to ignore most of these effects in the bulk of the strongly magnetized cold pair plasma, as envisioned for typical pulsar magnetospheres; however, singular current sheets may require a more elaborate treatment. In this Chapter we use a constant uniform conductivity throughout the domain and restrict ourselves to the simple Ohm's Law to elucidate the basic physics. Boosting back to the laboratory frame, the current vector can be expressed as

$$\begin{aligned} \mathbf{j} &= \frac{\rho c \mathbf{E} \times \mathbf{B}}{B^2 + E_0^2} \\ &+ \frac{(-\beta_{||} \rho c + \sqrt{\frac{B^2+E_0^2}{B_0^2+E_0^2}(1-\beta_{||}^2)}\sigma E_0)(B_0 \mathbf{B} + E_0 \mathbf{E})}{B^2 + E_0^2}. \end{aligned} \tag{2.1}$$

See Section 2.1 for a full derivation of this expression and the subsequent limits that we discuss below. Here, $\beta_{||}$ is the magnitude of the boost along the parallel electric and magnetic fields to the fluid rest frame, ρ is the charge density in the laboratory frame, and E_0 and B_0 are the magnitudes of the electric and magnetic fields in all frames in which they are parallel. E_0 and B_0

are defined by the expressions (Gruzinov, 2007, 2008)

$$\begin{aligned} B_0^2 &= \frac{\mathbf{B}^2 - \mathbf{E}^2 + \sqrt{(\mathbf{B}^2 - \mathbf{E}^2)^2 + 4(\mathbf{E}\cdot\mathbf{B})^2}}{2}, \\ E_0 &= \sqrt{B_0^2 - \mathbf{B}^2 + \mathbf{E}^2}, \\ B_0 &= \mathrm{sign}(\mathbf{E}\cdot\mathbf{B})\sqrt{B_0^2}, \end{aligned} \tag{2.2}$$

where we allow B_0 to be positive or negative, depending on whether the magnetic field is aligned or antialigned with the electric field. Note that in addition to the advection of charge in the $\mathbf{E}\times\mathbf{B}$ direction, there is conduction current along both the laboratory frame magnetic field and the electric field (the last term in equation 2.1). There is still a principal ambiguity here in defining the fluid rest frame, as we have not yet specified the magnitude of the parallel boost $\beta_{||}$. In fact, this speed cannot be obtained from a purely electrodynamic standpoint without the inclusion of gas dynamics, so a suitable choice has to be made.

One particularly interesting choice of fluid frame is the slowest moving frame that has electric fields parallel to magnetic fields, i.e., the frame with $\beta_{||} \to 0$. If particles start out on the stellar surface with non-relativistic velocity, then the fluid essentially satisfies this condition in the high conductivity limit (see e.g., Contopoulos & Kazanas, 2002; Tchekhovskoy et al., 2009; Beskin, 2010). In this minimal velocity limit the current becomes

$$\mathbf{j} = \frac{\rho c\mathbf{E}\times\mathbf{B} + \sqrt{\frac{B^2+E_0^2}{B_0^2+E_0^2}}\sigma E_0(B_0\mathbf{B} + E_0\mathbf{E})}{B^2 + E_0^2}. \tag{2.3}$$

This form of the current has the especially useful property that in the limit of vanishing conductivity the conduction current along the electric and magnetic fields goes to zero. Such a magnetosphere does not develop space charge due to the flow of charge from the star along the field lines. Thus, the current in the $\mathbf{E}\times\mathbf{B}$ direction also vanishes. This is exactly what we expect in the vacuum limit. Since we are interested in producing a resistive transition from ideal force-free to vacuum, we use this form of the current in our numerical investigation. Lyutikov (2003) derived an expression for resistive current in magnetically dominated plasma, choosing the

same minimal velocity frame for the formulation of the Ohm's law as in our derivation. However, his boost in the $\mathbf{E} \times \mathbf{B}$ direction to the fluid frame contains an error and does not bring the electric and magnetic fields parallel to one another. As a result, our final expressions differ.

We can alternatively express the minimal velocity current as

$$\mathbf{j} = \rho \mathbf{v} + \sigma \mathbf{E}_{\text{fluid}}, \tag{2.4}$$

where the fluid velocity $\mathbf{v} = c(\mathbf{E} \times \mathbf{B})/(B^2 + E_0^2)$ is the generalized drift velocity, $\mathbf{E}_{\text{fluid}} = \gamma(\mathbf{E} + \mathbf{v} \times \mathbf{B})$, and $\gamma = (1 - v^2/c^2)^{-1/2}$. The drift velocity contains the term E_0^2 in the denominator to account for the non-zero electric field in the fluid frame (see equation 2.21). The presence of this term allows the current to remain nonsingular in current sheets, where the magnetic field vanishes.

It is instructive to consider other limits for the current. Gruzinov (2007, 2008) derived an alternate limit of the general current in equation (2.1), known as Strong-Field Electrodynamics. He postulated that Ohm's law should be formulated in the frame where charge density vanishes, which gives parallel boost

$$\beta_{||} = \frac{-\rho}{(\gamma_x^2 \sigma^2 E_0^2/c^2 + \rho^2)^{1/2}} \tag{2.5}$$

and current

$$\mathbf{j} = \frac{\rho c \mathbf{E} \times \mathbf{B} + (\gamma_x^2 \sigma^2 E_0^2 + \rho^2 c^2)^{1/2}(B_0 \mathbf{B} + E_0 \mathbf{E})}{B^2 + E_0^2}, \tag{2.6}$$

where $\gamma_x^2 \equiv (B^2 + E_0^2)/(B_0^2 + E_0^2)$. We see no special reason as to why the fluid frame charge density must vanish. Further, this current does not reduce to vacuum as the conductivity drops to zero, as it does in equation (2.3). Consequently, even for vanishing conductivity the Strong-Field Electrodynamics solutions resemble ideal non-resistive solutions.

In the limit of infinitely conductive strongly magnetized plasma, which we refer to as the ideal force-free limit, the plasma satisfies transverse force balance, $\rho \mathbf{E} + \mathbf{j} \times \mathbf{B} = 0$, and the parallel electric field is shorted out, $E_0 \to 0$. However, as $\sigma \to \infty$, the product of σE_0 stays finite, and the

minimal velocity current becomes (Osherovich & Gliner, 1988; Gruzinov, 1999; Blandford, 2002)

$$\mathbf{j} = \frac{\rho c \mathbf{E} \times \mathbf{B}}{B^2} + \frac{c}{4\pi} \frac{(\mathbf{B} \cdot \nabla \times \mathbf{B} - \mathbf{E} \cdot \nabla \times \mathbf{E})\mathbf{B}}{B^2}. \tag{2.7}$$

Moreover, this reduction to the ideal force-free current at high σ is weakly sensitive to the choice of parallel boost $\beta_{||}$, which lends credence to our methods.

2.1 Resistive Current Derivation

We derive here in full generality our resistive current prescription. We start in the fluid frame, with charge ρ_0 and current flowing along the electric field with magnitude σE_0. For convenience, we pick the current and electric field to point along the positive z axis. The magnetic field can point along the positive or negative z axis, depending on whether B_0 is positive or negative. If we boost along the z axis with $\beta_{\mathbf{1}} = (0, 0, \beta_z)$, the current 4 vector in the boosted frame satisfies

$$\begin{bmatrix} \rho' c \\ \\ \\ j'_z \end{bmatrix} = \begin{bmatrix} \gamma_z & -\beta_z\gamma_z \\ & \\ & \\ -\beta_z\gamma_z & \gamma_z \end{bmatrix} \times \begin{bmatrix} \rho_0 c \\ 0 \\ 0 \\ \sigma E_0 \end{bmatrix}. \tag{2.8}$$

Boosting again in the x direction transverse to the electric and magnetic fields with $\beta_{\mathbf{2}} = (\beta_x, 0, 0)$,

$$\begin{bmatrix} \rho c \\ j_x \\ \\ j_z \end{bmatrix} = \begin{bmatrix} \gamma_x & \\ -\beta_x\gamma_x & \\ & \\ & 1 \end{bmatrix} \times \begin{bmatrix} \rho' c \\ 0 \\ 0 \\ j'_z \end{bmatrix}, \tag{2.9}$$

we obtain for lab frame quantities the system of equations

$$\rho = \gamma_x\gamma_z\rho_0 - \gamma_x\beta_z\gamma_z\sigma E_0/c, \tag{2.10}$$

$$j_x = -\beta_x c\rho, \tag{2.11}$$

$$j_z = -\beta_z \gamma_z c\rho_0 + \gamma_z \sigma E_0. \tag{2.12}$$

Rearranging equation (2.10),

$$\rho_0 = \frac{\rho}{\gamma_x \gamma_z} + \beta_z \sigma E_0 / c, \tag{2.13}$$

and plugging into equation (2.12),

$$\begin{aligned} j_z &= -\beta_z \gamma_z c(\frac{\rho}{\gamma_x \gamma_z} + \beta_z \sigma E_0/c) + \gamma_z \sigma E_0 \\ &= -\frac{\beta_z}{\gamma_x} c\rho + \frac{1}{\gamma_z} \sigma E_0. \end{aligned} \tag{2.14}$$

We next determine the magnitude of the perpendicular boost in the x direction. The electromagnetic fields are invariant under the boost $\beta_{\mathbf{1}}$. After applying the boost $\beta_{\mathbf{2}}$, the lab frame electromagnetic fields become

$$\begin{aligned} &E_x = 0 \qquad E_y = \gamma_x(E'_y - \beta_x B'_z) = -\gamma_x \beta_x B_0 \qquad E_z = \gamma_x(E'_z + \beta_x B'_y) = \gamma_x E_0 \\ &B_x = 0 \qquad B_y = \gamma_x(B'_y + \beta_x E'_z) = \gamma_x \beta_x E_0 \qquad B_z = \gamma_x(B'_z + \beta_x E'_y) = \gamma_x B_0. \end{aligned} \tag{2.15}$$

Hence

$$B^2 = \frac{\beta_x^2 E_0^2 + B_0^2}{1 - \beta_x^2}, \tag{2.16}$$

$$\beta_x^2 = \frac{B^2 - B_0^2}{B^2 + E_0^2}, \tag{2.17}$$

and

$$\gamma_x^2 = \frac{B^2 + E_0^2}{B_0^2 + E_0^2}. \tag{2.18}$$

The lab frame x direction corresponds to the $-\vec{E} \times \vec{B}$ direction. The y and z coordinates are rotated with respect to the $\vec{B}$ and $\vec{E}_\perp$ directions. We let θ denote the angle between the z axis and the laboratory frame magnetic field and assume without loss of generality that $\beta_x > 0$. The

current in the $\mathbf{E} \times \mathbf{B}$ direction is then

$$j_{\widehat{\mathbf{E}\times\mathbf{B}}} = \beta_x c\rho. \tag{2.19}$$

Noting that

$$E_\perp^2 = \mathbf{E}^2 - (E_0 B_0/B)^2 = B^2 + E_0^2 - B_0^2 - E_0^2 B_0^2/B^2, \tag{2.20}$$

$$\beta_x = \sqrt{\frac{B^2 - B_0^2}{B^2 + E_0^2}} = \frac{E_\perp B}{B^2 + E_0^2}. \tag{2.21}$$

The boost $-\beta_{\mathbf{1}} = (-\beta_x, 0, 0)$ is the slowest boost from the lab frame that brings the electric and magnetic fields parallel to one another, and β_x can be thought of as a generalized drift velocity. From β_x, we immediately obtain the transverse current

$$j_{\widehat{\mathbf{E}\times\mathbf{B}}} = \frac{\rho E_\perp B}{B^2 + E_0^2} c. \tag{2.22}$$

The current in the direction of the magnetic field is

$$\begin{aligned} j_{\widehat{\mathbf{B}}} &= j_z \cos\theta = (-\frac{\beta_z}{\gamma_x}\rho c + \frac{1}{\gamma_z}\sigma E_0)\frac{\gamma_x B_0}{B} \\ &= (-\beta_z \rho c + \frac{\gamma_x}{\gamma_z}\sigma E_0)\frac{B_0 B + E_0 \mathbf{E}\cdot\mathbf{B}/B}{B^2 + E_0^2}. \end{aligned} \tag{2.23}$$

The current in the direction $\mathbf{E}_\perp$ is

$$\begin{aligned} j_{\widehat{\mathbf{E}_\perp}} &= j_z \sin\theta = (-\frac{\beta_z}{\gamma_x}\rho c + \frac{1}{\gamma_z}\sigma E_0)\frac{\gamma_x \beta_x E_0}{B} \\ &= (-\beta_z \rho c + \frac{\gamma_x}{\gamma_z}\sigma E_0)\frac{E_0 E_\perp}{B^2 + E_0^2}. \end{aligned} \tag{2.24}$$

Hence the laboratory frame current vector can be expressed in full generality as

$$\mathbf{j} = \frac{\rho c \mathbf{E}\times\mathbf{B} + (-\beta_z \rho c + \sqrt{\frac{B^2+E_0^2}{B_0^2+E_0^2}(1-\beta_z^2)}\sigma E_0)(B_0\mathbf{B} + E_0\mathbf{E})}{B^2 + E_0^2}. \tag{2.25}$$

In Section 2 β_z has been replaced by $\beta_{||}$ to emphasize that it is the magnitude of the boost along the parallel electric and magnetic fields to the fluid rest frame.

3 Numerical Simulations

In order to test the influence of global resistivity on the structure of pulsar magnetospheres, we employ the three-dimensional numerical code described in Chapter 1 that implements the finite difference time-domain scheme (Taflove & Hagness, 2005) to evolve electromagnetic fields from Maxwell's equations,

$$\begin{aligned} \partial_t \mathbf{E} &= c\nabla \times \mathbf{B} - 4\pi \mathbf{j}, \\ \partial_t \mathbf{B} &= -c\nabla \times \mathbf{E}, \end{aligned} \tag{2.26}$$

where the current is given by equations (2.2) and (2.3). We run our simulations on a grid of size 1024^3 at Courant number 0.5. The central region of our grid is occupied by a conducting spherical star of radius R_*, rotating at angular velocity $\mathbf{\Omega}$, with embedded dipole field of magnetic moment μ inclined relative to the rotation axis by angle α (see Spitkovsky 2006, hereafter S06 for more detail). The electric field inside the star is set to ensure rigid corotation, and we smooth fields across the stellar boundary as in S06 in order to minimize stair-stepping of a sphere on a Cartesian grid. The spatial resolution of our simulations is such that the light cylinder (LC) radius, $R_{\rm LC} = c/\Omega$, is resolved with 80 cells, and the simulation box is $12.8\,R_{\rm LC}$ on a side. The outer boundary condition is periodic, which limits our run time to the light travel time across the grid. We set $R_* = 30$ cells, allowing us to resolve the star while keeping the star sufficiently small compared to the light cylinder. We run our code for a range of different values of the dimensionless conductivity, σ/Ω, to produce a transition from vacuum at low conductivity to ideal force-free solution at high conductivity. We have verified that our solutions are converged with spatial resolution, as well as run sufficiently long so as to reach a steady state in the frame corotating with the pulsar.

In addition to the resistive solutions obtained with the above method, we also consider two special cases of the current prescription that we call "force-free" and "vacuum." By force-free solutions we mean "ideal force-free" magnetospheres; however, instead of using the full equation (2.7) for the current, our numerical implementation follows the approach in S06, where at each time step we evolve the perpendicular part of the current from equation (2.7) and then correct the electric field by removing any electric field component parallel to the magnetic field. Further field limiters are used to enforce $E < B$ in current sheets. As a result, the force-free scheme of S06 has an effective small resistivity, because the cleaning of parallel fields can be interpreted as the effect of very large conductivity along field lines. Also, as all parallel fields are cleaned on every step, such a scheme does not have the usual convergence behavior with timestep. The resistive scheme using equation (2.3) gives us a more well-defined method for handling magnetospheric dissipation. In addition, this resistive scheme does not require special limiters to handle current sheets[1]. The "vacuum" solutions described below evolve Maxwell's equations without volume charges or currents outside the star, allowing for significant potential drops along field lines.

In Figure 2.1 we show magnetic field lines in the μ-$\mathbf{\Omega}$ plane for 60° inclined force-free dipole (panel a), resistive dipoles at $(\sigma/\Omega)^2 = 40$ (panel b), $(\sigma/\Omega)^2 = 4$ (panel c), $(\sigma/\Omega)^2 = 0.4$ (panel d), $(\sigma/\Omega)^2 = 0.04$ (panel e), and vacuum dipole (panel f). The field lines are shown after 1.5 turns, sufficiently long to reach a steady state out to several light cylinder radii in the corotating frame. We show only the central five light cylinders of our simulation. Color represents the out-of-plane magnetic field into (red) and out of (blue) the page. The maximum magnitude of the out-of-plane magnetic field value is different in each panel, with maximum value increasing with conductivity. Table 2.1 gives the maximum values normalized to the maximum vacuum value[2]. The maximum values occur at the stellar surface and fall on the blue end of the color table. To improve contrast, the color table shows values up to 30% of the maximum, and a square root

[1]This property is not unique to our resistive current prescription, and is also present in the original formulation by Gruzinov (2007, 2008).

[2]The discrepancy between maximum field for vacuum and $\sigma = 0$ solutions is numerical and is due to the boundary conditions on the star. This is further discussed in Section 3.1

stretching is applied to the data. Gradients in color reflect the sum of in-plane components of conduction and displacement currents.

Figure 2.1a shows the force-free magnetosphere. The gross features of this solution are the same as were discussed in S06[3], Contopoulos & Kalapotharakos (2010) and Bai & Spitkovsky (2010). The polar cap consists of the footpoints of open field lines that extend out to infinity. Field lines with both ends attached to the star form the closed field line region, which extends out to a cylindrical distance of $1R_{LC}$. A large scale conduction current flows outwards from the polar cap along open field lines and returns through the current sheet, current layer, and a fraction of the neighboring open field lines. The current sheets appear as the sharp transition in the out-of-plane magnetic field, starting at the Y-point at the light cylinder. The current layer flows along the boundary of the closed field line region. The conduction current is closed in a circuit by a surface current flowing across the polar cap, a point we will return to when discussing pulsar spin-down.

At $(\sigma/\Omega)^2 = 40$, shown in Figure 2.1b, the qualitative picture of the magnetosphere looks quite similar to force-free. We find that values $(\sigma/\Omega)^2 > 40$ give fairly good estimates of highly conducting magnetospheres for $R_*/R_{\rm LC} = 3/8$. The dimensionless quantity $\sigma/\Omega = (c/\Omega)/(c/\sigma)$ is the relativistic analog of the Elsasser number, defined as the ratio of the Alfvén radius in a rotating system, v_A/Ω, to the resistive diffusion scale (Elsasser, 1946). The above threshold corresponds to resistive diffusion length scale c/σ small compared to the light cylinder, $c/\sigma < 0.16R_{\rm LC} \ll R_{\rm LC}$, while satisfying $c/\sigma \lesssim R_{\rm pc} = R_*(R_*/R_{\rm LC})^{1/2}$. We have also run simulations with our current prescription at higher conductivity, $(\sigma/\Omega)^2 = 400$, and find spin-down luminosities that match the force-free values quite well. Our explicit scheme requires very small time step at such high conductivities though, and it is perhaps more appropriate to use an implicit-explicit (Palenzuela et al., 2009) or fully implicit scheme to explore this regime. We note that the kink in the current sheet seen in the force-free solution near $2R_{\rm LC}$ disappears for

[3]In comparing to previous force-free results, we note that S06 rescaled the total magnetic field when displaying the out-of-plane component, whereas we rescale only the strength of the out-of-plane component.

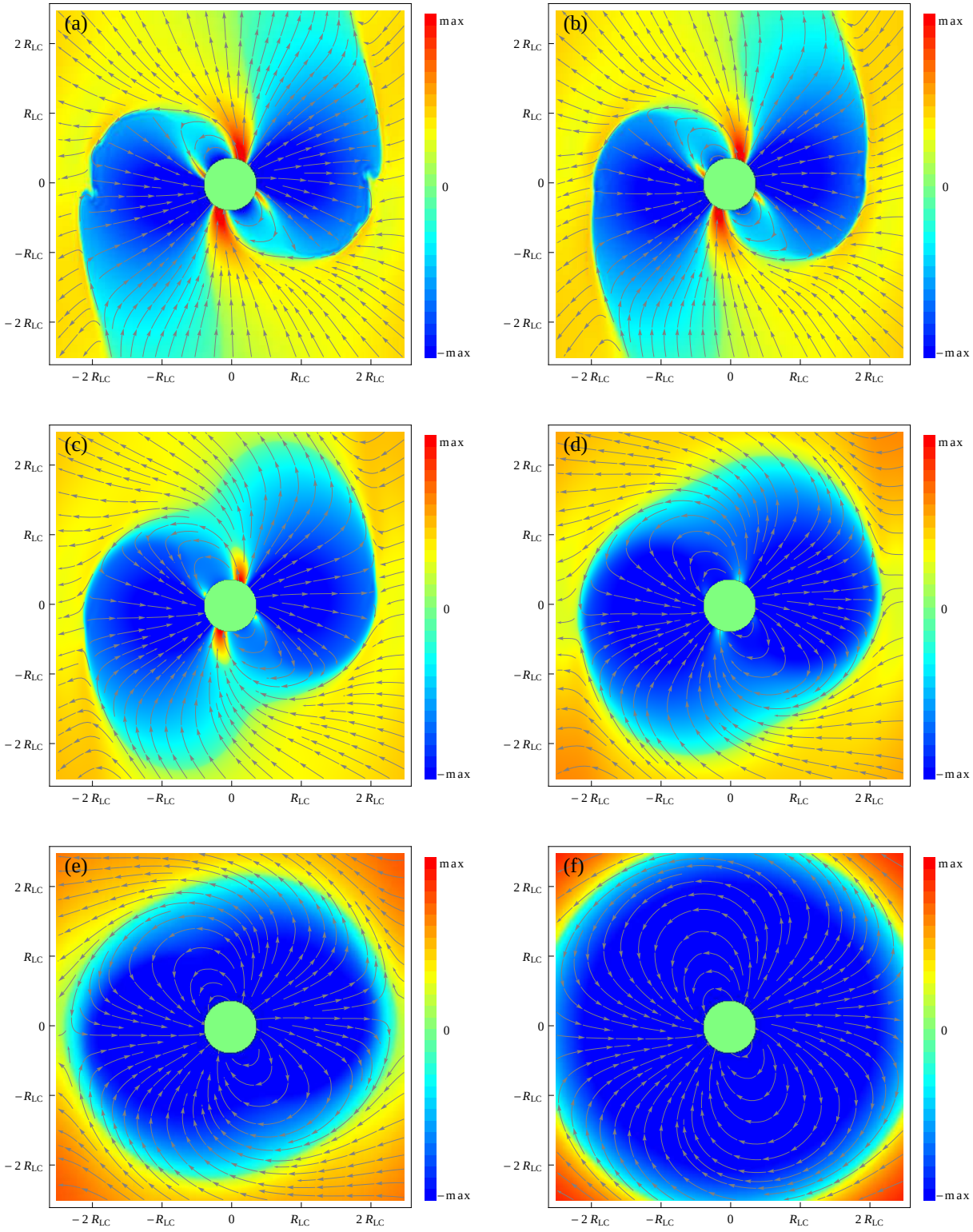

Figure 2.1: Magnetic field lines in the $\mu - \mathbf{\Omega}$ plane for a 60° inclined dipole. Color represents out-of-plane magnetic field into (red) and out of (blue) the page. The color table shows only values up to 30% of the maximum of the out-of-plane magnetic field, and a square root stretching has been applied to its magnitude. The maximum out-of-plane magnetic field values are given in Table 2.1. Conduction and displacement currents weaken with decreasing conductivity. (a) force-free dipole; (b) resistive dipole at $(\sigma/\Omega)^2 = 40$; (c) $(\sigma/\Omega)^2 = 4$; (d) $(\sigma/\Omega)^2 = 0.4$; (e) $(\sigma/\Omega)^2 = 0.04$; (f) vacuum dipole.

resistive solutions even at high conductivities. It is likely then that this kink is a numerical artifact of the cleaning procedure used in our force-free formulation.

Table 2.1: Maximum out-of-plane magnetic field values, normalized to the maximum vacuum value, for each panel from Figure 2.1.

$(\sigma/\Omega)^2$	$B_{\rm out,max}/B_{\rm out,max,vac}$
force-free	8.7
40.	8.3
4.	6.3
0.4	4.0
0.04	2.5
0	1.2
vacuum	1.

Displacement currents play an important role in the highly conducting magnetospheres of Figures 2.1a and 2.1b. The displacement currents in the current sheets actually dominate over conduction currents for the 60° rotator. Displacement currents are not present in the magnetospheres of aligned rotators, but the strength of the displacement current in the current sheets of highly conducting magnetospheres increases monotonically with increasing inclination angle. This is in contrast to the conduction currents, whose strength is independent of inclination angle for fixed conductivity. Both displacement and conduction currents weaken considerably with decreasing conductivity, reflected by smaller gradients in the out-of-plane magnetic field in panels (b) through (e) of Figure 2.1. Recall that the maximum in the color table corresponds to weaker out-of-plane magnetic field at lower conductivities. The extent of the closed field line region also expands with decreasing conductivity, evident in the same sequence of panels. We further expect the current sheet to thicken with decreasing conductivity. At $(\sigma/\Omega)^2 = 0.04$, shown in Figure 2.1e, the current sheet should have characteristic width c/σ of order $5R_{LC}$.

There is an obvious increase in the radius of toroidal field sign reversal beyond the light cylinder as one transitions from the force-free to the vacuum magnetosphere. This can be understood from the increase in the winding radius of the spiral pattern for lower conductivities. The winding of the spiral is determined by the characteristic speed of the radial outflow multiplied by the pulsar period. In the force-free case, the radial outflow is given by the radial component of

the $\mathbf{E} \times \mathbf{B}$ velocity, which increases with radius so that the Lorentz factor grows linearly with cylindrical radius: $\gamma_{E\times B} = \sqrt{1 + (R/R_{\rm LC})^2}$ (Contopoulos & Kazanas, 2002). Thus, the force-free outflow approaches the speed of light only asymptotically. In the vacuum case, the "outflow" is always at the speed of light, so we expect the sign transition of the field to occur near the half-wavelength of the vacuum wave, or $\pi R_{\rm LC}$, as is confirmed by Figure 2.1f. The force-free case of Figure 2.1a reverses near $2R_{\rm LC}$, indicative of the smaller outflow speed near the light cylinder.

The surface currents flowing across the polar cap of the pulsar exert a spin-down torque on the star. The rotational energy loss is connected to infinity by an outward directed Poynting flux, which can be thought of as the ejection of toroidal field. We compute the Poynting flux at the light cylinder for each of our simulation runs and show the results in Figure 2.2. All spin-down values are calculated for $R_* = 3/8R_{LC}$. The spin-down curves have been normalized to L_0, defined as 3/2 times the power of the orthogonal vacuum rotator with finite $R_* = 3/8R_{LC}$. Two-dimensional axisymmetric calculations for small star tell us that the spin-down of the aligned force-free rotator should be 3/2 times larger than the power of the orthogonal point vacuum dipole, $L_1 = 2\mu^2\Omega^4/3c^3$ (Contopoulos et al. 1999; Gruzinov 2005; McKinney 2006; S06). The short dashed line shows the function $L/L_0 = 1 + \sin^2\alpha$, the expected force-free curve in the limit of small star with inclined dipole (S06). The gray band around the force-free curve indicates the uncertainty in the measurement due to boundary effects and numerical dissipation of Poynting flux in the magnetosphere (see Appendix B for thorough discussion). Similar bands are implied but not shown for resistive spin-down curves. The long dashed line shows the analytic vacuum Deutsch field solution (Michel & Li, 1999). One of our principal results is that we see a smooth monotonic transition from the force-free spin-down curve to the vacuum spin-down curve for decreasing conductivity.

All spin-down curves in Figure 2.2 show a strong dependence on both inclination angle and conductivity. The radial Poynting flux carrying the spin-down power is proportional to the product of poloidal and toroidal magnetic fields ($E_\theta B_\phi \sim \Omega R B_p B_\phi/c$), both of which are affected by the strength of displacement and conduction currents in the magnetosphere. One can get a qualitative feel for the relative significance of two contributions by considering the limiting cases.

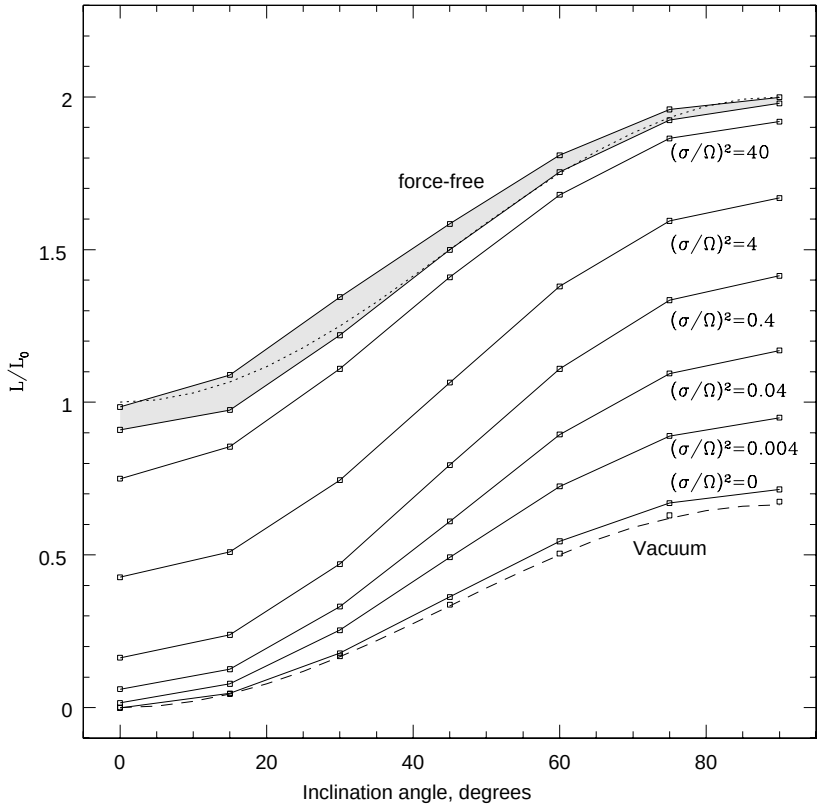

Figure 2.2: Spin-down luminosity dependence on inclination angle for force-free, a sequence of resistive, and vacuum dipoles. Spin-down is normalized by 3/2 times the spin-down power of the orthogonal vacuum rotator. We see a smooth monotonic transition from force-free to vacuum with decreasing conductivity.

In vacuum, the increase of spin-down with inclination is solely due to rising displacement current. This current is likely responsible for much of the angular dependence of the resistive and force-free solutions. The increase in spin-down with increasing conductivity is due to the additional sweep-back and opening of the poloidal field brought on by the increasing conduction current. We find that spin-down luminosity at any conductivity has an angle-dependent term proportional to $\sin^2 \alpha$. We parameterize the spin-down curves in Figure 2.2 with functions $f(\sigma/\Omega)$

and $g(\sigma/\Omega)$ such that $L/L_0 = f(\sigma/\Omega) + g(\sigma/\Omega)\sin^2\alpha$. We find the piecewise linear fit

$$\begin{aligned}
\frac{L}{L_0} &= 0.3 + 0.3\log(\sigma/\Omega)^2 + 1.2\sin^2\alpha\,,\ (\sigma/\Omega)^2 > 0.4; \\
\frac{L}{L_0} &= 0.2 + 0.08\log(\sigma/\Omega)^2 + (1.3 + 0.2\log(\sigma/\Omega)^2)\sin^2\alpha, \\
&\quad 0.004 < (\sigma/\Omega)^2 < 0.4.
\end{aligned} \tag{2.27}$$

The amplitude of the angular dependence, $g(\sigma/\Omega)$, is constant for $(\sigma/\Omega)^2 > 0.4$ and begins to transition to the vacuum value below $(\sigma/\Omega)^2 = 0.4$.

We have thus far shown how spin-down luminosity depends on plasma conductivity, but the physical meaning of the conductivity is not entirely clear. It is instructive to reinterpret the conductivity parameter, σ/Ω, in terms of the potential drop along open field lines in the corotating frame. This gives us a handle on the deviation of the magnetosphere from ideal force-free, which has vanishing potential drops along field lines. The electromagnetic fields in the frame corotating with the pulsar are obtained via a coordinate transformation from the laboratory frame (Schiff, 1939; Grøn, 1984):

$$\mathbf{E}' = \mathbf{E} + \frac{\mathbf{\Omega} \times \mathbf{r}}{c} \times \mathbf{B} \tag{2.28}$$

and

$$\mathbf{B}' = \mathbf{B}. \tag{2.29}$$

Since the fields are steady in the corotating frame, $\nabla \times \mathbf{E}' = 0$ and the corotating electric field can be written as the gradient of a scalar potential, i.e., $\mathbf{E}' = \nabla\chi$. Taking the line integral of the corotating electric field along a magnetic field line, l, we find

$$\Delta\chi = \int_l \mathbf{E}' \cdot \mathbf{dl} = \int_l \mathbf{E} \cdot \mathbf{dl} \equiv V_{\rm drop}. \tag{2.30}$$

We see that the potential drop along field lines in the corotating frame can be computed directly from the laboratory frame fields. Although in resistive solutions particles will actually drift across

magnetic field lines, in addition to accelerating along them, we choose to study the field-aligned potential drop $V_{\rm drop}$ as a fiducial measure of particle energy gain. In fact, the exact particle trajectories we choose make little difference when estimating potential drops because the electric field is potential in the frame corotating with the pulsar.

Consider field lines starting on the stellar surface in the $\mu - \mathbf{\Omega}$ plane separated by 15° in latitude from pole to equator. For every such field line we integrate the electric field to find the maximum potential drop along each field line. We then determine the field line with the largest overall potential drop for a given magnetic inclination. Integrating field lines separated by 15° increments on the stellar surface is sufficient to give a good estimate of the maximum potential drop along field lines. Figure 2.3 shows the maximal potential drop as a function of dipole inclination angle for different conductivities. All results have been normalized to the potential drop from the pole to the equator of an aligned vacuum rotator in the laboratory frame, $V_0 = |\mu|/(R_{\rm LC} R_*)$. As our models do not prescribe a high conductivity to the closed field line region, the available accelerating potential is generally limited by the pole-to-equator potential difference, rather than the smaller polar cap potential, $V_{\rm pc} = V_0 R_*/R_{LC}$, with a few notable exceptions. Low conductivity solutions, $(\sigma/\Omega)^2 \lesssim 0.04$, at high inclination angle, $\alpha > 45°$, have $V_{\rm drop}$ scaling intermediate between V_0 and $V_{\rm pc}$. The orthogonal rotator drop at $(\sigma/\Omega)^2 = 0.04$ scales roughly with $V_{\rm pc}$. Using the vacuum Deutsch fields, one can obtain that the aligned vacuum rotator potential drop scales exactly proportional to V_0, whereas the orthogonal vacuum rotator drop scales closer to $V_{\rm pc}$. From Figure 2.3 we see that for $(\sigma/\Omega)^2 > 0.04$ the potential drop is roughly independent of inclination angle for fixed σ, i.e., there is a one-to-one map between conductivity and maximal potential drop along a field line originating in the $\mu - \mathbf{\Omega}$ plane for all inclination angles. The maximal potential drop increases from zero for force-free (or $\sigma/\Omega \to \infty$) to $V_{\rm drop}/V_0 \sim 0.2$ for $(\sigma/\Omega)^2 = 0.04$.

The fact that potential drop is independent of inclination angle for $(\sigma/\Omega)^2 > 0.04$ allows us to relate luminosity to potential drop in a very simple manner. We present the result here and explain its origin in more detail below. Figure 2.4 shows the spin-down luminosity as a function of potential drop for inclination angles $\alpha = 0, 30, 60, 90°$. Spin-down luminosity increases with

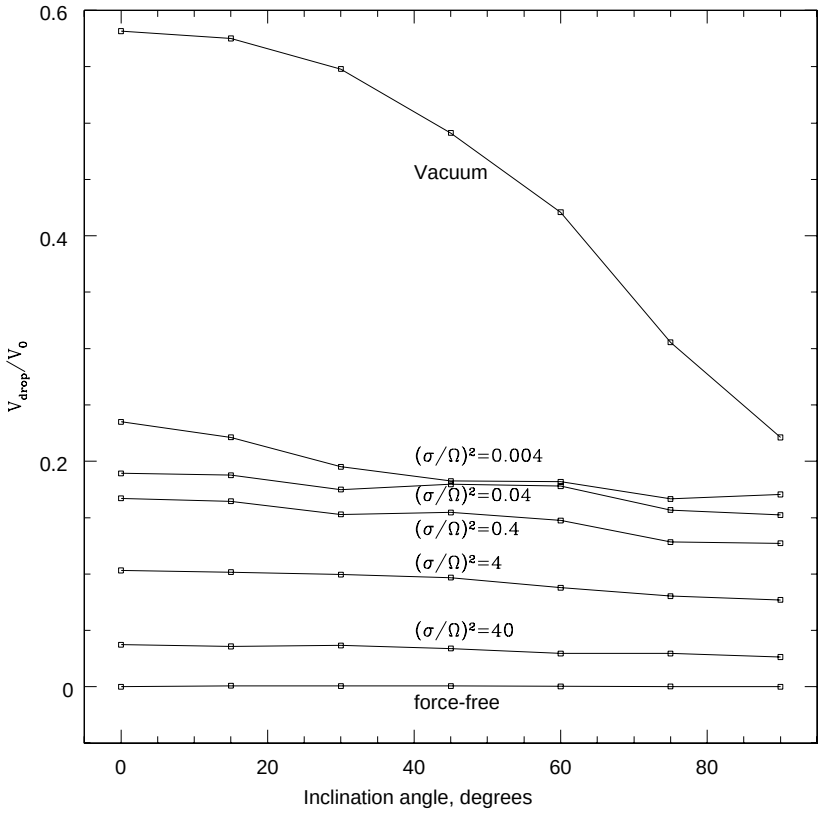

Figure 2.3: Open field line potential drop with inclination angle for force-free, a sequence of resistive, and vacuum dipoles. Results are normalized to $V_0 = |\mu|/R_{\rm LC}R_*$. For $(\sigma/\Omega)^2 > 0.04$ the potential drop is relatively independent of inclination angle.

increasing inclination angle and with decreasing field line potential drops. We fit the spin-down curves in Figure 2.4 with the linear relation

$$\frac{L}{L_0} = 0.9\left(1 - \frac{V_{\rm drop}}{0.2V_0}\right) + 1.1\sin^2\alpha\,,\ 0 < V_{\rm drop} < 0.2V_0. \tag{2.31}$$

This formula applies only to the domain for which we have data shown with solid lines in Figure 2.4, i.e., $0 < V_{\rm drop}/V_0 < 0.2$. A similar spin-down formula was constructed by Contopoulos & Spitkovsky (2006) for the case of a finite gap at the base of the open field lines in a force-free magnetosphere. The spin-down was also found to be linear in the potential drop in the gap but had a different slope and angular dependence of the form $(1 - V_{\rm drop}/V_{\rm pc})\cos^2\alpha + \sin^2\alpha$. This

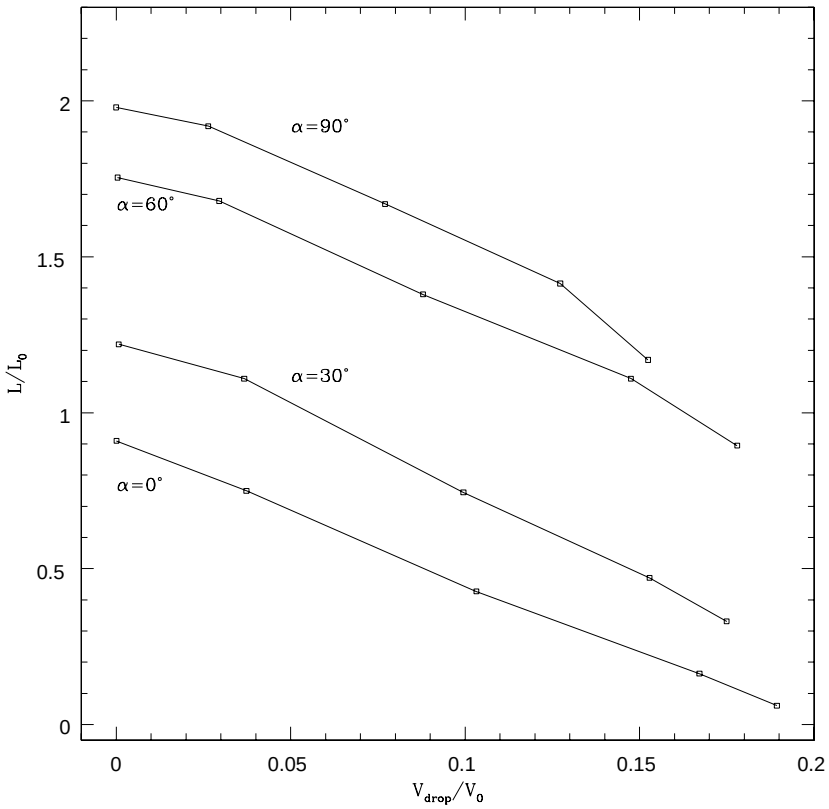

Figure 2.4: Spin down dependence on the open field line potential drop for a sequence of different inclination angles, $\alpha = 0°, 30°, 60°$, and $90°$. Potential drop is normalized to $V_0 = |\mu|/R_{\rm LC}R_*$ and luminosity to 3/2 the spin-down of the orthogonal vacuum rotator. For $V_{\rm drop}/V_0 < 0.2$ spin-down falls linearly with potential drop.

angular dependence was not a rigorous derivation, but a prediction based on aligned force-free and orthogonal vacuum limits. We note that our spin-down formula reduces to the force-free spin-down formula from S06 within error bars when $V_{\rm drop}/V_0 = 0$.

For $V_{\rm drop}/V_0 > 0.2$ the dependence of spin-down on the potential drop enters a different regime (see dotted lines in Figure 2.4). We do not provide a fit here, as potential drop no longer scales with V_0 at high inclination angle. The potential drop along field lines in this regime is due to the reemergence of the vacuum electric fields as conductivity is reduced. There are three contributions to the vacuum electric field which are provided by the quadrupolar surface charge on a finite-radius star and by central and surface monopolar charges. The central monopolar

component provides part of the radial electric field needed for corotation of the magnetized stellar interior. If the star initially is uncharged (as is assumed in our simulations), a surface charge of opposite sign compensates the net charge of the interior of the star (see Michel & Li, 1999 for thorough discussion). This surface charge, together with the induced quadrupolar surface charge from corotation, can leave the star and be redistributed throughout the magnetosphere when conductivity is turned on, or when the work function of the surface is low. Such redistribution lowers the maximum available potential drop.

The available monopolar surface charge varies with inclination as $\cos\alpha$ (Michel & Li, 1999), so the potential drop associated with it disappears for orthogonal rotators. Hence, the value $V_{\rm drop} \sim 0.2V_0$ for the vacuum 90° rotator in Figure 2.3 represents the quadrupolar contribution to the potential drop. At conductivity $(\sigma/\Omega)^2 \sim 0.04$, the maximal potential drop is close to the orthogonal vacuum rotator value of $V_{\rm drop} \sim 0.2V_0$ at all inclination angles. Qualitatively, magnetospheres with finite conductivity $(\sigma/\Omega)^2 > 0.04$ can effectively redistribute the surface charges and maintain the linear relationship between the maximal potential drop and the spin-down luminosity. Below $(\sigma/\Omega)^2 = 0.04$, the surface charge redistribution is incomplete (the monopolar surface charge is concentrated closer to the star in the corotating steady-state solution) and the curves in Figure 2.3 gain a tilt more reminiscent of the vacuum solution. The potential drops are not constant with inclination angle at a given conductivity, and the linear relation (2.31) no longer holds. We have explicitly verified that by the end of the simulation these solutions reached steady-state in the corotating frame.

Redistribution of surface charge in near-vacuum magnetospheres also affects the spin-down power. Looking back at Figure 2.2 and the piecewise linear relations (2.27), we see that the final 30% of the spin-down transition between force-free and vacuum rotators occurs for $(\sigma/\Omega)^2 < 0.04$. Despite the fact that potential is no longer constant with angle for each value of the conductivity in this regime, the transition in spin-down is still continuous and smooth.

3.1 Numerical effects on spin-down power

In principle we should be measuring spin-down values at the stellar surface, but there is uncertainty in the stellar spin-down measurement due to stair-stepping at the spherical inner boundary on our Cartesian grid. To avoid this issue, we measure spin-down at the light cylinder. Dissipation of Poynting flux inside the light cylinder artificially suppresses our spin-down estimates measured at the light cylinder, though. We quantify these uncertainties by computing the force-free spin-down values measured both on the star and at the light cylinder. The true force-free spin-down luminosity likely falls within the shaded grey region in Figure 2.2 bounded by the stellar and light cylinder spin-down values. There is also a deviation from the vacuum Deutsch solution for our zero conductivity solution (compare dashed line to $(\sigma/\Omega)^2 = 0$ line). This difference is due to our boundary conditions at the star. The smoothing of the fields across the stair-stepped boundary leads to small charge bleed-off from the inside of the star to the outside. The first term in equation (2.3) is then not identically zero just outside the star even in the $\sigma = 0$ case. This numerical artifact does not affect the solutions with high conductivity when the physical current exceeds the numerical smoothing current, but below $(\sigma/\Omega)^2 = 4 \times 10^{-3}$ it can influence the field structure and slightly modify the spin-down power.

To better understand these numerical issues it is helpful to look at the run of Poynting flux with radius. In Figure 2.5 we show the Poynting flux integrated over spherical shells of varying radii for force-free, vacuum and a range of resistive solutions with $\alpha = 60^\circ$. The results are normalized to the force-free value at the star, located at $R_* = 0.375 R_{LC}$, and we show the run of Poynting flux with spherical radius out to $2.25 R_{LC}$. The vacuum and $(\sigma/\Omega)^2 = 0$ curves are flat, indicating negligible dissipation of Poynting flux with increasing radius, but there is an offset between the curves that we attribute to our imperfect inner boundary. Force-free is in principle dissipationless and should have the run of Poynting flux flat with radius. As was argued above, our method for cleaning parallel electric field in force-free simulations is resistive and causes Poynting flux to slope downwards with increasing radius. Inside the light cylinder, the drop is due to artificial volume $\mathbf{j} \cdot \mathbf{E}$ dissipation above the polar caps. This dissipation varies with magnetic

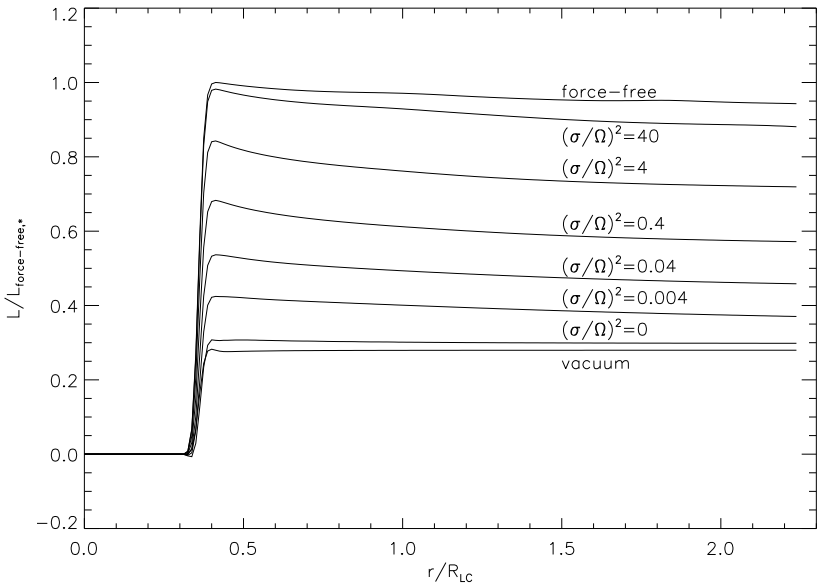

Figure 2.5: Poynting flux with radius for force-free, a sequence of resistive, and vacuum dipoles inclined at $\alpha = 60°$. The resistive Poynting flux values slope downwards with increasing radius, reflecting magnetospheric dissipation. Results are normalized to the force-free spin-down value on the star.

inclination angle and is responsible for the varying width of the gray error band with angle for force-free solutions in Figure 2.2. Outside the light cylinder, the drop in Poynting flux is due to it disappearing into the current sheets.

The resistive runs in Figure 2.5 have Poynting flux dropping with increasing radius, as we expect, indicating dissipation throughout the magnetosphere. Inside the light cylinder the dissipation is primarily physical $\mathbf{j} \cdot \mathbf{E}$ dissipation above the polar caps. There is also some dissipation due to the disappearance of Poynting flux into the current layer, though significantly weaker in magnitude as compared to the volume $\mathbf{j} \cdot \mathbf{E}$ dissipation. Outside the light cylinder the Poynting flux is dissipated in the current sheets. The dissipation of Poynting flux is strongest at intermediate conductivities, $\sigma/\Omega \sim 1$. At higher conductivities, the currents are more ideal and dissipationless, and at lower conductivities, dissipation is reduced because the conduction currents are weaker. Volume dissipation introduced in our resistive simulations implies that the light cylinder measurements of Poynting flux in Figure 2.2 underestimate the true spin-down power of

the resistive solutions, and should be treated as being within the error bands similar to the gray band of the force-free solution.

4 Discussion

We have presented a continuous one-parameter family of pulsar magnetosphere solutions that span the range between the vacuum and force-free limits. Each solution of the family is characterized by the value of the conductivity parameter, σ/Ω, which is related to the maximum potential drop that a test particle can experience as it moves along field lines, $V_{\rm drop}$. The zero conductivity limit, $\sigma/\Omega \to 0$, $V_{\rm drop} \to V_{\rm drop,vac}$, yields the vacuum magnetosphere. It shows a substantial effective potential drop that makes up a significant fraction of the rotation-induced potential difference between the pole and the equator of the star (20−60% depending on the inclination). The high conductivity limit, $\sigma/\Omega \to \infty$, yields essentially an ideal force-free magnetosphere. Unlike in vacuum, abundant magnetospheric charges short out any potential differences along field lines, leading to vanishing effective potential drop, $V_{\rm drop,ff} \to 0$. While in the vacuum case nearly all field lines, even those that extend beyond the light cylinder, eventually return to the star and are formally closed, in the ideal force-free case a fraction of field lines open up and reach infinity. Our simulations show that resistive high-σ pulsars spin down at least 3 times faster than resistive low-σ and vacuum pulsars (for the same value of inclination), in agreement with earlier ideal force-free simulations (S06). Our resistive solutions bridge the gap between the force-free and vacuum limits by having intermediate values of major magnetospheric parameters, such as effective potential drop, $0 < V_{\rm drop} < V_{\rm drop,vac}$, the fraction of open field lines, and the spin-down rate.

Before discussing possible observational implications of these solutions, we note that our approach to modeling resistive pulsar magnetospheres is quite simplistic: we use a form of Ohm's Law in which we neglect several terms (Meier, 2004) and we assume constant conductivity σ/Ω throughout all space. The finite bulk conductivity used in this work can be thought of as not due to collisions, but due to the insufficient plasma supply in the magnetosphere that cannot short

out all the accelerating fields. It is possible that real magnetospheres have a lower (anomalous) conductivity in the current layer and the current sheet than in the rest of the magnetosphere. We might also expect a lower value of conductivity on the open field lines than on the closed field lines. Since our models do not explicitly model the plasma fluid (Section 1), the plasma velocity component along the direction of magnetic field is unconstrained, which necessitates the choice of a frame in which to write the Ohm's Law. We choose the so-called minimum velocity frame, which has a number of attractive properties (see Section 2), yet this is not a covariant choice. With these important caveats in mind, let us now for the sake of argument take our model seriously as a description of pulsar magnetosphere and consider the consequences.

Addition of resistivity can, in principle, allow the detailed study of pulsar spin-down and the determination of pulsar braking indices. For a spin-down law $\Omega = \Omega(t)$, the braking index is defined as $n \equiv \Omega\ddot{\Omega}/\dot{\Omega}^2$. In order to measure a braking index numerically, we run a series of simulations for different values of angular frequency, Ω, and map out the dependence, $L(\Omega)$. We find that $L(\Omega) \propto \Omega^4$ for both purely force-free and vacuum solutions, which translates into a value of the braking index, $n = 3$, as we will see below. This is larger than the range of observed values, $n \simeq 2.5{-}2.8$ (Livingstone et al., 2007). One way to lower the braking index is to allow the evolution of the extent of the magnetosphere (the radius of the Y-point) to lag behind the outward expansion of the light cylinder due to spin down (e.g., Contopoulos & Spitkovsky, 2006). The extent of the Y-point is controlled by the rate of reconnection at the edge of the magnetosphere. We calculated the braking index in our simulations by comparing the magnetosphere with constant conductivity spun up to different periods, and we do not find significant deviations from $n = 3$. This rapid spinup biases our answer, however, because the Y-point extends to the light cylinder within one rotation period. It is not entirely clear that we would obtain the same braking index if we allowed the pulsar period to increase during a single simulation as the pulsar spins down and the light cylinder slowly recedes. The extent of the Y-point may depend on the past history of the pulsar. To do this calculation, we need to increase the pulsar period several times within a single simulation and measure the resulting spin-down luminosity after each increase. We must also ensure that the reconnection at the Y-point is controlled by the resistivity we impose

and not by numerical effects. A more accurate braking index calculation would require much longer simulations, and possibly higher spatial resolution near the Y-region.

Another possibility that can affect the braking index is the evolution of conductivity with time. Such time-evolution translates into evolution in pulsar dimensionless luminosity, $\ell = L/L_0$ (see Figure 2.2), and leads to $n \neq 3$:

$$n = \frac{\Omega\ddot{\Omega}}{\dot{\Omega}^2} = 3 - 2\frac{\mathrm{d}\ell/\mathrm{d}t}{\ell/\tau}, \tag{2.32}$$

where $\tau = P/2\dot{P}$ is the pulsar age, and we used the scaling, $L_0 \propto \Omega^4$. If dimensionless plasma conductivity does not change in time, $\sigma/\Omega =$ constant, then $\ell =$ constant and equation (2.32) gives $n = 3$. Purely force-free and purely vacuum pulsars, discussed above, fall into this category. As a pulsar ages, it is natural to expect that its plasma supply depletes and the pulsar becomes progressively more vacuum-like: in other words, both σ/Ω and ℓ decrease in time (see Figure 2.2). For such pulsars, $\mathrm{d}\ell/\mathrm{d}t < 0$, and equation (2.32) gives $n > 3$. Of course, the converse is also true, and the braking index lower than 3 would result if a pulsar becomes progressively more force-free–like, i.e., if pulsar dimensionless luminosity increases in time, $\mathrm{d}\ell/\mathrm{d}t > 0$. Presently, however, it is not clear why such behavior would be physically expected. Thus, the addition of bulk resistivity does not seem to easily solve the braking index puzzle, and a more elaborate explanation is still required.

Our resistive magnetospheres naturally lend themselves to modeling the sub-pulse drift phenomena observed in a number of pulsars (see e.g., Asgekar & Deshpande, 2001; Deshpande & Rankin, 2001; Rankin et al., 2003; Contopoulos & Spitkovsky, 2006). The following discussion takes place in the corotating frame, where we define electromagnetic fields by equations (2.28) and (2.29). In this frame there is transverse particle drift with velocity of order $v_{\mathrm{drift}} \sim \mathbf{E}_\perp \times \mathbf{B}/B^2$. This drift velocity can be thought of as the minimal velocity of particles, ignoring motion along the magnetic field lines. The transverse electric field $\mathbf{E}_\perp$ reverses sign through the axis of maximum potential drop, and so there is rotation of field lines about this axis. In general, this axis is not in the direction of the magnetic moment, and in fact does not even

need to be a straight line. If we consider a simplified picture of the magnetosphere in which there is no parallel electric field in the closed field line region, the potential drop across open field lines is given roughly by the longitudinal potential drop along field lines. The differential rotation can then be roughly related to the longitudinal potential drop by

$$\Delta\Omega = \Delta V_{\rm drop}/(B_p R_\perp^2) = \Delta V_{\rm drop}/\Psi_{\rm cap}. \tag{2.33}$$

In the laboratory frame, the field lines are undergoing rotation about the pulsar spin axis (with the angular frequency Ω), and in addition they are rotating differentially around the maximum potential axis in a retrograde sense. The differential rotation of plasma can explain sub-pulse emission features that drift with respect to the otherwise periodic light curve of the pulsar. Our result is in contrast to the standard picture in which the plasma precesses about the magnetic axis (Ruderman & Sutherland, 1975). The magnetic colatitude parameter in the cartographic transformation of, e.g. Deshpande & Rankin (2001), must then be modified accordingly.

To better visualize the differential rotation in the context of our resistive magnetospheres, consider the full drift velocity

$$v_{\rm drift} = \frac{\mathbf{E}\times\mathbf{B}}{B^2 + E_0^2}c, \tag{2.34}$$

again in the corotating frame. Figure 2.6 shows magnetic field lines in the $\mu - \mathbf{\Omega}$ plane for a 60° inclined dipole at conductivity $(\sigma/\Omega)^2 = 4$. Color indicates out-of-plane drift velocity, with red (blue) representing velocity into (out of) the page. The velocity has been rescaled by raising its magnitude to the 1/2 power. The axis of maximum potential extends from the star roughly halfway between the rotation and magnetic axes. The differential rotation of plasma about this axis is denoted by the transition from red to blue across the axis, indicating a reversal in the sign of the out-of-plane drift velocity. Note that the axis bends off in the direction of open field lines beyond the light cylinder. These corotating frame drift velocities can be quite substantial. The maximum illustrated drift velocity occurs near the current sheets and corresponds to a velocity of $0.8c$. The differential rotation is much stronger than that implied by sub-pulse drift, but we expect the qualitative features of differential rotation to persist in solutions with more realistic

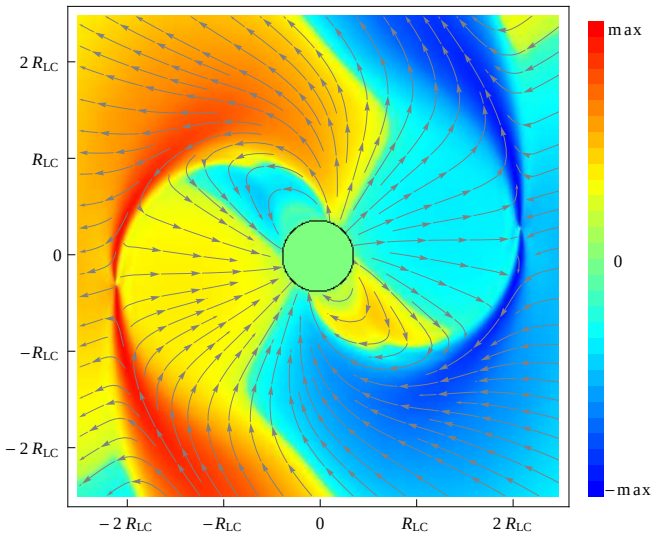

Figure 2.6: Magnetic field lines in the $\mu - \mathbf{\Omega}$ plane for a 60° inclined dipole at conductivity $(\sigma/\Omega)^2 = 4$. Color represents the out-of-plane drift velocity in the corotating frame, with blue color representing the out of the page direction. There is retrograde differential rotation about the axis with maximum potential drop, situated roughly halfway between the rotation and magnetic axes when inside the light cylinder, as well as about the boundary of the closed field line region. The maximum value on the color table corresponds to a drift velocity of $0.8c$.

open field line potential drops. At lower conductivities the magnitude of differential rotation about the axis of maximum potential drop increases, and the conductivity is a parameter that can be tuned to attempt to match observed sub-pulse emission features.

Incidentally, the bundle of field lines surrounding the axis of the maximum potential corresponds to the field lines that carry the largest distributed current density on the polar cap (see Figure 4 in Bai & Spitkovsky 2010). If the strength of the current is associated with radio emission, then the core emission would have a centroid that is offset from the magnetic pole. The offset could be as large as half of the polar cap radius. This would introduce potentially significant modifications to the polarization sweep of the core radio emission and cause deviations from the expected S-curve of Radhakrishnan & Cooke (1969). For a number of pulsars, it would imply differences in the inclination and viewing angles inferred from the shape of the polarization sweep.

We conclude with a discussion of ways to improve our method. In Chapter 3 we will generalize our assumption that σ/Ω is constant in the magnetosphere. In addition to having higher

conductivity in the closed zone, we will experiment with prescriptions for anomalous resistivity in the current sheet in Chapter 4. These improvements will yield a more realistic magnetospheric structure, that can be accurate enough for geometrical modeling of gamma-ray light curves from pulsars. The gamma-ray pulse formation is sensitive to the geometry of the magnetosphere, and, in particular, to the field lines near the current sheet (Bai & Spitkovsky, 2010). Deviations from the force-free geometry may be important for modeling the light curves of older pulsars which require wider gaps in the outer-gap models (Watters et al., 2009).

Bibliography

Asgekar, A. & Deshpande, A. A. 2001, MNRAS, 326, 1249

Bai, X.-N. & Spitkovsky, A. 2010, ApJ, 715, 1282

Beskin, V. S. 2010, MHD Flows in Compact Astrophysical Objects

Blandford, R. D. 2002, in Lighthouses of the Universe: The Most Luminous Celestial Objects and Their Use for Cosmology, ed. M. Gilfanov, R. Sunyeav, & E. Churazov, 381

Contopoulos, I. & Kalapotharakos, C. 2010, MNRAS, 404, 767

Contopoulos, I. & Kazanas, D. 2002, ApJ, 566, 336

Contopoulos, I., Kazanas, D., & Fendt, C. 1999, ApJ, 511, 351

Contopoulos, I. & Spitkovsky, A. 2006, ApJ, 643, 1139

Deshpande, A. A. & Rankin, J. M. 2001, MNRAS, 322, 438

Elsasser, W. M. 1946, Physical Review, 70, 202

Grøn, Ø. 1984, International Journal of Theoretical Physics, 23, 441

Gruzinov, A. 1999, ArXiv Astrophysics e-prints

—. 2005, Physical Review Letters, 94, 021101

—. 2007, ArXiv e-prints

—. 2008, ArXiv e-prints

Livingstone, M. A., Kaspi, V. M., Gavriil, F. P., Manchester, R. N., Gotthelf, E. V. G., & Kuiper, L. 2007, Ap&SS, 308, 317

Lyutikov, M. 2003, MNRAS, 346, 540

McKinney, J. C. 2006, MNRAS, 368, L30

Meier, D. L. 2004, ApJ, 605, 340

Michel, F. C. & Li, H. 1999, Phys. Rep., 318, 227

Osherovich, V. A. & Gliner, E. B. 1988, Sol. Phys., 117, 391

Palenzuela, C., Lehner, L., Reula, O., & Rezzolla, L. 2009, MNRAS, 394, 1727

Radhakrishnan, V. & Cooke, D. J. 1969, Astrophys. Lett., 3, 225

Rankin, J. M., Suleymanova, S. A., & Deshpande, A. A. 2003, MNRAS, 340, 1076

Ruderman, M. A. & Sutherland, P. G. 1975, ApJ, 196, 51

Schiff, L. I. 1939, Proceedings of the National Academy of Science, 25, 391

Spitkovsky, A. 2006, ApJ, 648, L51

Taflove, A. & Hagness, S. 2005, Computational Electrodynamics: The Finite-Difference Time-Domain Method, 3rd edn. (Norwood, MA: Artech House)

Tchekhovskoy, A., McKinney, J. C., & Narayan, R. 2009, ApJ, 699, 1789

Watters, K. P., Romani, R. W., Weltevrede, P., & Johnston, S. 2009, ApJ, 695, 1289

Chapter 3

On the Spin-Down of Intermittent Pulsars

1 Introduction

Pulsars spin down due to torques exerted by currents flowing on the surface of the neutron star. In the absence of magnetospheric plasma, the pulsar spins down due to magneto-dipole radiation (Michel, 1991; Beskin et al., 1993). Magnetospheric plasma allows for currents that can produce additional spin-down torques (Spitkovsky, 2006, hereafter S06), so variations in plasma supply can potentially modulate pulsar spin-down.

Several classes of pulsars have been identified that may exhibit such modulation. Nulling pulsars have radio emission that appears to shut off for a few to several tens of rotation periods. Since radio emission is presumably tied to the magnetospheric plasma, the nulling suggests that some process is affecting the plasma supply and/or currents above the polar caps (Wang et al., 2007; Zhang et al., 2007; Timokhin, 2010). Intermittent pulsars switch between an "on", radio-loud, state in which they behave like normal radio pulsars, and an "off", radio-quiet, state in which they produce no detectable radio emission for long periods of time. This process may be an extreme manifestation of nulling. The first two intermittent pulsars with published data have quite different duty cycles: PSR B1931+24 (Kramer et al., 2006, hereafter K06), with a period $P \approx 0.8$ s, cycled through the "on"–"off" sequence of states approximately once a month, whereas PSR J1832+0029 (Lyne, 2009), with a period $P \approx 0.5$ s, kept quiet for nearly two years between "on" cycles of unknown length. The spin-down rate for each of these pulsars is larger in the "on" state than in the "off" state by a factor $f_{\mathrm{on}\to\mathrm{off}} \simeq 1.5$. Figure 3.1 shows the change in pulse frequency over time and the timing residual for the intermittent pulsar from K06. A third

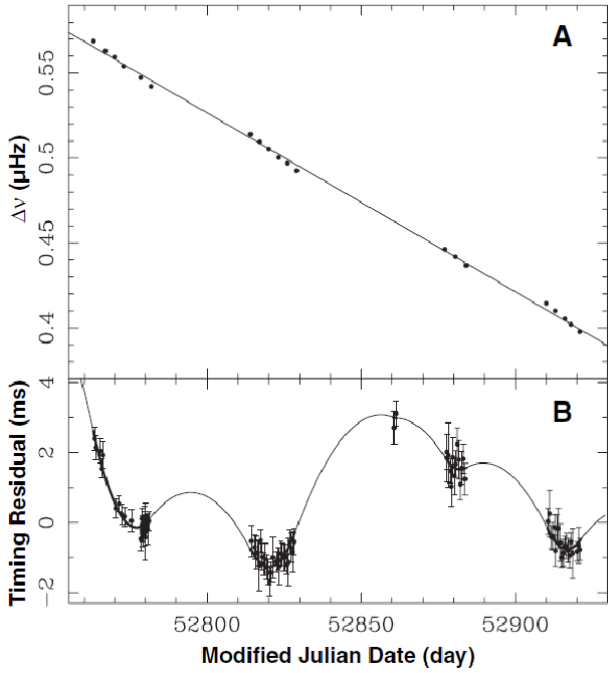

Figure 3.1: Change in frequency over time and timing residual for the intermittent pulsar from Kramer et al. (2006). The Spin-down rate is different when radio is observed and when no radio is observed.

intermittent pulsar, PSR J1841-0500, was not detected for over 1.5 years between "on" cycles, one of which appears to have lasted for at least a year (Camilo et al., 2012). This pulsar seems to have a spin-down ratio between "on" and "off" states of $f_{\mathrm{on}\to\mathrm{off}} \simeq 2.5$. Such substantial differences in spin-down rates suggest that the pulsar magnetosphere undergoes a dramatic reconfiguration as it transitions between the "on" and "off" states, yet such a transition was reported for PSR B1931+24 to take place in just over 10 pulsar periods.

Intermittent pulsars offer a unique testbed of pulsar theory. K06 first proposed that in the "on" state plasma fills the pulsar magnetosphere and supports plasma processes that produce radio emission. The pulsar transitions to the "off" state when open field lines become depleted of charged radiating particles. K06 approximated the spin-down rate in the "off" state by the spin-down of a vacuum dipole and estimated the extra plasma currents needed to account for the observed spin-down of the "on" state. It is not clear, however, whether a working pulsar should naturally yield the required on-off spin-down ratio of this picture. The simplest model for the

"on" state is the force-free magnetosphere, which has abundant charges everywhere. The force-free spin-down rate is larger than the vacuum spin-down rate by a factor $f_{\rm ff\rightarrow vac} = (1+\sin^2\alpha)/(2/3\sin^2\alpha)$ (S06) that is greater than or equal to 3 for all inclination angles α. This is clearly incompatible with the observed values, $f_{\rm on\rightarrow off} \simeq 1.5-2.5$ (Beskin & Nokhrina, 2007; Gurevich & Istomin, 2007). This suggests that, perhaps, we do not understand the spin-down power of the "off" state.

The shutoff of pair formation as the intermittent pulsar switches "off" allows plasma to escape along the open field lines, but the plasma in the closed zone is supplied by a different mechanism and/or confined by the geometry of the field lines. This is an important physical effect that was not included in previous work (K06; Li et al. 2012;Kalapotharakos et al. 2012). The currents and charges associated with plasma trapped in the closed zone can increase the spin-down in the "off" state even if the open field lines are empty. Thus, in this paper, we model the "off" state using a simple two-zone prescription in which the closed zone is highly conducting and the open field lines are vacuum-like. We run resistive force-free simulations to directly solve for the magnetospheric geometry in the "on" and "off" states and test whether this model can produce the observed intermittent pulsar spin-down ratios. In Section 2 we describe the numerical code and setup. Section 3 illustrates our intermittent pulsar solutions and shows the spin-down results. Section 4 provides a brief summary of our results and their observational implications.

2 Setup

We employ the same three-dimensional numerical code from Chapters 1 and 2 that implements the finite difference time-domain scheme (Taflove & Hagness, 2005) scheme to evolve electromagnetic fields from Maxwell's equations,

$$\begin{aligned} \partial_t \mathbf{E} &= c\nabla\times\mathbf{B} - 4\pi\mathbf{j}, \\ \partial_t \mathbf{B} &= -c\nabla\times\mathbf{E}, \end{aligned} \tag{3.1}$$

where the current $\mathbf{j}$ is given by

$$\mathbf{j} = \rho\mathbf{v} + \sigma\mathbf{E}_{\rm fluid}. \tag{3.2}$$

The fluid velocity $\mathbf{v} = c(\mathbf{E}\times\mathbf{B})/(B^2 + E_0^2)$ is the generalized drift velocity, $\mathbf{E}_{\rm fluid} = \gamma(\mathbf{E} + \mathbf{v}\times\mathbf{B})$ is the fluid frame electric field, $\gamma = (1 - v^2/c^2)^{-1/2}$, E_0 is the magnitude of $\mathbf{E}_{\rm fluid}$, ρ is the charge density, and σ is the plasma conductivity in the fluid frame. The central region of our grid is occupied by a conducting spherical star of radius R_*, rotating at angular velocity $\mathbf{\Omega}$, with embedded dipole field of magnetic moment μ inclined relative to the rotation axis by angle α. We resolve the light cylinder $R_{\rm LC} = c/\Omega$ with 80 cells and set $R_* = 30$ cells. We have verified that our solutions are converged with spatial resolution, as well as run sufficiently long so as to reach a steady state in the frame corotating with the pulsar.

In Chapter 2 we showed that our resistive force-free formulation can capture both the vacuum and ideal force-free limits by varying the conductivity parameter. We model the "on" state as a magnetosphere with high conductivity $(\sigma/\Omega)^2 = 40$, our fiducial value representing force-free–like conditions for $R_*/R_{\rm LC} = 3/8$. This is preferable to using an ideal force-free formulation as in S06, because our high conductivity solutions are numerically cleaner, especially in the current sheets. We model the "off" state as having conducting and vacuum-like regions separated sharply at the boundary of the closed field line region, which we approximate as the closed field lines of the force-free "on" state. Nonrotating dipole magnetic field lines are traced by the curves $s = s_0 \sin^2\theta$ (Michel & Li, 1999), where θ is the angle from the magnetic axis, s is spherical radius, and s_0, the maximum perpendicular distance of a field line from the magnetic axis, specifies which field line is under consideration. The closed field lines in the force-free solutions are typically stretched in the direction perpendicular to the magnetic axis as compared to vacuum dipole closed field lines. We use the surface $s = R_{\rm LC}\sin^2\theta(R_{\rm LC}\sin^2\theta/R_*)^k$ to demarcate the closed field line region. The exponent k is set at each inclination angle to best match the shape of the force-free closed zone (see Section 3 for illustrations of these demarcation surfaces), and the half-angle size of the conducting polar cap is given by $\theta_{\rm pc} = \sqrt{R_*/R_{\rm LC}}$. Interior to the demarcation surface, we set $(\sigma/\Omega)^2 = 40$, as in the "on" state. Exterior to the demarcation surface, we set $(\sigma/\Omega)^2 = 0.04$, a

fiducial value representative of vacuum-like conditions for $R_*/R_{\rm LC} = 3/8$. We pick this value over $\sigma/\Omega = 0$ for better numerical accuracy when computing the field geometry. This choice of conductivity on open field lines and the exact shape of the demarcation surface have minimal effect on spin-down (see Section 3).

3 Results

Figure 3.2 shows magnetic field lines in the $\mu - \mathbf{\Omega}$ plane for inclined dipoles at $\alpha = 30^\circ$ (top), 60° (middle), 90° (bottom). Color is representative of the out-of-plane magnetic field. To improve contrast, the color table shows values up to 30% of the maximum out-of-plane field, and a square root stretching is applied to the data. The left column shows the "off" state with abundant plasma in the closed zone but a shortage of plasma along open field lines. The red curves indicate the boundary between the conducting and vacuum-like regions in the illustrated cross-section of the magnetosphere. The right column shows the "on" state with abundant plasma everywhere. The magnetospheres in the "on" state are force-free–like, with conduction currents flowing along open field lines. The current returns through the current sheets and along the boundary of the closed field line region in the current layers. Gross features of the magnetosphere in the "off" state are vacuum-like, with large closed field line region and displacement currents contributing to spin-down. For reference we show a representative vacuum solution with inclination angle $\alpha = 60^\circ$ in Figure 3.3. There are a number of important differences that distinguish the intermittent "off" state from the vacuum solutions. The current from toroidal advection of charged plasma in the closed zone leads to greater magnetic flux passing through the light cylinder and a larger fraction of open field lines. Further, poloidal conduction currents are present even outside the conducting closed zone. They are due primarily to the fluid advection term $\rho\mathbf{v}$ in the current and lead to greater magnetic field sweepback and stronger current sheets than in pure vacuum solutions.

Figure 3.4 shows the spin-down luminosity, normalized by L_0 (where L_0 is 3/2 times the power of the orthogonal vacuum rotator with finite $R_*/R_{\rm LC} = 3/8$), as a function of inclination angle for both the "on" and "off" states of the magnetosphere. Spin-down luminosity is calculated as the

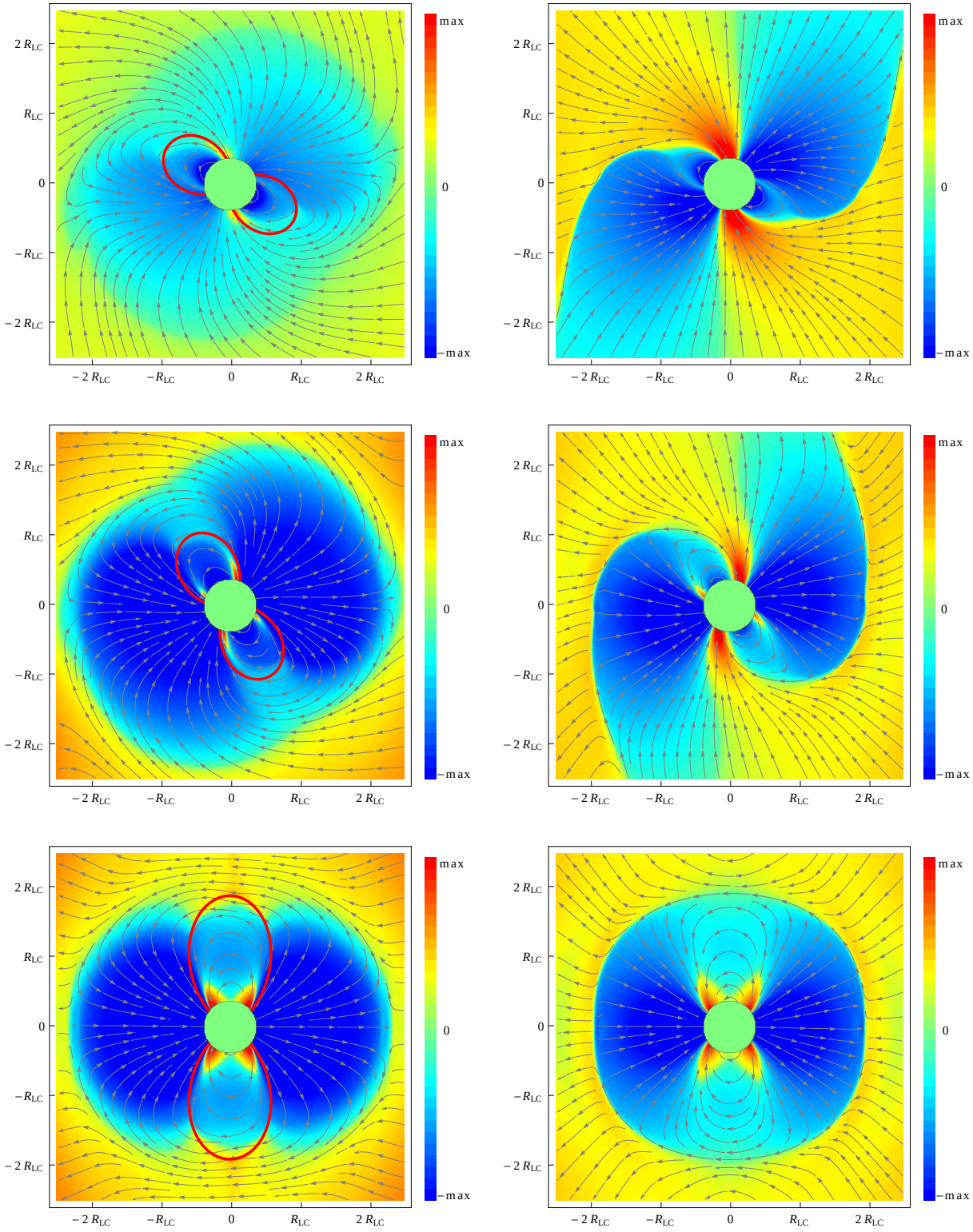

Figure 3.2: Magnetic field lines in the $\mu - \mathbf{\Omega}$ plane for inclined dipoles at $\alpha = 30°$ (top), $\alpha = 60°$ (middle), $\alpha = 90°$ (bottom). Color is representative of out-of-plane magnetic field into (red) and out of (blue) the page. The left column shows the "off" state with abundant plasma in the closed zone and vacuum-like conditions along open field lines. The red curves indicate the intersection with the $\mu - \mathbf{\Omega}$ plane of the demarcation surface between these distinct conducting and vacuum-like regions. Gross features of the magnetosphere in the "off" state are vacuum-like, but the "off" states have more magnetic flux passing through the light cylinder and stronger magnetic field sweepback than vacuum solutions. The right column represents the "on" state with abundant plasma everywhere.

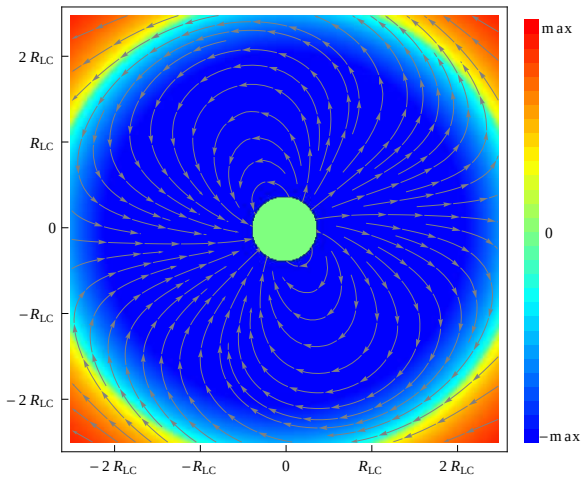

Figure 3.3: Magnetic field lines in the $\mu - \mathbf{\Omega}$ plane for a vacuum inclined dipole at $\alpha = 60°$. Color is representative of out-of-plane magnetic field into (red) and out of (blue) the page. There is large closed field line region, and displacement currents circulate and contribute to spin-down.

surface integral of the Poynting flux over a sphere of radius $R_{\rm LC}$. We also show for reference the spin-down for the vacuum solution in the total absence of plasma. The "on" state spin-down is essentially the force-free spin-down. There is an uncertainty of roughly 10% of L_0 in the force-free spin-down at low inclination angles due to stellar boundary effects and unphysical dissipation above the polar caps (see Chapter 2 Section 3.1). The spin-down in the "off" state lies between the force-free and vacuum spin-down values at all inclination angles. The spin-down of the aligned rotator in the "off" state is small, as the displacement currents are zero and large-scale conduction currents are weak. The open field lines carry minimal Poynting flux. Inclined dipole open field lines carry Poynting flux, however, and the larger magnetic flux passing through the light cylinder in the "off" state results in higher spin-down than in the vacuum solution. This increase in Poynting flux over vacuum spin-down in the "off" state is largest at high inclination angles, where the open field lines in the vacuum solutions carry the most Poynting flux. The advective poloidal conduction currents also lead to higher spin-down since they cause larger magnetic field sweepback than in vacuum solutions. We evaluated the relative contributions of these two effects to higher spin-down over vacuum solutions by killing the advection current term $\rho\mathbf{v}$ outside the

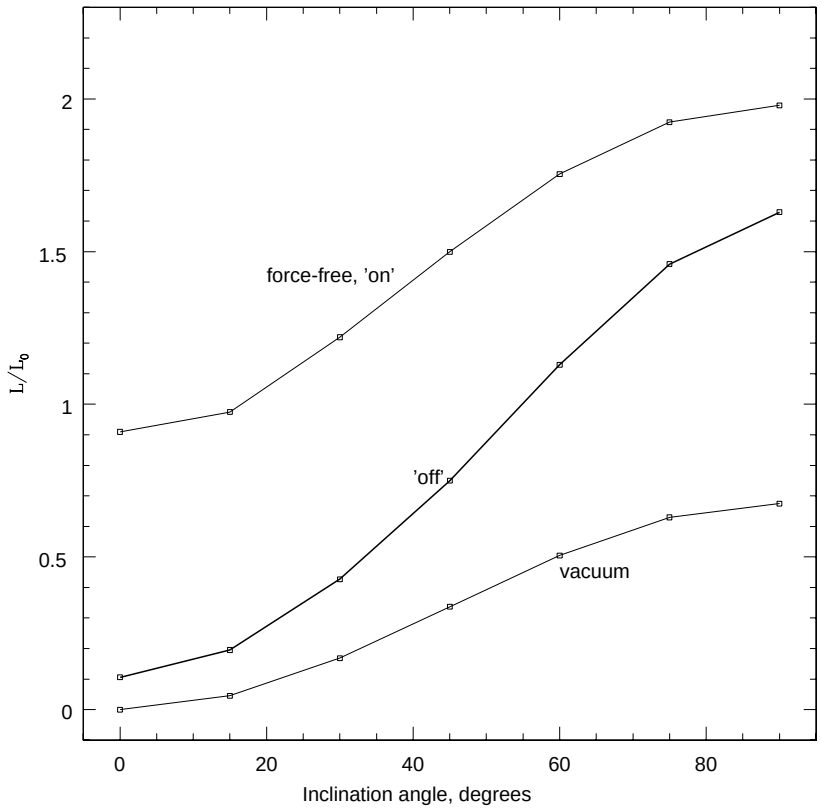

Figure 3.4: Spin-down luminosity dependence on inclination angle for the force-free–like "on" state, the "off" state, and the vacuum solution. The "off" state spin-down naturally lies between the force-free and vacuum spin-down values for all inclination angles. spin-down is normalized by 3/2 times the spin-down power of the orthogonal vacuum rotator.

closed zone. The larger magnetic flux passing through the light cylinder is responsible for upwards of two-thirds of the increase in Poynting flux over vacuum spin-down in the "off" state.

The spin-down in the simulated "off" state is relatively insensitive to the size of the conducting closed zone. We varied the volume of the conducting closed zone by a factor of a few while keeping the size of the polar cap fixed, and we find that spin-down changes by less than 20% of L_0 at all inclination angles. It is not the total size of the conducting closed zone, but rather its extent on the stellar surface that is more important in determining the gross magnetospheric properties. Blocking radial currents near the stellar surface limits the large-scale poloidal current circuit. Spin-down also depends very weakly on the fiducial values of σ/Ω that we pick to

represent highly conducting and vacuum conditions. We checked this by setting the conductivity to $\sigma/\Omega = 0$ instead of $(\sigma/\Omega)^2 = 0.04$ along open field lines, and we find that the resulting spin-down is offset by less than 20% of L_0 for all inclination angles. The aligned "off" state spin-down drops to zero in this case, as we expect, since the large-scale conduction currents have been eliminated. We also tried setting the closed zone to have conductivity $(\sigma/\Omega)^2 = 20$ instead of $(\sigma/\Omega)^2 = 40$, and spin-down results change by less than 10% of L_0 at all inclination angles.

The most relevant observational parameter in the context of intermittent pulsars is the ratio of spin-down power in the "on" and "off" states, $f_{\rm on\rightarrow off}$. Figure 3.5 shows this ratio for our models. We emphasize that these models provide a physically well-motivated set of solutions to describe both the "on" and "off" states of intermittent pulsars. Assuming a uniform distribution of pulsar inclination angles, we expect two-thirds of intermittent pulsars to have $f_{\rm on\rightarrow off}$ between $1.2 - 2.9$. Known intermittent pulsars fall within this range (K06, Lyne, 2009; Camilo et al., 2012). Uncertainties in the exact charge configuration and charge transport properties in the "off" state magnetosphere imply error bars associated with our calculation of the ratio $f_{\rm on\rightarrow off}$. The uncertainty is of order 10% at inclination angle $\alpha = 90^\circ$ and rises with decreasing inclination angle to a factor of order 2 at $\alpha = 30^\circ$. Below $\alpha = 30^\circ$ the ratio $f_{\rm on\rightarrow off}$ rises above 3 due to the small spin-down of the aligned rotator in the "off" state, but there are large uncertainties in the exact value of $f_{\rm on\rightarrow off}$ in this regime.

A major improvement of our intermittent pulsar models over existing work lies in the treatment of accelerating potential drops, which can be used as a fiducial measure of energy gain as particles fly away from the stellar surface. We define the potential drops as in Chapter 2, i.e., as the line integral along magnetic field lines of the corotating electric field $\mathbf{E}' = \mathbf{E} + (\mathbf{\Omega} \times \mathbf{r}) \times \mathbf{B}/c$. In ideal force-free solutions the potential drops vanish, as $\mathbf{E} \cdot \mathbf{B} = 0$, but they increase monotonically with increasing bulk resistivity. Previously, we implemented a constant conductivity σ/Ω throughout the magnetosphere. As the polar cap played no fundamental role in these models, open field line potential drops were generally limited by the full pole-to-equator potential drop, yielding unphysically large potential drops of order 10^{16} V. Our new models for the "off" state introduce conducting plasma in the closed field line zone,

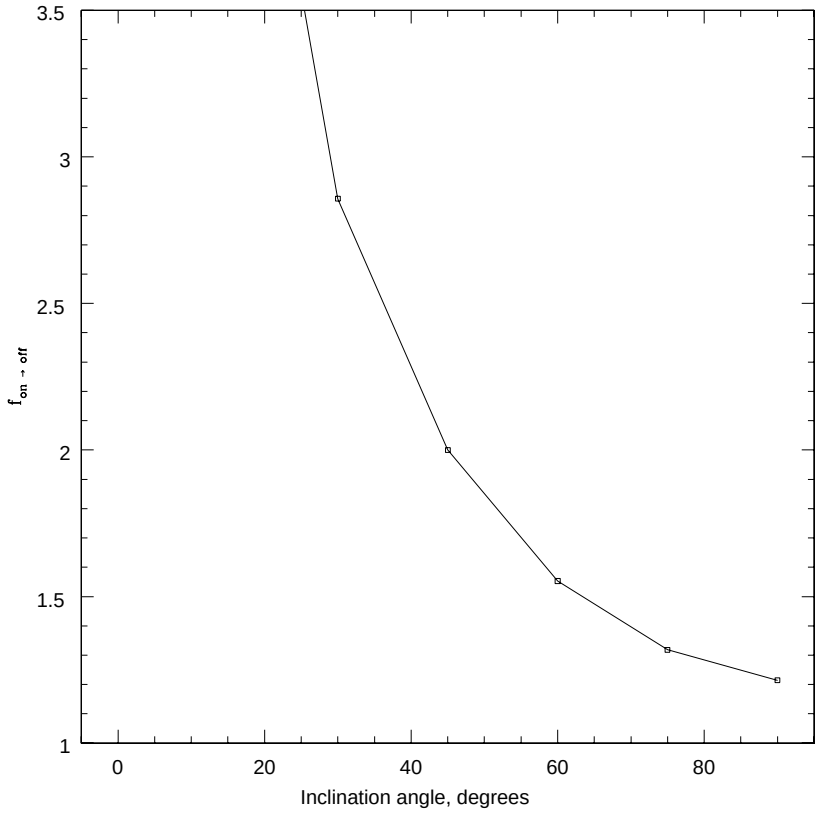

Figure 3.5: The ratio of spin-down power between the "on" and "off" states, $f_{\rm on\to off}$, as a function of inclination angle. We obtain $f_{\rm on\to off} \sim 1.2 - 2.9$ for $\alpha > 30^\circ$. Known intermittent pulsars have $f_{\rm on\to off}$ in this range.

effectively shielding the potential drop there. The potential drops are then limited by the polar cap potential drop $V_{\rm pc} = |\mu|/R_{\rm LC}^2$. For typical pulsars with periods $P \sim 1$s, we obtain characteristic potential drop of $\sim 10^{12}$ V, more in line with expectations.

4 Discussion

We have developed an improved numerical method for solving pulsar magnetospheres with resistivity, and we apply it to describe intermittent pulsars in a self-consistent manner. In the "on" state, plasma is abundant everywhere, and the instabilities in this plasma generate coherent radio emission. In the "off" state plasma has leaked off the open field lines, suppressing the open

field line currents. The radio emission is hence shut off. Plasma remains trapped in the closed zone, however, and the current from toroidal advection of these charges leads to spin-down values that are a factor of ~ 2 larger than vacuum values. This allows us to naturally produce spin-down ratios $f_{\rm on\rightarrow off} \sim 1.2 - 2.9$ for inclination angle in the range $\alpha = 30^\circ - 90^\circ$, consistent with observations, and we obtain realistic values for accelerating potential drops, $V_{\rm drop} \sim 10^{12}$ G. In our model the spin-down ratio $f_{\rm on\rightarrow off}$ takes on its minimum value at $\alpha = 90^\circ$ and increases monotonically with decreasing inclination angle. Hence, given an observed spin-down ratio $f_{\rm on\rightarrow off}$ for an intermittent pulsar, we can predict, within errors, the pulsar's inclination angle. Alternatively, given the pulsar inclination angle from, e.g., polarization vector sweep data, we can predict the spin-down ratio $f_{\rm on\rightarrow off}$ if the pulsar displays clear "on" and "off" states. A verification of our predictions would lend strong support to the idea that abrupt changes in plasma supply on open field lines can play an important role in determining the emission properties and spin-down rates of real pulsars.

One potential limitation of our models relates to the spatial distribution of conductivity in the magnetosphere. We specify only a conducting torus located in the plane perpendicular to the magnetic axis. In fact, rotation of a conducting neutron star leads to unipolar induction, and domes of negative charge form above the magnetic poles even in the absence of a pair cascade if the work function of the surface is low (Krause-Polstorff & Michel, 1985a,b; Pétri et al., 2002b,a; Spitkovsky & Arons, 2002; Spitkovsky, 2004). We explored this effect by prescribing additional conducting domes above the magnetic poles, setting $(\sigma/\Omega)^2 = 40$ interior to the surfaces specified by $s = R_{\rm LC} \cos^2\theta$. Spin-down values increase at all inclination angles by an offset of less than 20% of L_0, but the spin-down ratio $f_{\rm on\rightarrow off}$ remains within the errors quoted in Section 3.

It is important to note that at present the precise mechanism by which the plasma supply is turned on and off is still unclear. In at least one intermittent pulsar case the switching between different spin-down rates is quasi-periodic (K06), implying that the processes supplying and limiting plasma alternately recur. Intermittency may actually be the same basic process as nulling, the crucial difference being that the "off" state lasts months to years instead of from a few rotation periods up to days. In this light, timing noise can in some instances be caused by nulling

events that are not resolved by the observations. The pulsar timing data in the Jodrell Bank data archive are typically smoothed and do not resolve features that occur on time scales shorter than a few tens of days (see Hobbs et al., 2010; Lyne et al., 2010). Suppose recurring nulling events last for an accumulated time that is of order a few percent of the time that the pulsar behaves normally. Since in our model the spin-down in the "off" state is typically of order 1/2 that in the "on" state, the resulting spin-down luminosity in a state with unresolved nullings could easily be modified by $\sim 1\%$. Lyne et al. (2010) established a connection between timing noise and mode changing, when the pulse profile of the pulsar changes to a different shape, but they do not see mode changing in all pulsars that exhibit timing noise. It is possible that some of these pulsars undergo nulling events, which leads to variation in spin-down rate and the observed timing noise. The mode changing is presumably due to changes in the magnetospheric configuration. One possibility is that it is an intermediate state between our "on" and "off" states in which some but not all of the plasma along open field lines has leaked away. These intermediate states could lead to a number of observed pulsar features including jitter, subpulse drift, precursors, and interpulses, though such ideas are at present still speculative. Another possible cause for changing pulse profiles is the presence of multiple components to the emission, e.g., the core and conal components, and one or more components being modified or shut off by changes in plasma supply.

If the "on" and "off" states of the pulsar can last anywhere from a few periods to years, it is further conceivable that Rotating Radio Transients (RRATs) are another manifestation of the process captured by our model. RRATs are rotating neutron stars that occasionally emit pulses, usually isolated, but in a few instances in a string of several (McLaughlin et al., 2006; Palliyaguru et al., 2011). It has not been ruled out that RRATs are an extreme form of nulling, and we envision RRATs as pulsars that spend the majority of their time in our "off" state, but turn "on" from time to time and emit pulses. If future observations are able to establish a more definitive link between the seemingly disparate processes of intermittency, nulling, timing noise, and RRATs, it would be an important step in our understanding of pulsar physics.

Bibliography

Beskin, V. S., Gurevich, A. V., & Istomin, Y. N. 1993, Physics of the pulsar magnetosphere

Beskin, V. S. & Nokhrina, E. E. 2007, Ap&SS, 308, 569

Camilo, F., Ransom, S. M., Chatterjee, S., Johnston, S., & Demorest, P. 2012, ApJ, 746, 63

Gurevich, A. V. & Istomin, Y. N. 2007, MNRAS, 377, 1663

Hobbs, G., Lyne, A. G., & Kramer, M. 2010, MNRAS, 402, 1027

Kalapotharakos, C., Kazanas, D., Harding, A., & Contopoulos, I. 2012, ApJ, 749, 2

Kramer, M., Lyne, A. G., O'Brien, J. T., Jordan, C. A., & Lorimer, D. R. 2006, Science, 312, 549

Krause-Polstorff, J. & Michel, F. C. 1985a, MNRAS, 213, 43P

—. 1985b, A&A, 144, 72

Li, J., Spitkovsky, A., & Tchekhovskoy, A. 2012, ApJ, 746, 60

Lyne, A., Hobbs, G., Kramer, M., Stairs, I., & Stappers, B. 2010, Science, 329, 408

Lyne, A. G. 2009, in Astrophysics and Space Science Library, Vol. 357, Astrophysics and Space Science Library, ed. W. Becker, 67

McLaughlin, M. A., Lyne, A. G., Lorimer, D. R., Kramer, M., Faulkner, A. J., Manchester, R. N., Cordes, J. M., Camilo, F., Possenti, A., Stairs, I. H., Hobbs, G., D'Amico, N., Burgay, M., & O'Brien, J. T. 2006, Nat, 439, 817

Michel, F. C. 1991, Theory of neutron star magnetospheres

Michel, F. C. & Li, H. 1999, Phys. Rep., 318, 227

Palliyaguru, N. T., McLaughlin, M. A., Keane, E. F., Kramer, M., Lyne, A. G., Lorimer, D. R., Manchester, R. N., Camilo, F., & Stairs, I. H. 2011, MNRAS, 417, 1871

Pétri, J., Heyvaerts, J., & Bonazzola, S. 2002a, A&A, 387, 520

—. 2002b, A&A, 384, 414

Spitkovsky, A. 2004, in IAU Symposium, Vol. 218, Young Neutron Stars and Their Environments, ed. F. Camilo & B. M. Gaensler, 357

Spitkovsky, A. 2006, ApJ, 648, L51

Spitkovsky, A. & Arons, J. 2002, in Astronomical Society of the Pacific Conference Series, Vol. 271, Neutron Stars in Supernova Remnants, ed. P. O. Slane & B. M. Gaensler, 81

Taflove, A. & Hagness, S. 2005, Computational Electrodynamics: The Finite-Difference Time-Domain Method, 3rd edn. (Norwood, MA: Artech House)

Timokhin, A. N. 2010, MNRAS, 408, L41

Wang, N., Manchester, R. N., & Johnston, S. 2007, MNRAS, 377, 1383

Zhang, B., Gil, J., & Dyks, J. 2007, MNRAS, 374, 1103

Chapter 4

High-Energy Radiation from Current Sheets and Current Layers in Pulsar Magnetospheres

1 Introduction

The Fermi γ-ray Space Telescope (GST) has recently discovered > 100 pulsars with γ-ray emission in the GeV range (Abdo et al., 2010, 2013). This γ-ray emission can constitute a large fraction of the pulsar spin-down power, and may yield important clues about plasma processes operating in the magnetosphere of the pulsar. A number of authors have suggested that particles are accelerated in vacuum gaps and that the high-energy emission comes from slot gaps (SG; Arons & Scharlemann, 1979; Arons, 1983; Muslimov & Harding, 2003, 2004; Dyks & Rudak, 2003; Dyks et al., 2004) or outer gaps (OG; Cheng et al., 1986a,b; Romani & Yadigaroglu, 1995; Yadigaroglu, 1997; Cheng et al., 2000) in the outer magnetosphere. An alternative possibility is that the high-energy emission comes from the extended pulsar current sheet, which provides a large reservoir of energy via reconnection of magnetic fields (e.g., Bai & Spitkovsky, 2010b,a; Kirk et al., 2002; Arka & Dubus, 2013; Pétri, 2013). In order to differentiate between these models, it would be helpful to have a better quantitative understanding of how accelerating electric fields and variations in the plasma supply affect particle motions in the magnetosphere.

Until very recently, quantitative solutions of the global magnetospheric structure existed only for the vacuum limit (Deutsch, 1955) and for the limit of abundant plasma in force-free electrodynamics (see Contopoulos et al. 1999; Gruzinov 2005; Timokhin 2006; McKinney 2006; Parfrey et al. 2012; Palenzuela 2013 for aligned rotators, and Spitkovsky 2006; Kalapotharakos & Contopoulos 2009; Pétri 2012b for pulsars with arbitrary inclinations) or ideal

magnetohydrodynamics (Komissarov 2006 in 2D; Tchekhovskoy et al. 2013 in 3D). The real pulsar magnetosphere is likely operating somewhere in between these limits, with various accelerating gaps, regions of pair production, and strong current sheets likely causing local violations of the ideal MHD constraint, $\mathbf{E} \cdot \mathbf{B} = 0$. Knowing the structure of the magnetosphere, including such non-ideal effects, would be very useful for calculating the properties of pulsar emission. Indeed, currently the ideal force-free models that include the back-reaction of plasma currents on the field structure lack any accelerating fields by construction, and thus cannot be used to directly predict the spectra of γ-ray radiation observed by the Fermi GST.

Nonzero accelerating electric fields can be incorporated into our models by allowing for plasma resistivity (Kalapotharakos et al., 2012b,a, 2013). Force-free methods formally lack plasma velocities along magnetic field lines, and so there is an ambiguity in determining the fluid frame in which to specify Ohm's Law. Nevertheless, we have recently developed a resistive force-free method that smoothly transitions between the vacuum and force-free limits as we vary the plasma conductivity, and also has the extremely useful property of remaining stable in ordinarily discontinuous current sheets (c.f. Chapter 2). We use these resistive solutions to examine models in which the high-energy emission from γ-ray pulsars comes from regions with strong accelerating electric fields: the current layer interior to the light cylinder $R_{\rm LC} = c/\Omega$ and the reconnecting current sheet beyond the light cylinder.

The γ-ray pulsar light curves often have a characteristic strongly double peaked profile, sometimes with bridge emission seen between the first and second γ-ray peaks (Abdo et al., 2010, 2013). In many cases the first γ-ray peak trails the radio emission by a small phase lag, ~ 0.15 P, where P is the pulsar period, with γ-ray peaks widely separated by ~ 0.45 P. The data further indicate that the γ-ray peak separation decreases as the phase lag of the first γ-ray peak from the radio increases. In this work we try to explain these basic features of the γ-ray light curves. In Figure 4.1 we reproduce for clarity the radio and γ-ray light curves from a characteristic pulsar, the Vela pulsar, originally seen in Chapter 1.

In Section 2 we describe briefly our numerical code. Section 3 discusses the physical properties of the current sheet. Section 4 provides a number of physically motivated models for particle

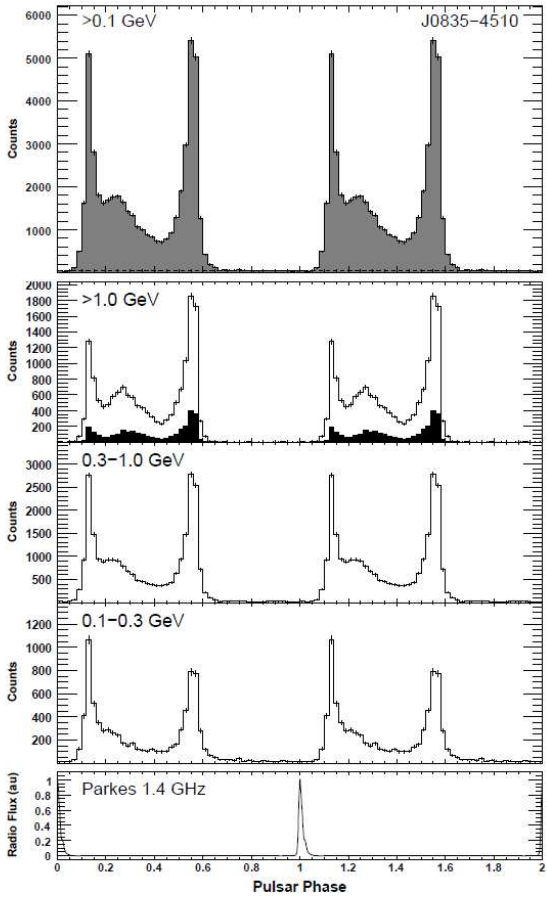

Figure 4.1: Radio and γ-ray light curves for the Vela pulsar from the Fermi GST (Abdo et al., 2010). γ-ray light curves have a characteristic double-peaked shape, with bridge emission seen between the first and second peaks. The first γ-ray peak trails radio emission by 0.13 P.

motion and the associated skymaps and light curves. These models include beaming emission in the direction of the accelerating electric field, the direction of the current, and several directions tangential to the current sheet. They do not reproduce observed light curves, but are instructive in giving hints about what types of models might work. Section 5 explores skymaps and light curves for one such toy model that likely represents a step in the right direction, radial beaming of emission from the current sheet. This model lacks bridge emission between the γ-ray peaks, however, and we believe this emission must arise from interior to the light cylinder. Section 6 presents emission from the current layer interior to the light cylinder, using the methods of Bai & Spitkovsky (2010a). Finally, in Section 7 we combine emission from the current layer interior to the light cylinder and current sheet exterior to the light cylinder in our best working model. This model improves over previous work by considering emission explicitly from inside the sheet, rather than the separatrix layer adjacent to it. Bai & Spitkovsky (2010a) did not consider emission from inside the sheet because current sheets in their ideal force-free solutions were neither smooth nor well-resolved. We conclude in Section 8 with a brief discussion of our results and their implications.

2 Numerics

We employ the same three-dimensional numerical code from Chapters 1 and 2 that implements the finite difference time-domain scheme (Taflove & Hagness, 2005) scheme to evolve electromagnetic fields from Maxwell's equations,

$$\begin{aligned} \partial_t \mathbf{E} &= c\nabla \times \mathbf{B} - 4\pi \mathbf{j}, \\ \partial_t \mathbf{B} &= -c\nabla \times \mathbf{E}, \end{aligned} \tag{4.1}$$

where the current $\mathbf{j}$ is given by

$$\mathbf{j} = \rho \mathbf{v} + \sigma \mathbf{E}_{\text{fluid}}. \tag{4.2}$$

The fluid velocity $\mathbf{v} = c(\mathbf{E} \times \mathbf{B})/(B^2 + E_0^2)$ is the generalized drift velocity, $\mathbf{E}_{\rm fluid} = \gamma(\mathbf{E} + \mathbf{v} \times \mathbf{B})$ is the fluid frame electric field, $\gamma = (1 - v^2/c^2)^{-1/2}$, E_0 is the magnitude of $\mathbf{E}_{\rm fluid}$, ρ is the charge density, and σ is the plasma conductivity in the fluid frame. Unlike in ideal force-free electrodynamics, our resistive current remains stable in current sheets and allows for nonzero parallel electric fields. The central region of our grid is occupied by a conducting spherical star of radius R_*, rotating at angular velocity $\mathbf{\Omega}$, with embedded dipole field of magnetic moment μ inclined relative to the rotation axis by angle α. We resolve the light cylinder $R_{\rm LC} = c/\Omega$ with 160 cells, set $R_* = 3/8R_{\rm LC}$, $(\sigma/\Omega)^2 = 40$ except where otherwise noted, and run the simulations for 1.5 turns. See Koide (2008) for a more detailed treatment of resistive pair plasmas.

3 Current Sheet

On energetic grounds, it seems quite plausible that the γ-ray emission comes from the current sheet, where there is a vast reservoir of energy available from the reconnection of $\sim 10^6$ G strength magnetic fields. We consider here synchrotron emission processes, as we are concerned primarily with geometric constraints on light curves as opposed to predicting spectral properties of the emission. In the absence of electric fields the synchrotron cooling function is (Rybicki & Lightman, 1979)

$$\Lambda = \frac{4}{3}\sigma_T c \frac{B^2}{8\pi}(\gamma^2 - 1), \tag{4.3}$$

with characteristic photon energy in the absence of bulk beaming

$$\epsilon \sim \gamma^2 \hbar \omega_c = \gamma^2 \hbar \frac{qB}{m_e c} \sim \left(\frac{\gamma}{1000}\right)^2 \left(\frac{B}{10^6 \mathrm{G}}\right) \mathrm{MeV}. \tag{4.4}$$

The extended pulsar current sheet has a special geometric shape, taking, e.g., the form of an archimidean spiral in the equatorial plane of an orthogonal rotator. Figure 4.2 illustrates the 3 dimensional current sheet structure between $r = 1.1 - 2R_{\rm LC}$, along with open field lines anchored to the edge of the north and south polar caps. The left panel shows the 60° degree inclined rotator, and the right panel the 90° degree rotator. Purple and grey colors in Figure 4.2 indicate

positive and negative net local charge density in the current sheet. The kink in the current sheet near the null charge surface, where the charge density vanishes, highlights where the sheet bifurcates into two current layers enclosing the closed field line region. Beyond several light cylinder radii, the field lines and current sheet qualitatively approach the split monopole configuration (Bogovalov, 1999; Kalapotharakos & Contopoulos, 2009), though recent results by Tchekhovskoy et al. (2013) indicate that there are differences in the angular distribution of Poynting flux at large radii. The left panel of Figure 4.3 shows the shape of the current sheet in the $\mu - \mathbf{\Omega}$ plane for a 60 degree inclined spinning dipole with $R_*/R_{\rm LC} = 3/8$ and $(\sigma/\Omega)^2 = 10$, extending out to $\sim 25 R_{\rm LC}$. Streamlines trace magnetic fields in this plane, and color shows RB_ϕ. For reference we show the shape of the current sheet in the same plane for a 60 degree inclined split monopole. We find small quantitative differences in the shape of the current sheet between the two solutions, with the dipole sheet extending closer to the rotation axis for the chosen values of spin and conductivity.

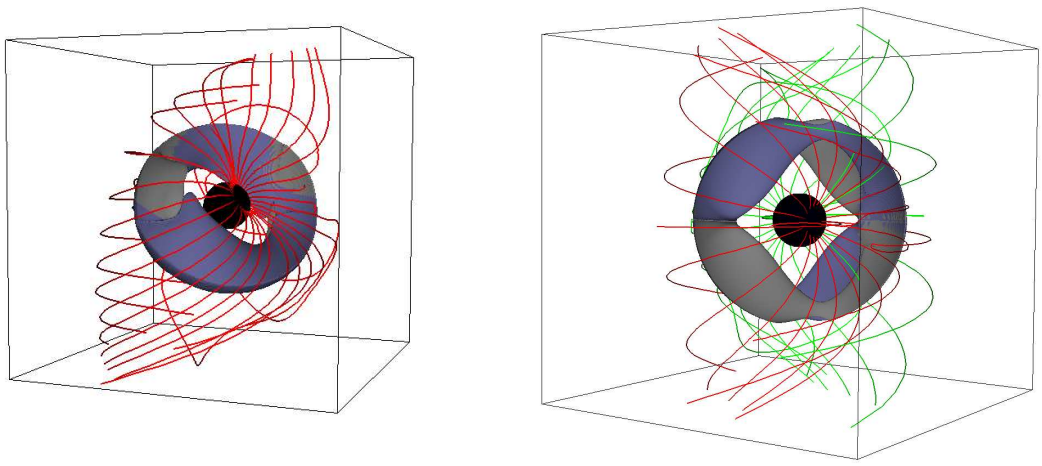

Figure 4.2: Current sheet and open field lines with footpoints near the edge of the polar cap. The left panel shows the 60 degree inclined rotator, and the right panel the 90 degree rotator. Red field lines originate on the north polar cap and green field lines in the right panel originate on the south polar cap. See http://arks.princeton.edu/ark:/88435/dsp01st74cq59f for a movie of the spinning 60 degree inclined pulsar, and http://arks.princeton.edu/ark:/88435/dsp012b88qc316 for a movie of the spinning 90 degree inclined pulsar.

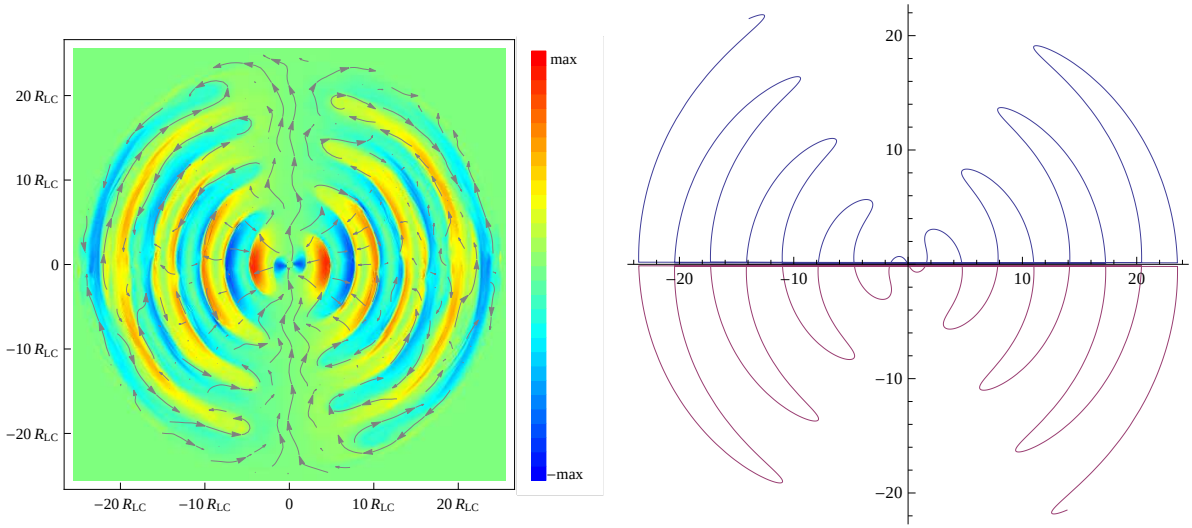

Figure 4.3: The current sheet shape for a 60 degree inclined dipole (left), and a split monopole (right), extending out to $\sim 25R_{\rm LC}$. Color in the left panel is RB_ϕ, and streamlines trace magnetic fields in the $\mu - \mathbf{\Omega}$ plane. The current sheet shape is similar in both cases, but the dipole sheet extends closer to the rotation axis.

In order to study emission from the pulsar current sheet in our resistive force-free pulsar solutions, it is first necessary to isolate the current sheet. There are many potential ways to isolate the current sheet or regions of dissipation, including measuring $\mathbf{j} \cdot \mathbf{E}$, $\nabla \cdot \mathbf{S}$, $\lambda = (j - \rho \mathbf{\Omega} \times \mathbf{r})/B$ (Gruzinov, 2007; Bai & Spitkovsky, 2010a), or Lorentz invariant measures of dissipation (Zenitani et al., 2011). In practice we find the best way to isolate the current sheet is to set a threshold in j_σ/B, where $j_\sigma = \sigma \mathbf{E}_{\rm fluid}$. In the sheet, we expect the current j_σ to remain high and the magnetic field strength to drop to small values. We pick

$$\sigma \mathbf{E}_{\rm fluid}/\mathbf{B} \gtrsim \frac{1}{3}\Omega(\frac{R_{\rm LC}}{R_*})^{3/2} = \frac{1}{3}\sigma\frac{L_{\rm res}}{L_{\rm pc}}, \tag{4.5}$$

where $R_{\rm LC} = c/\Omega$, $L_{\rm res} = c/\sigma$, and $L_{\rm pc} = R_*(R_*/R_{\rm LC})^{1/2}$. We expect the bulk of the magnetosphere to have very high conductivity due to abundant plasma produced above the polar cap in pair cascades. The current sheet may have anomalous resistivity due to plasma instabilities in the sheet, however. A natural model incorporating this effect would introduce localized resistivity in the current sheet. In practice we find that in our framework the electric fields in the

current sheet do not depend strongly on whether a small time-independent resistivity is localized to the sheet or present everywhere throughout the magnetosphere. Hence we introduce a small resistivity everywhere in the magnetosphere by setting $(\sigma/\Omega)^2 = 40$ when $R_*/R_{\rm LC} = 3/8$. We then isolate the current sheet and build emission models using an emissivity that is constant per unit volume except where otherwise noted. The resistivity is chosen to be small enough to ensure that the bulk magnetosphere remains nearly ideal, as otherwise photons no longer pile up into strongly peaked emission.

The most fundamental way to study particle microphysics in relativistic pair plasma current sheets is to run particle-in-cell (PIC) simulations (see e.g., Zenitani & Hoshino, 2001, 2005, 2007, 2008; Zenitani et al., 2009; Bhattacharjee et al., 2009; Bessho & Bhattacharjee, 2005, 2007; Cerutti et al., 2012). Particle energization appears to occur at x-points, where particles are accelerated in the direction of the electric field but eventually deflected in the transverse direction along the upstream magnetic fields in the absence of a guide field. If there is a guide magnetic field in the current sheet, particles are deflected perpendicular to the guide field. In either case particles are trapped in magnetic islands confined to the plane of the current sheet by the strong magnetic field on either side of the sheet. The problem of interest to us, the pulsar current sheet, differs qualitatively from prior PIC current sheet simulations, however. First, particles may have highly relativistic velocities along upstream magnetic field lines as they enter the sheet. Second, there is a Y-surface, where the current sheet bifurcates into two current layers, and where particles can be injected into the current sheet. These properties may lead to interesting particle dynamics and radiation from the current sheet.

Our resistive force-free method does not account for gas pressure and particle velocities, and the current sheet can be described by a purely electromagnetic formalism. This setup is interesting because the mechanical force density on particles can be directly obtained as

$$\frac{d\mathbf{p}}{dt} = -(1/4\pi c)\frac{d}{dt}(\mathbf{E}\times\mathbf{B}) + \nabla\cdot\mathbf{T} = \rho\mathbf{E} + \mathbf{j}\times\mathbf{B}, \tag{4.6}$$

where the components of the Maxwell Stress Tensor are given by

$$T_{ij} = 1/(4\pi)\left(E_iE_j + B_iB_j - 1/2(E^2 + B^2)\delta_{ij}\right). \tag{4.7}$$

With this in mind, our resistive current closure yields an analytic 1D current sheet, which can potentially provide insight on understanding the large scale pulsar current sheet. We solve the stationary Faraday equation,

$$c\nabla \times \mathbf{B} - 4\pi\left(\rho\mathbf{v} + \sigma\mathbf{E}_{\rm fluid}\right) = 0. \tag{4.8}$$

Assuming

$$B_x = B_1 f(z), E_y = kB_1, E_z = \sqrt{1-k^2}B_x, \tag{4.9}$$

where k is the reconnection rate, Faraday's equation becomes

$$f' = \frac{4\pi\sigma}{c}\sqrt{-(1-k^2)f^4 + (1-2k^2)f^2 + k^2}. \tag{4.10}$$

The solution to this equation involves an inverse function and elliptic functions but is straightforward to obtain with numerical methods. The reconnection rate k is a free parameter, and the current sheet thickness $c/4\pi\sigma$ is an independent free parameter. In the simplifying case $k = 1$, the current sheet solution becomes

$$B_x = \begin{cases} B_1\sin(\zeta), & \text{if } -\pi/2 < \zeta < \pi/2 \\ B_1, & \text{if } |\zeta| \geq \pi/2, \end{cases} \tag{4.11}$$

$$E_y = B_1, \tag{4.12}$$

$$j_y = \begin{cases} \sigma B_1\sqrt{1-\sin^2(\zeta)}, & \text{if } -\pi/2 < \zeta < \pi/2 \\ 0, & \text{if } |\zeta| \geq \pi/2, \end{cases} \tag{4.13}$$

where $\zeta = (4\pi\sigma/c)z$. Note that $\mathbf{E} > \mathbf{B}$ in this current sheet, but it remains stable due to the presence of $E_0 = B_1(1 - \sin^2(\zeta))^{1/2}$ in the denominator of the drift velocity. We plot these quantities explicitly in Figure 4.4, where the current has been normalized arbitrarily. For $k \neq 1$, the current sheet is tearing unstable (as in Komissarov et al., 2007), breaking up into magnetic islands and flux ropes. The behavior of the tearing mode is not strictly Lorentz covariant, likely due to our assumption of the minimal velocity drift frame when specifying Ohm's Law. We can still use these ideas to better inform our understanding of plasma physics processes operating in the pulsar magnetosphere. In this paper we explore microphysical and geometric emission models that attempt to utilize the special shape of the current sheet, the orientation of magnetic fields, and the accelerating electric fields.

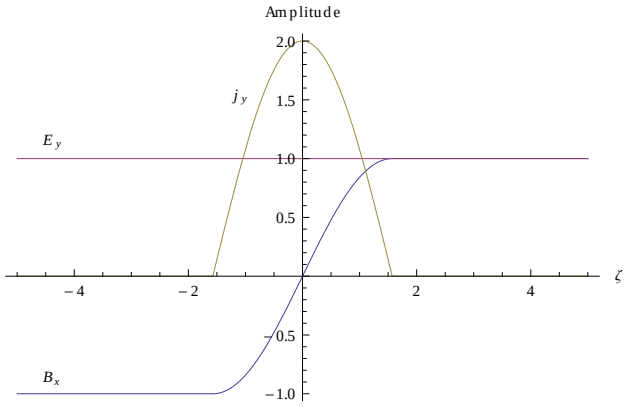

Figure 4.4: Example of an analytic 1D current sheet in our resistive force-free method. This particular sheet is reconnecting at the speed of light. Current has been normalized arbitrarily.

4 Particle Motion

Resistive force-free electrodynamics formally does not account for plasma velocities along fields, and a number of choices can be made when modeling particle motion and emission from the current sheet in our magnetospheres. In this section we consider three different basic models that do not fully reproduce the observations, but help illuminate the physical processes at work.

One choice that makes use of additional information provided by resistive force-free methods is to assume that the bulk fluid motion can be decomposed into a drift velocity and a second component along the accelerating electric field, $\mathbf{E}_{\rm fluid}$. In the Electrodynamics of Massless Charges Gruzinov (2012) assumed that positive and negative charges fly relativistically in opposite directions along $\mathbf{E}_{\rm fluid}$. The counterstreaming beams lead to extra peaks in the emission that do not match the observed light curves, however. A more realistic scenario is that the opposite signed charge carriers are coupled by plasma instabilities (e.g., Two-stream instability; see Lyubarsky 1995) and the bulk fluid moves along the accelerating electric field, directed along the current sheet. The direction of motion is determined by the Lorentz force, and we can choose the velocity down the electric field to either be ultrarelativistic or have magnitude such that the Lorentz force vanishes in the fluid frame. Both choices give similar results because the latter choice generally gives relativistic velocities.

The top panel of Figure 4.5 gives the skymap and light curves for particles in the sheet having ultrarelativistic velocity

$$\mathbf{v} = \frac{\mathbf{E}\times\mathbf{B}}{B^2+E_0^2}c + \frac{E_0\mathbf{E}+B_0\mathbf{B}}{B^2+E_0^2}\frac{\rho}{|\rho|}c. \tag{4.14}$$

The skymap illustrates emission intensity as a function of observer angle, $\xi_{\rm obs}$, the angle between the pulsar rotation axis and the observer, and phase of observation, ϕ. A standard correction for time delay and aberration are used to calculate the phase,

$$\phi = -\phi_v - \mathbf{r}\cdot\hat{\mathbf{v}}/R_{\rm LC}, \tag{4.15}$$

where ϕ_v is the phase of emission, and intensity is proportional to photon count in each bin in $\zeta_{\rm obs}$ and ϕ, divided by a solid angle correction factor (see e.g., Bai & Spitkovsky, 2010a). The pulsar inclination angle in the top panel of Figure 4.5 is $\alpha = 60^\circ$, and the north magnetic pole projects onto the skymap at $\xi_{\rm obs} = 60^\circ$, $\phi = 0^\circ$. Light curves are obtained by picking an observer angle and slicing horizontally across the skymap. There is a strong caustic on the skymap tracing emission from the positively charged portion of the current sheet, and the isolated blobs at phase $\phi \sim 45^\circ, 225^\circ$ come from negatively charged regions of the current sheet. This unconventional

skymap does a poor job at reproducing observed strongly double peaked light curves, however, even when removing the emission from negatively charged regions of the current sheet. Radio emission, if present, likely originates on field lines very close to the magnetic poles, and the phase lag between the γ-ray emission from the caustic and the radio is too large compared to observations (Abdo et al., 2010, 2013). An obvious shortcoming of this prescription is that it does not consider particles' momenta from before they enter the current sheet. These upstream velocities can in principle be highly relativistic and play an important role in determining particle velocities in the current sheet.

An alternative prescription is to consider particles to travel in the direction of the current, an exact assumption in a charge separated magnetosphere. The second panel of Figure 4.5 gives the skymap and light curves for $\alpha = 60^\circ$ when beaming emission along the current from the sheet, whose local net charge is primarily positive. The emission caustic bears some similarities to the case of beaming along $E_{\rm fluid}$, and again does not yield sharply double peaked light curves with the proper phase offset radio emission. Particles do not have to follow the direction of current in a pair plasma, however, because current can be sourced by relative counterstreaming of opposite charges along the accelerating electric field. In fact particle velocities can be quite different from the direction of the current, and we need to incorporate more information about particle velocities into our models.

Particles in the current sheet are confined to the sheet by the strong magnetic fields on either side of the sheet. The magnetic field direction outside the sheet is nearly tangential to the sheet and hence picks a possible direction of motion for particles in the sheet (c.f. Figure 4.2). Beaming emission in this direction is a natural extension of the Separatrix Layer model (Bai & Spitkovsky, 2010a), where particles were assumed to fly outward relativistically along open magnetic field lines near the current sheet. Here we assume particles enter the current sheet and retain their upstream momenta while moving along the sheet. The third panel of Figure 4.5 shows the resulting skymap and light curves for $\alpha = 60^\circ$ when beaming emission along the upstream magnetic field extrapolated into the sheet. We use $\nabla(j_\sigma/B)$ to pick the direction orthogonal to the current sheet, and step a short distance outside the sheet to obtain the upstream magnetic field $\mathbf{B}_{\rm up}$. The

magnetic field lines we select are comparable to the emitting open field lines in the Separatrix Layer model of Bai & Spitkovsky (2010a). Particle motion in this case can be decomposed into the drift velocity plus a component along $\mathbf{B}_{\rm up}$, or equivalently, the corotation velocity plus a component along $\mathbf{B}_{\rm up}$. The caustic in this model has a larger extent in observer angle than in previous models beaming along $E_{\rm fluid}$ or the current. This leads to more realistic light curves and a smaller phase offset between the radio and first γ-ray peak for the light curve at $\xi_{\rm obs} = 60°$.

The current sheet is an inherently 2 dimensional structure, and at each location we can decompose any vector tangential to the sheet into the sum of basis vectors along the upstream $\mathbf{B}_{\rm up}$ and orthogonal to the upstream $\mathbf{B}_{\rm up}$. The addition of a velocity component orthogonal to $\mathbf{B}_{\rm up}$ can in principle shift the phase of the caustic seen in the third panel of Figure 4.5 (c.f. equation 4.15). $\mathbf{B}_{\rm up} \times [\nabla(j_\sigma/B)]$ provides us with such a vector that points along the current sheet and is orthogonal to $\mathbf{B}_{\rm up}$. The fourth panel of Figure 4.5 shows the skymap and light curves when beaming emission along a representative direction $\hat{x} + 0.3\hat{y}$, where $\hat{x}$ is a unit vector pointing outward along $\mathbf{B}_{\rm up}$ and $\hat{y}$ is a unit vector along $[\nabla(j_\sigma/B)] \times \mathbf{B}_{\rm up}$. The caustic is still evident, but there is now significant emission outside the caustic that leads to additional peaks in the light curves. The bottom panel of Figure 4.5 shows the skymap and light curves if we instead beam emission along $\hat{x} - 0.3\hat{y}$. In this case the caustic loses much of its strength and instead has emission concentrated in isolated regions of the skymap. These results suggest that assuming γ-ray emitting particles move in the direction of the upstream magnetic field is potentially justified. In the laboratory frame, these particles move nearly radially outward in straight lines, an idea explored in greater detail in the following section.

5 Toy Models of Current Sheet Emission

5.1 Overview

In this section we explore geometric current sheet emission models, i.e., we are concerned primarily with the direction of motion of highly relativistic γ-ray emitting particles. For simplicity we assume that emitting particles move radially outwards at relativistic speeds. These

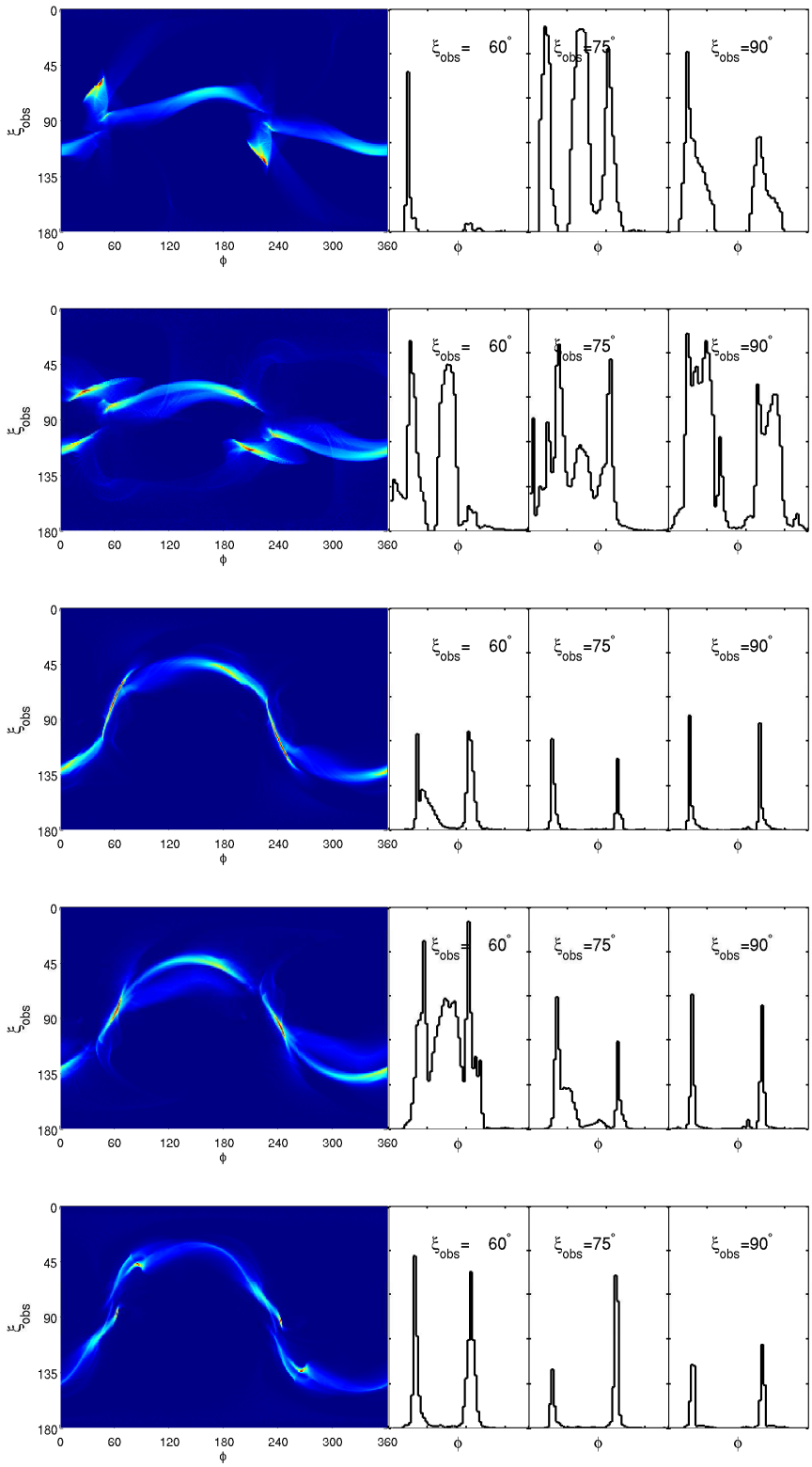

Figure 4.5: Skymaps for emission from the current sheet between $r = 1.1 - 1.5R_{\rm LC}$ for a $\alpha = 60^\circ$ rotator. Emission is beamed along $\mathbf{E}_{\rm fluid}$ (top), along $\mathbf{j}$ (2nd panel), along the upstream magnetic field $\mathbf{B}_{\rm up}$ extrapolated into the sheet (3rd panel), a combination of $\mathbf{B}_{\rm up}$ and $[\nabla(j_\sigma/B)] \times \mathbf{B}_{\rm up}$ (4th panel), and a combination of $\mathbf{B}_{\rm up}$ and $-[\nabla(j_\sigma/B)] \times \mathbf{B}_{\rm up}$ (bottom). Of these models, beaming along $\mathbf{B}_{\rm up}$ works best, producing a strong caustic and reasonable phase offset from possible radio emission at the magnetic poles.

particles remain confined to the sheet as it rotates around the neutron star. Photons emitted along the entire trajectory of a relativistic particle traveling in the sheet will then pile up and arrive at the observer in phase, generating strong peaks in emission. Radial beaming of emission from the current sheet leads to a strong caustic on the skymap, and the phase of the caustic is independent of the distance from the neutron star that emission comes from. We illustrate these points explicitly in the following sections by considering emission from both near the light cylinder and beyond a few light cylinder radii.

5.2 Light Cylinder Region

Beyond the light cylinder in the force-free pulsar magnetosphere the magnetic energy density scales roughly as $u_B = B^2/8\pi \propto 1/R^2$ and pressure scales as $\mathrm{p} \propto B^2 - E^2 \propto 1/R^4$. Hence there is more energy available to accelerate particles closer in to the light cylinder than at larger radii. Previous authors have suggested that emission from close to or in the current sheet near the light cylinder can give rise to the strong caustic and double peaked light curves (Bai & Spitkovsky, 2010a; Arka & Dubus, 2013).

We explore here the physical basis for a model with radial particle motions near the light cylinder. First, particles can get accelerated by $\sim 10^{12}$ V potential drops above the polar cap and fly outwards along open magnetic field lines at high Lorentz factors, with $\gamma > 10^4$ (Timokhin & Arons, 2013). We expect particles just outside the current sheet to have small velocities transverse to the magnetic field lines and hence they will not radiate synchrotron photons. Since there is non-zero dissipation of magnetic energy in the pulsar magnetosphere, these magnetic field lines near the sheet will close through the sheet. Particles will therefore enter the current sheet with large velocities along upstream magnetic fields in the frame corotating with the pulsar. The fluid frame of the current sheet is thus moving close to radially outwards with high Lorentz factor, $\gamma > 10^4$.

In this fluid frame, we expect the current sheet to be tearing unstable, with non-thermal particle acceleration near x-lines. Positrons and electrons will be accelerated in opposite

directions along the accelerating electric field in the fluid frame, but they will eventually be deflected transverse to the x-lines. Particles are injected with a power-law spectrum (Hoshino & Lyubarsky, 2012) into magnetic flux ropes, the 3D analog of plasmoids and magnetic islands in 2D, which move away from x-lines at high velocities and with Lorentz factor $\gamma \sim \sqrt{\sigma_M}$ (Lyubarsky, 2005). In the pulsar magnetosphere the magnetization (Cheng et al., 1986a)

$$\sigma_M = B^2/4\pi\eta\gamma_\eta^2 \sim 10^4, \tag{4.16}$$

where η is the plasma density and γ_η is the bulk Lorentz factor. The flux ropes are confined to the plane of the sheet by the strong magnetization on either side of the sheet, and so these transverse motions are predominantly in both directions along the upstream magnetic field. In the lab frame both these flux ropes are boosted by the bulk fluid motion into the outward direction, one with with Lorentz factor $\gamma \sim 10^2$ and the other with $\gamma \sim 10^6$.

Individual particles confined to a flux rope can also be initially hot, leading to strong synchrotron cooling. A Lorentz factor in the comoving frame of the flux ropes of $\gamma \sim 30$ leads to $\epsilon \sim$ keV emission. Accounting for the bulk motion of the flux ropes, emission will be beamed in the radially outward direction and the most energetic photons will be boosted into the GeV range.

In the top panel of Figure 4.6 we show explicitly the skymap and light curves for a 60 degree inclined rotator, where emission is beamed radially outward from the current sheet between $r = 1.1 - 1.5R_{\rm LC}$. We are essentially projecting the shape of the current sheet onto θ, ϕ coordinates, accounting for light travel time delay effects, and we get a strong caustic in intensity on the skymap. There is evidence of the current sheet bifurcating into two current layers near $\phi \sim 60^\circ, 240^\circ$. The light curves show the characteristic double peaked profile, and the phase lag of the first γ-ray peak from the radio for $\xi_{\rm obs} = 60$ is $\sim 0.22P$, slightly larger than in most observed systems. There is also no evidence of interpulse bridge emission between the first and second γ-ray peaks. Recall that assuming that γ-ray emitting particles are confined to the sheet still allows for one degree of freedom in the direction of particle motion. If particles retain a portion of their velocities down the accelerating electric fields and along x-lines, emission would be less

concentrated in the caustic on the skymap. In practice though it is quite difficult to obtain both the strong single caustic and the smooth bridge emission by allowing for motion along accelerating electric fields in the corotating pulsar frame (c.f. bottom two panels of Figure 4.5).

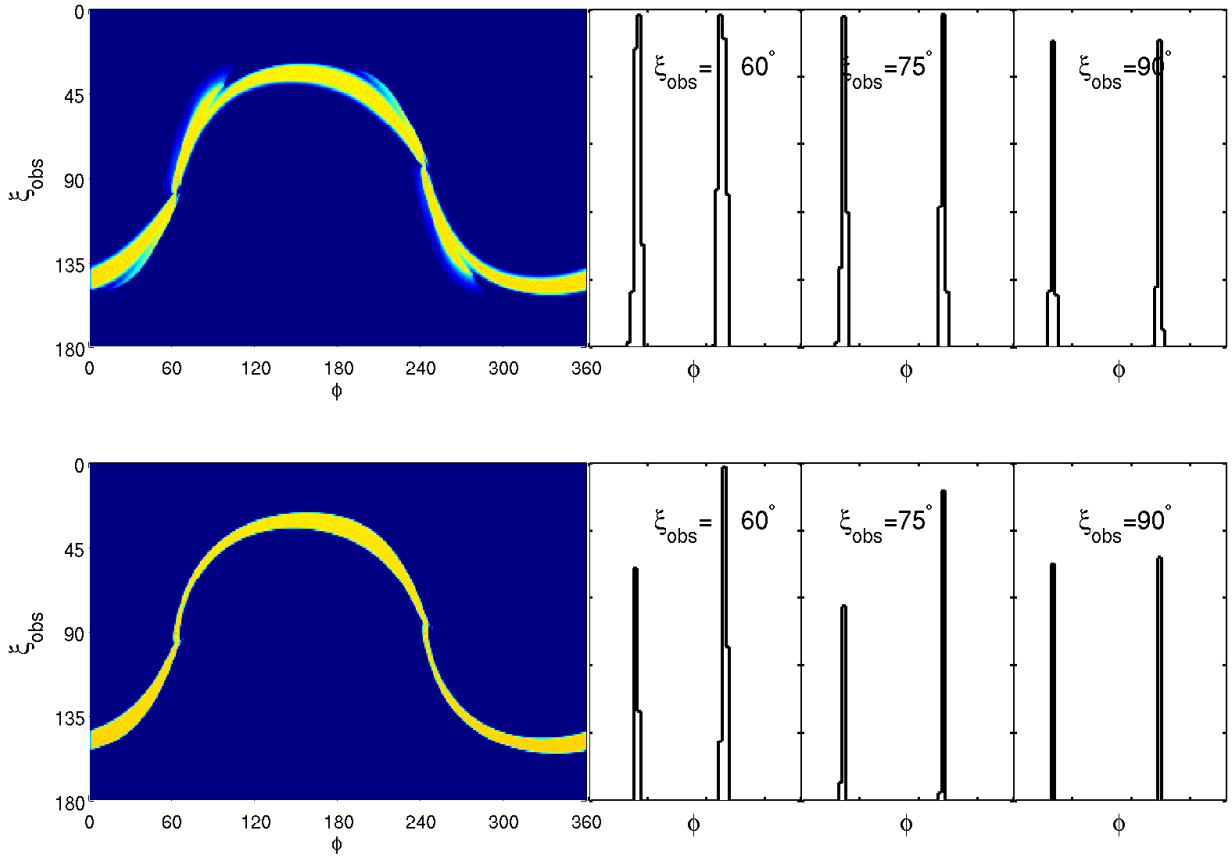

Figure 4.6: Skymaps for radial beaming of emission from the current sheet for a 60 degree inclined rotator. The top panel shows emission from between $r = 1.1 - 1.5R_{\rm LC}$, and the bottom panel shows emission from the wind zone between $r = 2.1 - 2.3R_{\rm LC}$. In both cases there is a strong caustic on the skymap and double peaked light curves for a broad range of inclination angles due to the special geometric shape of the current sheet.

5.3 Wind zone

The wind zone beyond a few light cylinder radii offers an alternative solution for generating strongly double peaked light curves (Coroniti, 1990; Michel, 1994; Lyubarsky & Kirk, 2001; Kirk

et al., 2002; Kirk & Skjæraasen, 2003; Pétri & Kirk, 2005; Pétri, 2009, 2013). One advantage of the wind zone is that radial beaming of emission arises quite naturally. It is instructive here to consider the analytic split monopole solution of Bogovalov (1999), though quantitatively we find small but real differences between the split monopole and dipole solutions (c.f. Figure 4.3 and Tchekhovskoy et al. 2013). The drift velocity is

$$v_{\rm dr} = \Omega R/B^2(-B_\phi B_R \hat{R} + (B_R^2 + B_z^2)\hat{\phi} - B_\phi B_z \hat{z}), \tag{4.17}$$

where

$$B_R = \pm R/(R^2 + z^2)^{3/2}, \tag{4.18}$$

$$B_\phi = \mp (R/R_{\rm LC})/(R^2 + z^2), \tag{4.19}$$

$$B_z = \pm z/(R^2 + z^2)^{3/2}. \tag{4.20}$$

This immediately yields

$$v_\phi/v_r = R_{\rm LC}/R, \tag{4.21}$$

i.e., the velocity is asymptotically radial, and the Lorentz factor of this wind frame grows with cylindrical radius,

$$\Gamma_w = \frac{1}{\sqrt{1 - v_{\rm drift}^2}} = \sqrt{1 + (R/R_{\rm LC})^2} \approx R/R_{\rm LC}. \tag{4.22}$$

Further, any microphysical process driving particles to high transverse velocities along **E** or **B** in the wind frame will be suppressed by Γ_w in the observer frame. The maximum transverse observer frame velocity will be c/Γ_w if $R \gg R_{\rm LC}$. Moreover, as particle velocities parallel to the magnetic field fall with cylindrical radius, reconnection in the observer frame may proceed at a faster rate than closer in to the light cylinder for fixed particle frame reconnection rate. In order to produce 100 MeV emission in the pulsar wind frame at $r = 10R_{\rm LC}$, where $B_w \sim \Gamma_w B_{\rm lab} \sim 10^6$ G, the wind-frame Lorentz factor must be $\gamma_w \sim 10^4$. Several authors have suggested that these

Lorentz factors can be reached in the synchrotron radiation reaction limit, where reconnection heating balances synchrotron cooling losses (Uzdensky & Spitkovsky, 2012; Pétri, 2012a).

The bottom panel of Figure 4.6 gives the skymap and light curves when radiation is beamed in the radial direction from between $r = 2.1 - 2.3R_{\rm LC}$ in the dipole current sheet. The pulsar inclination angle is 60 degrees. The phase of the caustic is the same as in the skymap considering emission between $r = 1.1 - 1.5R_{\rm LC}$ due to the special geometric shape of the current sheet. Strongly doubled peaked light curves will be seen for a range of observer angles, and we note that the phase offset of the first γ-ray peak is more realistic than in models that take emission from the split monopole current sheet (e.g., Arka & Dubus, 2013; Pétri, 2011). We emphasize that there is again no bridge emission, however. Further, it is unclear how to produce bridge emission in the wind zone, where all the plasma is flying radially outwards at relativistic speeds. It seems likely bridge emission is produced closer in to the light cylinder, where Γ_w is not so large and emission is less beamed, or inside the light cylinder.

6 Current Layer

It is actually quite natural to obtain the bridge emission from near the current layer interior to the light cylinder, where magnetic field lines are curved in the poloidal plane. Particles slipping down these field lines can radiate into a range of observer angles, depending on the height above the stellar surface (Bai & Spitkovsky, 2010a). In Figure 4.7 we trace last open field lines centered on $r_{\rm ov} = 0.98$ outward from the stellar surface to the light cylinder. The open volume coordinate $r_{\rm ov}$ of a field line is defined as the fraction of the distance to the edge of the polar cap that the footpoint lies at (e.g., Bai & Spitkovsky, 2010a). We also map these field lines onto the skymap, assuming that emission is beamed in the direction of motion of particles flying relativistically down these field lines. The polar caps form small disks on the skymap centered on the north and south magnetic poles. We see evidence of emission starting to pile up near the light cylinder, forming the weak caustic seen in Figure 4.8. The conductivity in the magnetosphere is taken to be high and constant everywhere, and we assign a constant emissivity along field lines. The last

open magnetic field lines that originate on the edge of the polar cap traverse the distance between the polar caps and the current sheet both in real space and on the skymap. Some field lines overshoot the current sheet caustic, however, and for example the bridge emission between the 2 γ-ray peaks at $\xi_{\rm obs} = 60^\circ$ comes from both north and south magnetic pole field lines. We speculate that γ-ray emission could be related to dissipation of magnetic energy in the current layer, or more generally, time-dependent accelerating electric fields. There is some dependence of emission properties on the choice of $r_{\rm ov}$ when selecting emitting field lines, but any choice of $r_{\rm ov}$ near 1 will approximately trace the separatrix between open and closed field lines.

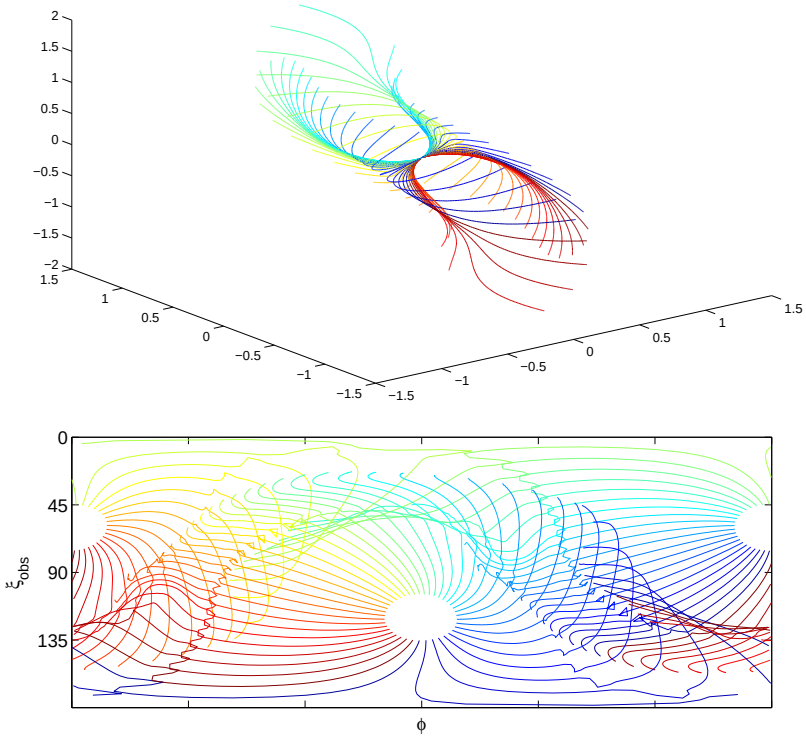

Figure 4.7: Last open field lines in 3 dimensions, and projected onto the skymap. Pulsar inclination angle is 60 degrees. Field lines satisfy $r_{\rm ov} = 0.98$ and are traced to the light cylinder. These field lines traverse the space between polar cap and the current sheet both in real space and on the skymap.

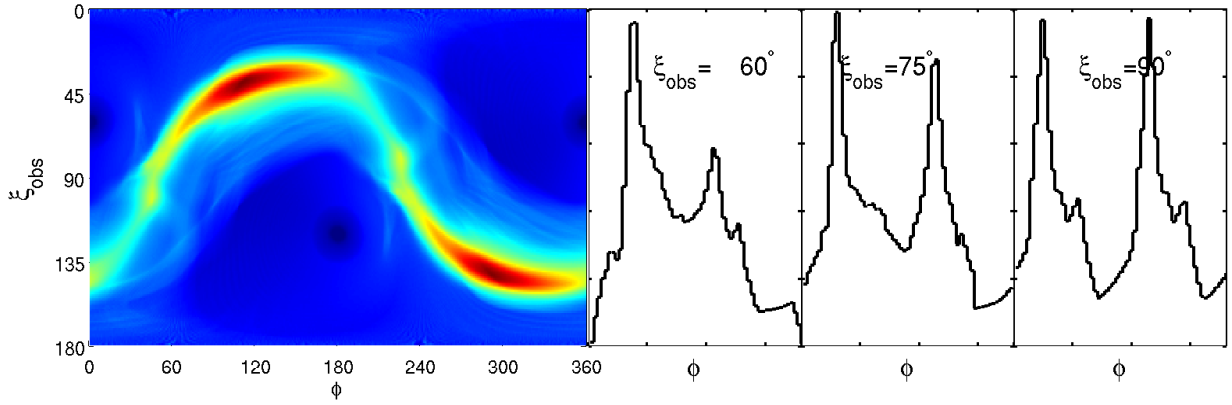

Figure 4.8: Skymap for Separatrix Layer model, where pulsar inclination angle is 60 degrees. Emission is taken from $r_{\rm ov} = 0.98$, interior to the light cylinder. There is a weak caustic on the skymap produced by emission from near the light cylinder, and strong bridge emission between the first and second γ-ray peaks.

7 Combined Current Layer and Current Sheet Skymaps

In this section we propose a more realistic γ-ray emission scenario based on insights gained from our previous models. We envision different physical emission processes generating the bridge emission interior to the light cylinder and the caustic emission exterior to the light cylinder. Indeed, in a number of observed γ-ray pulsars, including Vela (Abdo et al., 2010), phase resolved spectroscopy indicates a harder spectrum for peak emission as compared to bridge emission. They further show spectral differences between the two peaks, and between two different components of bridge emission.

We propose that particles stripped off the stellar surface are accelerated to high Lorentz factors and induce a high multiplicity pair cascade in the high magnetic field environment above the polar cap (see Timokhin & Arons, 2013). Particle motion, currents, and fields dynamically adjust to satisfy the force-free condition in a time-averaged sense. High above the polar cap but still interior to the light cylinder, time-dependent electric fields accelerate particles, and the outward moving particles flying down magnetic field lines give rise to bridge emission. Observed bridge emission from north and south magnetic pole field lines may have different spectral properties due to the asymmetry of the emitting regions. Particles enter the current sheet with a

large bulk motion along field lines and are heated in the sheet by magnetic reconnection, giving rise to the harder double peaked emission. The spectrum of emission from the current sheet could have a spatial dependence. Emission is beamed in the direction of motion of the highly relativistic particles, which is likely to be along the sheet in the direction of the upstream magnetic field. Observed γ-ray pulsars also exhibit a range of relative strengths of bridge versus peak emission, with many showing no bridge emission at all. Differences in relative strength of peak versus bridge emission can naturally arise from different emissivities along open field lines and in the current sheet, and also from current sheet emission coming from different ranges of radii beyond the light cylinder extending into the wind zone. We in fact believe it is necessary to consider emission from beyond the light cylinder in order to produce strongly double peaked light curves.

Figure 4.9 shows the skymap and light curves for the current layer (top), current sheet (middle), and a combination of the current layer and current sheet (bottom), for pulsar inclination angle $\alpha = 30°$. The current layer model takes emission from field lines centered on $r_{\rm ov} = 0.95$ and traced from the star out to $R = 0.8R_{\rm LC}$. The current sheet model takes emission from a broad range of radii, $r = 0.8R_{\rm LC} - 1.8R_{\rm LC}$, with radiation beamed along the magnetic field extrapolated from a short distance away from the sheet. The combined skymap uses approximately equal but arbitrary relative weighting between the current layer and current sheet. This combined model has a strong caustic on the skymap giving rise to the characteristic double peaked light curve profile for certain observer angles, and also significant interpulse bridge emission. The bottom panel gives light curves showing the relative contribution of the current layer interior to $R = 0.8R_{\rm LC}$ (blue), as well as the combined current layer and current sheet light curves (black). The relative weighting of emission from the sheet and layer can be adjusted to give stronger or weaker double peaks.

Figure 4.10 shows the skymap and light curves for the current layer (top), current sheet (middle), and a combination of the current layer and current sheet (bottom), for pulsar inclination angle $\alpha = 60°$. The current layer model takes emission from field lines centered on $r_{\rm ov} = 0.98$ and traced from the star out to $R = 0.8R_{\rm LC}$. The current sheet model takes emission between $r = 0.8R_{\rm LC} - 1.8R_{\rm LC}$, with radiation beamed along the magnetic field extrapolated from

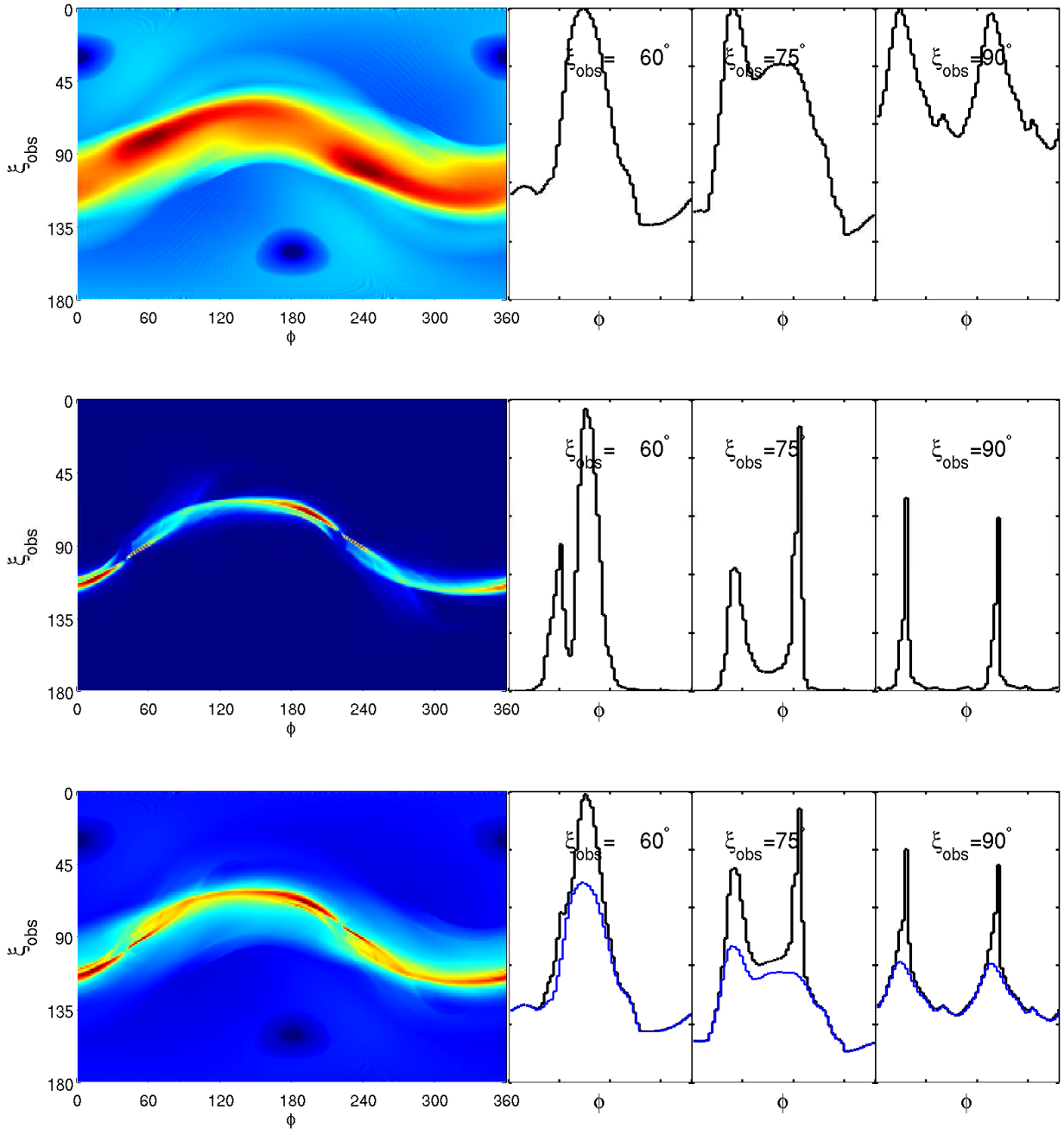

Figure 4.9: Skymaps for current layer (top), current sheet (middle), and both the current layer and current sheet (bottom), for a 30 degree inclined pulsar. The combined model has strong double peaks and bridge emission between the first and second γ-ray peaks. Blue light curves in the bottom panel isolate emission from the current layer, while black curves show total emission from both the current layer and current sheet.

a short distance away from the sheet. The current sheet caustic has some spatial strength dependence, and appears weaker in the locations where both the emission trails the radio pulses and the current layers join. In the combined model we see a strong caustic in the emission skymap giving rise to the characteristic widely separated double peaked light curve profile, and also significant interpulse bridge emission. The relative weighting between the current layer, giving the blue light curve in the bottom panel, and the current sheet, can again be adjusted to give stronger or weaker double peaks in the combined model. The first peak in this model lags possible radio emission originating close to the magnetic poles by ~ 0.19 P for observer angle $\xi_{\rm obs} = 60^\circ$. If radio emission is present near phase $\phi \sim 0^\circ$ at other observer angles, then the γ-ray peak separation increases with decreasing phase offset of the first peak from the radio.

Figure 4.11 shows the skymap and light curves for the current layer (top), current sheet (middle), and a combination of the current layer and current sheet (bottom), for pulsar inclination angle $\alpha = 90^\circ$. The current layer model takes emission from field lines centered on $r_{\rm ov} = 0.98$ and traced from the star out to $R = 0.8R_{\rm LC}$. The current sheet model takes emission between $r = 0.8R_{\rm LC} - 1.8R_{\rm LC}$, with radiation beamed in the direction of the magnetic field extrapolated from a short distance away from the sheet. The current sheet caustic appears as a nearly vertical stripe, reflecting the fact that at intermediate latitudes the current sheet is shaped like an archimidean spiral. For the relative current sheet weighting chosen here, we see a strong caustic in the emission, double peaked light curves, and interpulse bridge emission. Blue curves in the bottom panel again only show emission from the current layer. The phase offset of γ-ray emission from potential radio emission coming from the magnetic poles, ~ 0.16 P, is marginally smaller than the phase lag in the 60 degree inclined pulsar. This effect can be interpreted as due mainly to observing the caustic at a more favorable observer angle.

8 Discussion

In summary, our best working model for high-energy emission from γ-ray pulsars combines emission from the current sheet exterior to the light cylinder and the current layer interior to the

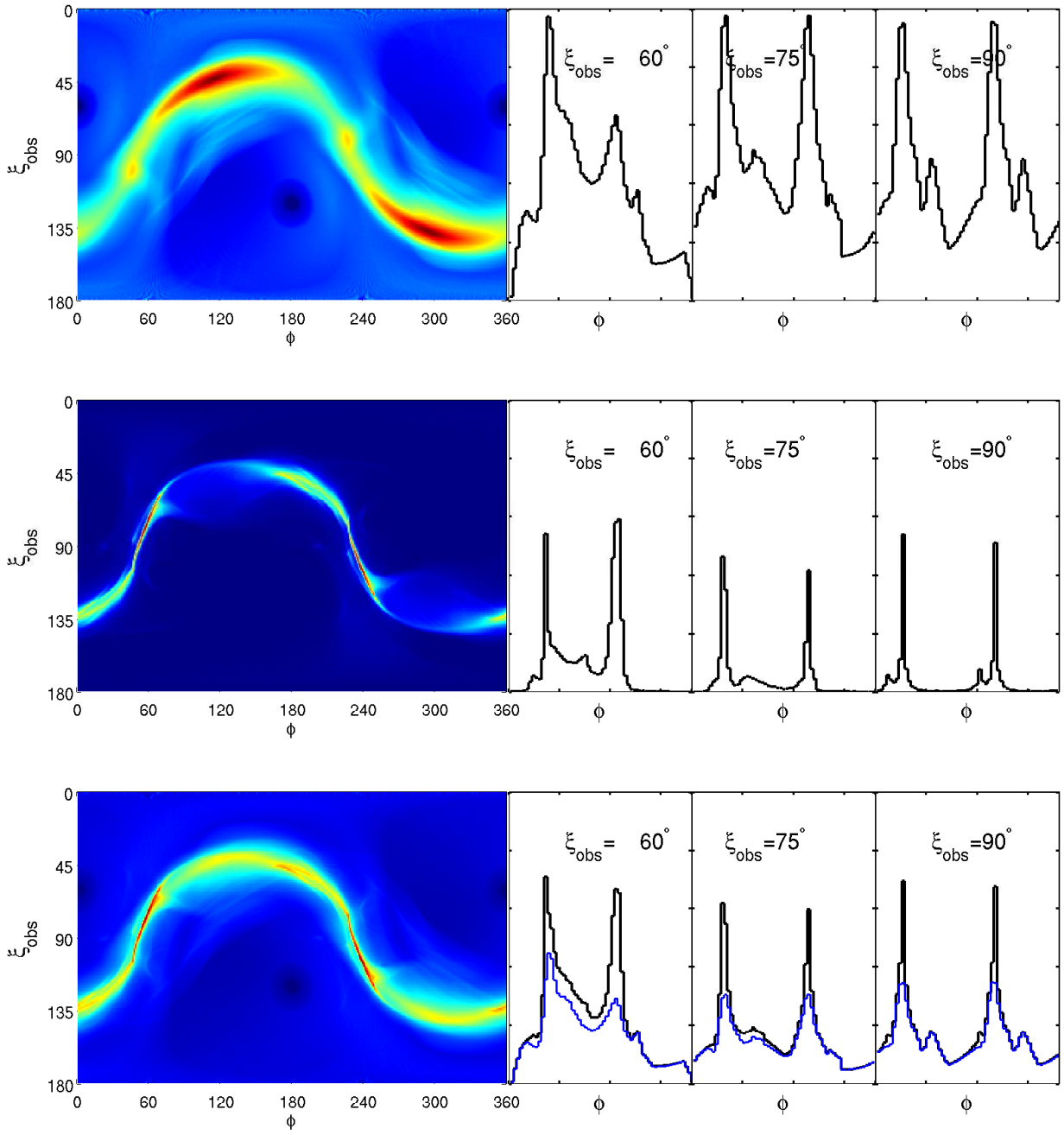

Figure 4.10: Skymaps for current layer (top), current sheet (middle), and both the current layer and current sheet (bottom), for a 60 degree inclined pulsar. The combined model has strong double peaks and bridge emission between the first and second γ-ray peaks. Blue curves in the bottom panel show emission only from the current layer. The light curve at $\xi_{\rm obs} = 60°$ has a phase offset from possible radio emission at the north magnetic pole of ~ 0.19 P.

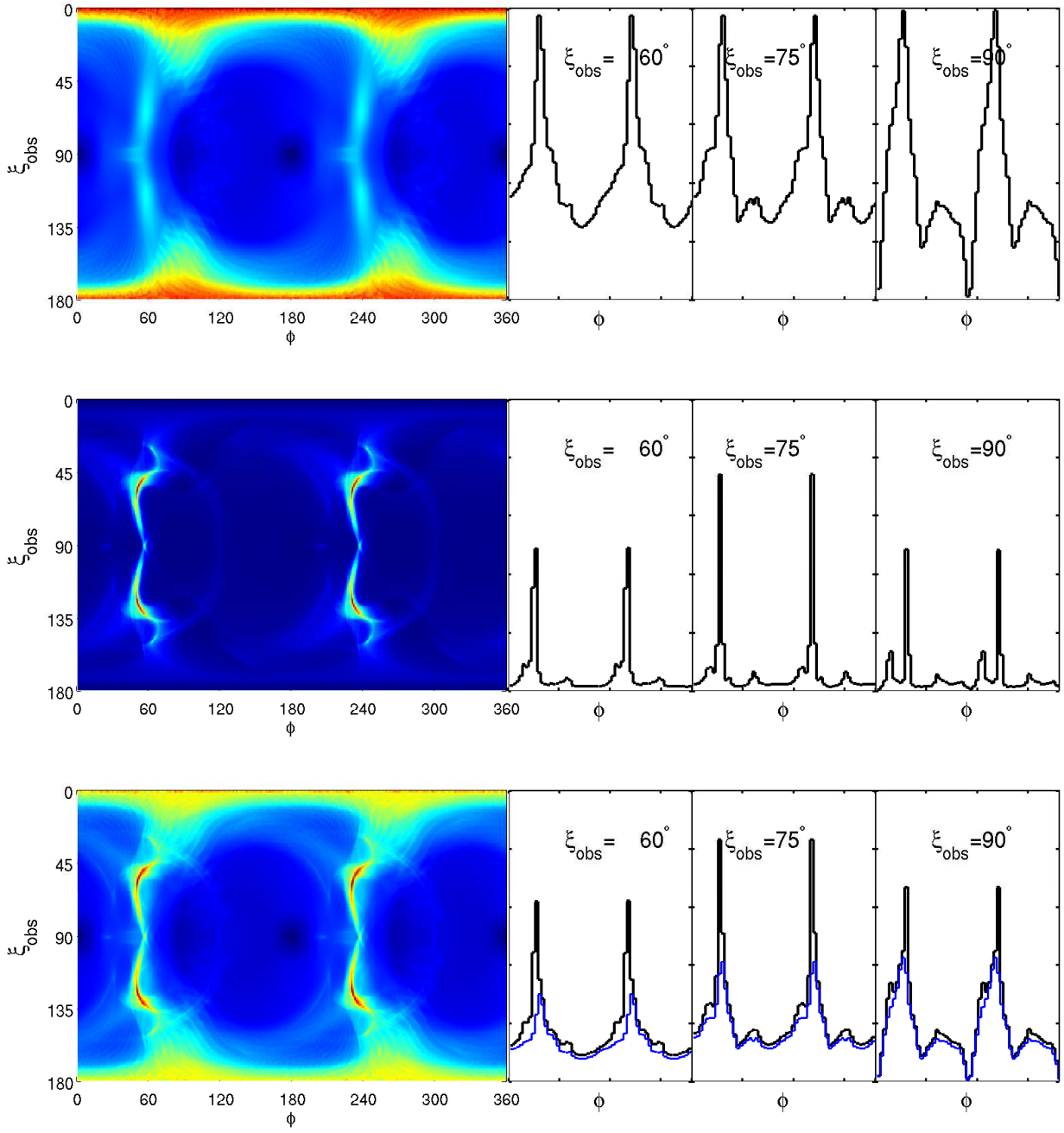

Figure 4.11: Skymaps for current layer (top), current sheet (middle), and both the current layer and current sheet (bottom), for a 90 degree inclined pulsar. There is a strong caustic on the skymap and double peaked light curves for a broad range of inclination angles. Blue light curves in the bottom panel show emission only from the current layer

light cylinder. The current sheet produces strongly double peaked light curves for a broad range of observer angles, and the current layer produces bridge emission between the first and second γ-ray peaks. Synchrotron emission at $\sim$ keV energies in the fluid frame of particles confined to magnetic flux ropes in the sheet may be boosted to GeV energies by bulk relativistic outflow of flux ropes at Lorentz factors of $\gamma \sim 10^6$. Pulsars at higher inclination angle are more likely to give observed double-peaked γ-ray light curves, and the separation between γ-ray peaks decreases with increasing phase offset of the first peak from radio emission at the magnetic poles.

Our results also suggest that there is an inclination angle dependence to the phase lag of the first γ-ray peak from the magnetic poles. If radio emission comes from close to the magnetic poles, then closer radio and γ-ray pulses suggest a higher pulsar inclination angle. It is not clear that radio emission is produced along field lines exactly at the magnetic poles, however. A number of pulsars have radio emission spread out over ~ 0.1 P (Abdo et al., 2010, 2013), suggesting radio emission comes from a range of altitudes above the polar cap. Further, a number of millisecond pulsars with phase-aligned radio and γ-ray pulses have recently been detected by Espinoza et al. (2013). These authors suggest there is some evidence that beamed low altitude radio emission can come from as high as $0.1R_{\rm LC}$ above the polar cap in some pulsars, and accounting for time delay effects would result in radio emission coming ~ 0.015 P earlier than the magnetic pole. Sweepback of magnetic field lines would have the opposite effect, leading to slightly later radio emission.

Recalling equation 4.15 for the phase of observation of radiation, the γ-ray phase offset can also be modified by deviations of particle motions from purely streaming down the upstream magnetic field. It is possible that particle velocities acquire an additional toroidal velocity in the vicinity of the current sheet, driven in this direction by the electromagnetic fields. We know the Poynting flux must carry angular momentum, as the pulsar is spinning down. The strong γ-ray caustic can then be shifted to earlier phases, in accordance with the observed light curves. The bottom two panels of Figure 4.5 suggest practical limits to how strong this effect can be, however, because adding too large an additional velocity component in the toroidal direction may break the strength of the caustic. Deviations from a pure dipolar field structure, the magnetospheric resistivity above the polar caps, and the pulsar spin period, can also potentially affect the shape

of the current sheet and high-energy emission from the outer magnetosphere. We emphasize again that our results indicate that the γ-ray phase offset when considering emission from the dipole current sheet is already significantly smaller than in models that use the split monopole sheet (e.g., Pétri, 2011).

It is thought that non-recycled pulsars tend to have stronger gamma-ray emission compared to total spin-down losses as the pulsar ages (e.g., Vink et al., 2011). This behavior may be related to the plasma supply in the magnetosphere. Young pulsars have abundant plasma in the magnetosphere and likely lack strong accelerator gaps above the stellar polar cap. Synchrotron emission from particles confined within reconnecting magnetic flux ropes may not be sufficiently beamed to give GeV emission. In this picture only older pulsars produce γ-ray emission, and further, not all γ-ray pulsars would necessarily produce radio emission. The lack of observed radio emission does not automatically imply that no radio emission is produced, but it is likely that plasma supply disruptions can in fact shut off radio emission (c.f. Chapter 3).

In this work we have made simplifying assumptions concerning particle velocities, because force-free electrodynamics formally does not solve the particle momentum equations. Our particle velocities are similar to those used in the Separatrix Layer model of Bai & Spitkovsky (2010a), where particles were assumed to fly relativistically down magnetic field lines. We improve upon this model, however, by considering emission explicitly from inside the sheet, rather than the separatrix layer adjacent to it. The next step towards improving pulsar γ-ray emission models would be to include gas dynamics and/or particle velocities in our analysis. Magnetohydrodynamic (MHD) or particle-in-cell (PIC) simulations could potentially provide significant improvements to our models. Results from MHD simulations suggest that potential γ-ray emitting particles in the current sheet travel close to radially outward in the laboratory frame (Tchekhovskoy et al., 2013), though the methods used were ideal. Adding explicit resistivity in MHD may yield further insights on this problem.

The methods for calculating high-energy radiation described in this paper can also potentially be applied to study high magnetization fluids surrounding different types of neutron stars. Specific problems that come to mind include neutron stars in binary compact object systems,

magnetars, and collapsing neutron stars. A common theme among these different objects and systems is that there is differential shearing or winding of strong magnetic fields in the vicinity of the neutron star, leading to the ejection of a powerful Poynting flux wind. As for pulsars and spinning black holes, the Poynting flux removes rotational or orbital energy from the system, but significant details of this dynamical process are not well understood. Large scale current sheets may form in the magnetospheres of these objects, and Poynting flux can be dissipated via magnetic reconnection. This may lead to energetic radiation in a manner closely analogous to how high energy photons are produced in the outer magnetospheres of γ-ray pulsars.

Bibliography

Abdo, A. A., Ackermann, M., Ajello, M., Atwood, W. B., Axelsson, M., Baldini, L., Ballet, J., Barbiellini, G., Baring, M. G., Bastieri, D., & et al. 2010, ApJS, 187, 460

Abdo, A. A., Ajello, M., Allafort, A., Baldini, L., Ballet, J., Barbiellini, G., Baring, M. G., Bastieri, D., Belfiore, A., Bellazzini, R., & et al. 2013, ApJS, 208, 17

Arka, I. & Dubus, G. 2013, A&A, 550, A101

Arons, J. 1983, ApJ, 266, 215

Arons, J. & Scharlemann, E. T. 1979, ApJ, 231, 854

Bai, X.-N. & Spitkovsky, A. 2010a, ApJ, 715, 1282

—. 2010b, ApJ, 715, 1270

Bessho, N. & Bhattacharjee, A. 2005, Physical Review Letters, 95, 245001

—. 2007, Physics of Plasmas, 14, 056503

Bhattacharjee, A., Huang, Y.-M., Yang, H., & Rogers, B. 2009, Physics of Plasmas, 16, 112102

Bogovalov, S. V. 1999, A&A, 349, 1017

Cerutti, B., Uzdensky, D. A., & Begelman, M. C. 2012, ApJ, 746, 148

Cheng, K. S., Ho, C., & Ruderman, M. 1986a, ApJ, 300, 500

—. 1986b, ApJ, 300, 522

Cheng, K. S., Ruderman, M., & Zhang, L. 2000, ApJ, 537, 964

Contopoulos, I., Kazanas, D., & Fendt, C. 1999, ApJ, 511, 351

Coroniti, F. V. 1990, ApJ, 349, 538

Deutsch, A. J. 1955, Annales d'Astrophysique, 18, 1

Dyks, J., Harding, A. K., & Rudak, B. 2004, ApJ, 606, 1125

Dyks, J. & Rudak, B. 2003, ApJ, 598, 1201

Espinoza, C. M., Guillemot, L., Çelik, Ö., Weltevrede, P., Stappers, B. W., Smith, D. A., Kerr, M., Zavlin, V. E., Cognard, I., Eatough, R. P., Freire, P. C. C., Janssen, G. H., Camilo, F., Desvignes, G., Hewitt, J. W., Hou, X., Johnston, S., Keith, M., Kramer, M., Lyne, A., Manchester, R. N., Ransom, S. M., Ray, P. S., Shannon, R., Theureau, G., & Webb, N. 2013, MNRAS, 430, 571

Gruzinov, A. 2005, Physical Review Letters, 94, 021101

—. 2007, ArXiv e-prints

—. 2012, ArXiv e-prints

Hoshino, M. & Lyubarsky, Y. 2012, Space Sci. Rev., 173, 521

Kalapotharakos, C. & Contopoulos, I. 2009, A&A, 496, 495

Kalapotharakos, C., Harding, A. K., & Kazanas, D. 2013, ArXiv e-prints

Kalapotharakos, C., Harding, A. K., Kazanas, D., & Contopoulos, I. 2012a, ApJ, 754, L1

Kalapotharakos, C., Kazanas, D., Harding, A., & Contopoulos, I. 2012b, ApJ, 749, 2

Kirk, J. G. & Skjæraasen, O. 2003, ApJ, 591, 366

Kirk, J. G., Skjæraasen, O., & Gallant, Y. A. 2002, A&A, 388, L29

Koide, S. 2008, Phys. Rev. D, 78, 125026

Komissarov, S. S. 2006, MNRAS, 367, 19

Komissarov, S. S., Barkov, M., & Lyutikov, M. 2007, MNRAS, 374, 415

Lyubarsky, Y. & Kirk, J. G. 2001, ApJ, 547, 437

Lyubarsky, Y. E. 1995, Physics of pulsars

—. 2005, MNRAS, 358, 113

McKinney, J. C. 2006, MNRAS, 368, L30

Michel, F. C. 1994, ApJ, 431, 397

Muslimov, A. G. & Harding, A. K. 2003, ApJ, 588, 430

—. 2004, ApJ, 606, 1143

Palenzuela, C. 2013, MNRAS, 431, 1853

Parfrey, K., Beloborodov, A. M., & Hui, L. 2012, MNRAS, 423, 1416

Pétri, J. 2009, A&A, 503, 13

—. 2011, MNRAS, 412, 1870

—. 2012a, MNRAS, 424, 2023

—. 2012b, MNRAS, 424, 605

—. 2013, MNRAS, 434, 2636

Pétri, J. & Kirk, J. G. 2005, ApJ, 627, L37

Romani, R. W. & Yadigaroglu, I.-A. 1995, ApJ, 438, 314

Rybicki, G. B. & Lightman, A. P. 1979, Radiative Processes in Astrophysics (Wiley)

Spitkovsky, A. 2006, ApJ, 648, L51

Taflove, A. & Hagness, S. 2005, Computational Electrodynamics: The Finite-Difference Time-Domain Method, 3rd edn. (Norwood, MA: Artech House)

Tchekhovskoy, A., Spitkovsky, A., & Li, J. G. 2013, MNRAS, 435, L1

Timokhin, A. N. 2006, MNRAS, 368, 1055

Timokhin, A. N. & Arons, J. 2013, MNRAS, 429, 20

Uzdensky, D. A. & Spitkovsky, A. 2012, ArXiv e-prints

Vink, J., Bamba, A., & Yamazaki, R. 2011, ApJ, 727, 131

Yadigaroglu, I.-A. G. 1997, PhD thesis, STANFORD UNIVERSITY

Zenitani, S., Hesse, M., & Klimas, A. 2009, ApJ, 705, 907

Zenitani, S., Hesse, M., Klimas, A., & Kuznetsova, M. 2011, Physical Review Letters, 106, 195003

Zenitani, S. & Hoshino, M. 2001, ApJ, 562, L63

—. 2005, ApJ, 618, L111

—. 2007, ApJ, 670, 702

—. 2008, ApJ, 677, 530

Chapter 5

Electromagnetic Properties of Binary Neutron Star Magnetospheres

1 Introduction

Binary neutron star and black hole - neutron star mergers have recently gained favor as the likely mechanism for producing short Gamma-ray bursts (GRB's; see e.g., Nakar 2007). The short, < 2 s mean duration of these events points towards very compact source objects, and the radiating plasma must be supplied by at least one object that is composed of ordinary matter, i.e., not a black hole. Merging neutron star systems are also predicted to generate copious gravitational waves, detectable with the next generation of detectors, Advanced LIGO and VIRGO. Linking gravitational wave sources with electromagnetic counterparts (e.g., Kelley et al., 2013) would provide an excellent opportunity for studying physics in strong field gravity and, in some cases, highly magnetized environments.

The bulk of the short GRB prompt emission is presumably due to a complicated and poorly understood dynamical accretion process of neutron star material, but in a sizable fraction of cases (~ 0.1) there can be significant precursor emission ~ 10 s before the prompt emission. The light curve of GRB 081024A from both the Fermi-GST and Swift shows clear evidence of precursor emission just under 2 s before the prompt emission (Troja et al., 2010). Understanding this precursor emission, which may be due to particle acceleration in the magnetosphere (e.g., Hansen & Lyutikov 2001; see also Piro 2012; Lai 2012; Vietri 1996; Lipunov & Panchenko 1996), is a potentially tractable problem with current numerical codes. Palenzuela et al. (2010) made initial forays in this direction by using an MHD code to simulate the magnetospheres of black holes

immersed in a magnetized ideal force-free plasma. A rotating black hole threaded by magnetic field ejects a Poynting flux whose luminosity is sourced by the black hole's rotational energy. Similarly, a black hole hole moving through a magnetic field or binary black holes orbiting in a plasma with net magnetic flux also generate an outward directed Poynting flux powered by the kinetic motions of the black holes. In the latter scenario, the magnetic fields anchored to a circumbinary accretion disk are expected to have strength of order $\sim 10^4$ G near the black holes.

If one of the binary compact objects were instead a neutron star (see Paschalidis et al., 2013), then the magnetic field threading the black hole could in principle be of strength $\sim 10^{12}$ G. This would lead to a much more powerful Poynting flux wind, as the Poynting flux can be thought of as the ejection of wound up toroidal field and hence is proportional to the ambient magnetic field strength. Recent analytic work has suggested that for mass ratios $M_{\rm BH}/M_{\rm NS} \gtrsim 5$ or black hole spin $a \lesssim 0.5$, the system will merge without disrupting the neutron star, ejecting a strong Poynting flux wind (McWilliams & Levin, 2011). A double neutron star system would also be expected to wind up magnetic fields and eject a strong Poynting flux prior to merger.

In this Chapter we modify our resistive force-free code to solve for the electromagnetic field structure surrounding both binary neutron star systems and a single neutron star in orbit around an unmagnetized center of mass. This paper is closely related to work done by Palenzuela et al. (2013b,a), but we find important differences in the electromagnetic energy losses of neutron star binaries. We also allow for stellar spin and arbitrary inclination angles of the magnetic moment one of the neutron stars with respect to the orbital angular velocity. Section 2 briefly describes our code, Section 3 illustrates the magnetospheric structure and explores electromagnetic energy losses, and Section 4 provides a discussion of possible high-energy emission from the outer magnetosphere.

2 Setup

We employ the same three-dimensional numerical code from Chapters 1 and 2 that implements the finite difference time-domain scheme (Taflove & Hagness, 2005) scheme to evolve

electromagnetic fields from Maxwell's equations,

$$\partial_t \mathbf{E} = c\nabla \times \mathbf{B} - 4\pi \mathbf{j},$$
$$\partial_t \mathbf{B} = -c\nabla \times \mathbf{E}, \tag{5.1}$$

where the current $\mathbf{j}$ is given by

$$\mathbf{j} = \rho \mathbf{v} + \sigma \mathbf{E}_{\rm fluid}. \tag{5.2}$$

The fluid velocity $\mathbf{v} = c(\mathbf{E} \times \mathbf{B})/(B^2 + E_0^2)$ is the generalized drift velocity, $\mathbf{E}_{\rm fluid} = \gamma(\mathbf{E} + \mathbf{v} \times \mathbf{B})$ is the fluid frame electric field, $\gamma = (1 - v^2/c^2)^{-1/2}$, E_0 is the magnitude of $\mathbf{E}_{\rm fluid}$, ρ is the charge density, and σ is the plasma conductivity in the fluid frame. We use a high value for the conductivity throughout the magnetosphere, and the results are similar to when using an ideal force-free method (Spitkovsky, 2006). Numerical luminosities calculated in Section 3.4 are within a factor of 2 between the two methods.

Our binary neutron star problem has two conducting spherical stars of mass $1.4M_\odot$ and radius $R_* = 10{\rm km} = 15$ cells. The stars are on Keplerian orbits with angular velocity $\mathbf{\Omega}$ and orbital light cylinder $R_{\rm LC} = c/\Omega$. The embedded dipole field of magnetic moment μ is aligned with the rotation axis for one star, and inclined relative to the rotation axis by angle α for the other. Each star is allowed to spin, but for simplicity the two stars are constrained to have the same spin Ω_* and light cylinder $R_{\rm LC,*} = c/\Omega_*$, with $\mathbf{\Omega}_*$ parallel to $\mathbf{\Omega}$. As the star moves across the grid, we reset the point dipolar magnetic field inside the star. The electric field inside the highly conducting star is set to $\mathbf{E} = -\mathbf{v} \times \mathbf{B}$, where the velocity $\mathbf{v}$ includes motion due to the stellar orbit and spin. Both the $\mathbf{E}$ and $\mathbf{B}$ fields are smoothed at the stellar surface to the exterior solution. The point dipole field also diverges at the center of the star, and so we cut the magnetic field off at a maximum value near the stellar center. This cutoff does not affect the solution exterior to the star. The semimajor axis of the orbits is given by

$$r_{\rm orb} = (R_{\rm LC}/c)^{2/3}(2.8GM_\odot)^{1/3}, \tag{5.3}$$

and we solve for the field structure for a series of different $r_{\rm orb}$ to simulate the binary inspiral. Solutions converge very quickly as long as light signals have time to propagate to the region of interest, but we still generally run our solutions for the longer of one spin period, if the star is spinning, or one orbital period. For the purposes of initialization, the domain is split in half along the surface equidistant from the two stars, and the magnetic fields are set to the fields of a point dipole centered on the star in each half. Instead initializing the field as a superposition of dipoles does not significantly change our results, though there are small changes to the field configuration between the stars. Simulations of a single star in orbit simply remove one of the stars and leave the parameters for the other unchanged. We also solve for the field structure when the stars are moving in vacuum in order to gain further insight into the binary magnetosphere problem.

A simple and robust outer boundary condition for force-free electromagnetic codes is in general an elusive problem. A number of different methods have been proposed, including absorbing boundary conditions, artificial resistive layers and magnetic diffusivities, perfectly matched layers, and complementary operators (Bérenger, 2007; Gedney, 2011; Kalapotharakos & Contopoulos, 2009). In practice we find that for our problem with outgoing wave amplitudes decaying with distance in a weakly resistive medium, a simple periodic boundary condition coupled with a large box size allows us to find converged solutions. Our standard box size has 1024^3 cells, and varying this size has negligible effect on our results. That said, only the highly conducting solutions at the very largest orbital separations in Section 3.4 could theoretically have waves reflect off the outer boundary and propagate back to the inner magnetosphere of interest to us. Vacuum solutions at the very largest orbital separations are run for shorter than one period to prevent such reflections. We also introduce an extra term $(\nabla \cdot \mathbf{B})\mathbf{\Omega} \times \mathbf{r}_{\rm orb}$ into Faraday's equation in the 3 cells above the stellar surface to clean magnetic monopoles left behind as the star moves across our grid through the highly conducting plasma. This prescription does not affect our estimates of electromagnetic luminosity. An alternative method of ensuring $\nabla \cdot \mathbf{B} = 0$ might be to source the dipole field in the star with a current loop, and include also the current due to the time varying electric polarization density induced by a moving magnet (Jackson, 1998).

3 Results

3.1 2D Magnetosphere Illustrations

Figures 5.1-5.10 provide 2D illustrations of magnetospheres of a single star in orbit and binary neutron stars orbiting each other. All figures satisfy the following properties. Magnetic field lines are shown after 1 orbital period in the plane containing $\mathbf{\Omega}$ and intersecting the center of the orbiting star or stars. The orbital light cylinder $R_{\rm LC} = 5.3R_*$ and semimajor axis $r_{\rm orb} = 1.9R_*$. Color is representative of out-of-plane magnetic field. To improve contrast, the color table shows values up to 30% of the maximum, and a square root stretching is applied to the data. The maximum values of out-of-plane magnetic field are given in Table 5.1. The out-of-plane field is weaker in Figures 5.1 and 5.3, and so we mask out a slightly larger star to suppress potential numerical artifacts near the stellar surface that are more apparent in these two cases.

Table 5.1: Maximum out-of-plane magnetic field values, normalized to the field strength at the stellar surface, for Figures 5.1-5.10.

Figure #	setup	α	$R_{\rm LC,*}/R_*$	$B_{\rm out,max}/B_0$
5.1	single star	0°	∞	0.0469
5.2	single star	0°	2.7	0.2022
5.3	binary	0°	∞	0.0651
5.4	binary	0°	2.7	0.2113
5.5	binary	180°	∞	0.2316
5.6	binary	180°	2.7	0.3309
5.7	binary	45°	∞	0.2003
5.8	binary	45°	2.7	0.3865
5.9	binary	90°	∞	0.3264
5.10	binary	90°	2.7	0.4473

Figure 5.1 shows the magnetosphere of a single nonspinning star orbiting in a highly conducting plasma. The field shape resembles that of a point dipole or a neutron star moving in vacuum, but field lines are weakly swept backwards by the orbital motion. Fields are most strongly modified near the star where there are surface currents and conduction currents flowing into the magnetosphere. A weak current sheet also forms in the equatorial plane, and the direction of current in this sheet reverses direction multiple times as distance from the star

increases. This property is due to the star moving in opposite directions at times separated by half a period on the orbit. Figure 5.2 shows magnetic field lines for a rapidly spinning neutron star with $R_{\mathrm{LC},*}/R_* = 2.7$. The spin angular velocity is again aligned with the orbital angular velocity. The field shape now resembles that of a force-free pulsar, but is distorted by the orbital motion.

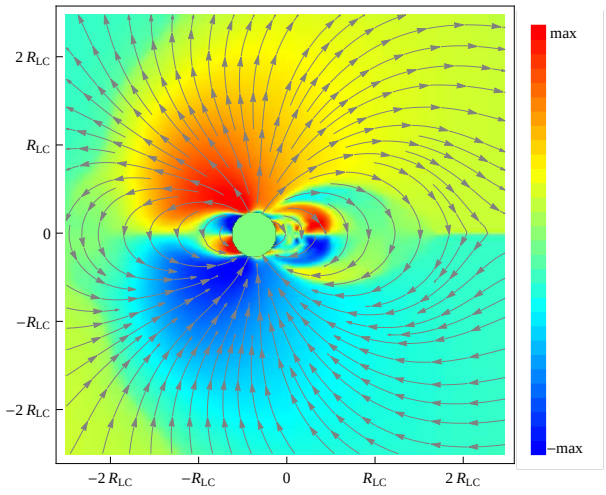

Figure 5.1: Magnetic field lines of a single neutron star on an orbit and μ parallel to $\mathbf{\Omega}$. The light cylinder $R_{\mathrm{LC}} = c/\Omega$, and color represents out-of-plane field. The star is not spinning, i.e., $R_{\mathrm{LC},*} = \infty$. Field lines resemble those of a point dipole, but are weakly swept backwards by orbital motion.

Figure 5.3 shows magnetic field lines for two nonspinning neutron stars in orbit around each other and with both dipole moments aligned with the orbital rotation axis. There is a fundamental change in the shape of the magnetosphere owing principally to the interaction of the magnetospheres of the two stars. In vacuum the binary magnetosphere would to first order be a simple superposition of the fields from each star orbiting individually. When the plasma is highly conducting, however, field lines cannot cross and there is an effective magnetic pressure blocking field lines from one star from propagating to regions closer to the other star. Field lines are instead swept backwards, and the curvature of field lines is readily apparent beyond a distance of $\sim 2R_{\mathrm{LC}}$. There are also two current sheets visible in Figure 5.3. One is an equatorial current sheet through which swept back magnetic field lines reverse direction. The other current sheet extends in the vertical direction and is coincident with the rotation axis, induced by the

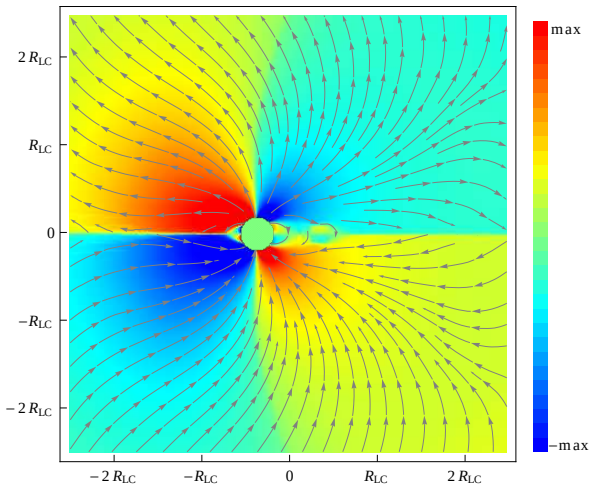

Figure 5.2: Magnetic field lines of a single neutron star on an orbit and μ parallel to $\mathbf{\Omega}$. The light cylinder $R_{\rm LC} = c/\Omega$, and color represents out-of-plane field. The star is spinning rapidly at $\sim$ ms periods, with $R_{\rm LC,*}/R_* = 2.7$. Field lines resemble those of a force-free pulsar.

sweepback of field lines due to orbital motion. When the stars spin rapidly with $R_{\rm LC,*}/R_* = 2.7$, field lines develop stronger sweepback and the equatorial current sheet becomes much more pronounced, as seen in Figure 5.4. Sweepback of fields due to orbital motion again becomes important beyond a distance of $\sim 2R_{\rm LC}$.

Figure 5.5 shows magnetic field lines for two nonspinning neutron stars in orbit around each other and with antialigned magnetic dipoles. In contrast to the aligned binaries, field lines reconnect and easily propagate from one star to the other, resulting in a quadrupolar-like field configuration. The field lines beyond a distance of $\sim 2R_{\rm LC}$ form a type of cocoon, forcing field lines interior to it to develop strong curvature. There is also a weak equatorial current sheet induced by the orbital motion. When the stars spin rapidly with $R_{\rm LC,*}/R_* = 2.7$, magnetospheric currents and the current passing through the equatorial current sheets increase significantly, as illustrated in Figure 5.6. Orbital sweepback of field lines truncates the pulsar-like magnetosphere beyond $\sim 2R_{\rm LC}$, however.

Binary systems where the stars are tilted by intermediate inclination angles are also of physical interest. Figure 5.7 shows magnetic field lines for two nonspinning neutron stars in orbit around each other and with one star's dipole moment tilted by $\alpha = 45°$. The magnetosphere in this case is

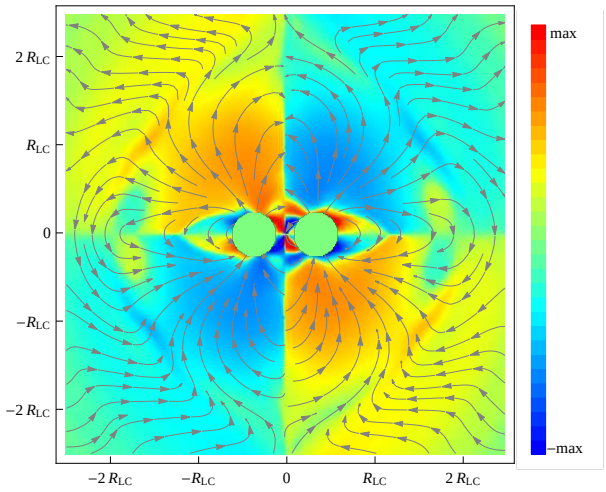

Figure 5.3: Magnetic field lines of orbiting binary neutron stars and μ of both stars parallel to $\mathbf{\Omega}$. The light cylinder $R_{\rm LC} = c/\Omega$, and color represents out-of-plane field. The stars are not spinning, i.e., $R_{{\rm LC},*} = \infty$. Fields from each star feel magnetic pressure of field lines from the other star, forcing magnetic field lines backwards toroidally. Field lines reconnect through a vertical current sheet coincident with the rotation axis.

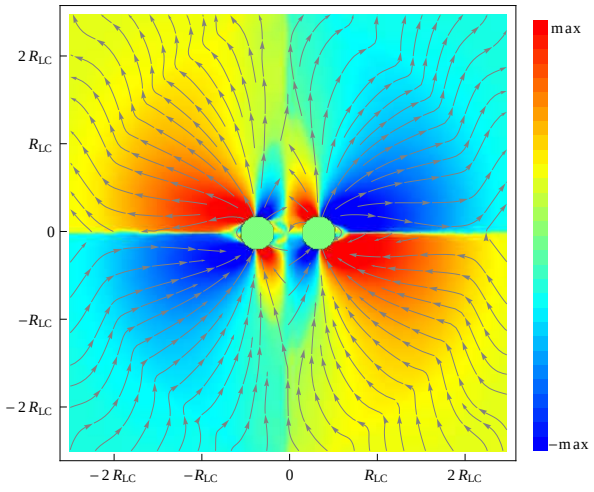

Figure 5.4: Magnetic field lines of orbiting binary neutron stars and μ of both stars parallel to $\mathbf{\Omega}$. The light cylinder $R_{\rm LC} = c/\Omega$, and color represents out-of-plane field. The stars are spinning rapidly at $\sim$ ms periods, with $R_{{\rm LC},*}/R_* = 2.7$. Magnetic fields are pulsar-like interior to $\sim 2R_{\rm LC}$, but feel the orbital effects beyond this distance. Field lines reconnect through a vertical current sheet coincident with the rotation axis.

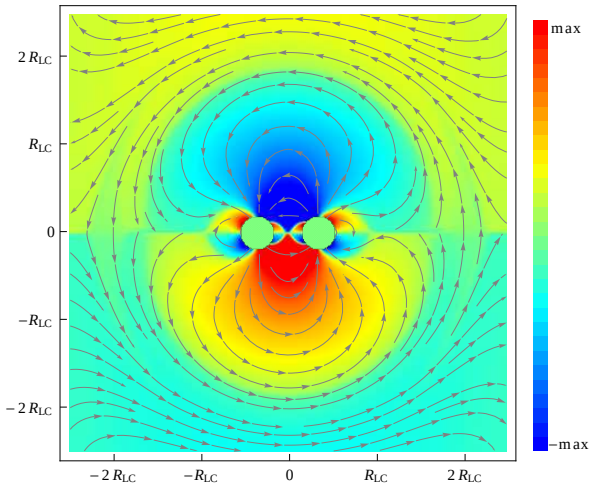

Figure 5.5: Magnetic field lines of orbiting binary neutron stars and μ of left star tilted from $\mathbf{\Omega}$ by angle $\alpha = 180°$. The light cylinder $R_{\rm LC} = c/\Omega$, and color represents out-of-plane field. The stars are not spinning, i.e., $R_{{\rm LC},*} = \infty$. Fields from each star are forced backwards by a confining pressure from field lines attached to the other star.

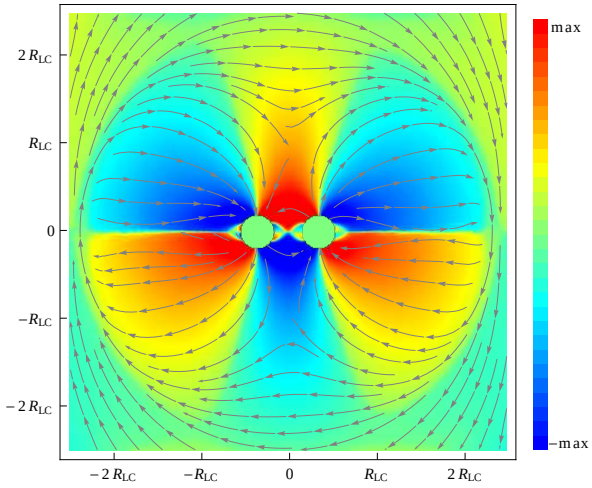

Figure 5.6: Magnetic field lines of orbiting binary neutron stars and μ of left star tilted from $\mathbf{\Omega}$ by angle $\alpha = 180°$. The light cylinder $R_{\rm LC} = c/\Omega$, and color represents out-of-plane field. The stars are spinning rapidly at $\sim$ ms periods, with $R_{{\rm LC},*}/R_* = 2.7$. Magnetic fields are pulsar-like interior to $\sim 2R_{\rm LC}$, but feel the orbital effects beyond this distance.

intrinsically time dependent because of the varying relative orientation of the magnetic moments. A number of field lines connect between the stars, but the majority extend outward. When the stars spin rapidly with $R_{\mathrm{LC},*}/R_* = 2.7$, strong currents sheets form, as illustrated in Figure 5.8. In both cases sweepback of field lines due to orbital motion becomes significant beyond $\sim 2R_{\mathrm{LC}}$.

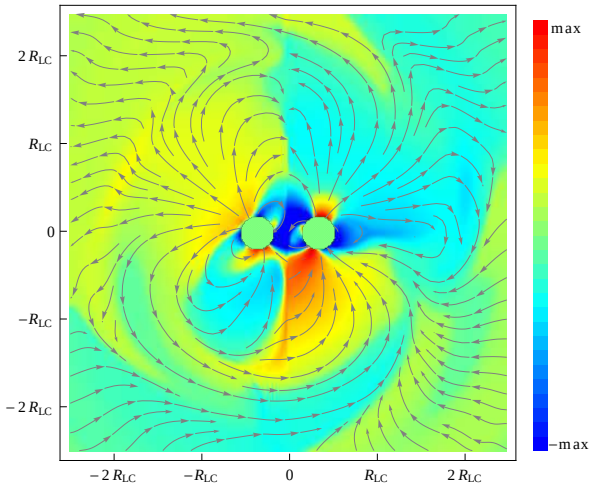

Figure 5.7: Magnetic field lines of orbiting binary neutron stars and μ of left star tilted from $\mathbf{\Omega}$ by angle $\alpha = 45°$. The light cylinder $R_{\mathrm{LC}} = c/\Omega$, and color represents out-of-plane field. The stars are not spinning, i.e., $R_{\mathrm{LC},*} = \infty$. Most field lines open outwards, but a few connect between the stars.

Figure 5.9 shows magnetic field lines for two nonspinning neutron stars in orbit around each other and with one star's dipole moment tilted by $\alpha = 90°$. More field lines connect from one star to the other, as compared to when the tilted neutron star is inclined at a smaller angle, though many field lines still remain open. When the stars spin rapidly with $R_{\mathrm{LC},*}/R_* = 2.7$, the current sheets become much more prominent, as illustrated in Figure 5.10. Field line curvature due to orbital motion in both figures is again significant beyond $\sim 2R_{\mathrm{LC}}$.

3.2 3D Magnetosphere Illustrations

The binary neutron star magnetosphere is an inherently 3D problem, and it is instructive to trace field lines in 3 dimensions. Figure 5.11, the 3D counterpart to Figure 5.3, traces field lines for the case where the neutron star magnetic moments are aligned. The stars are not spinning, have

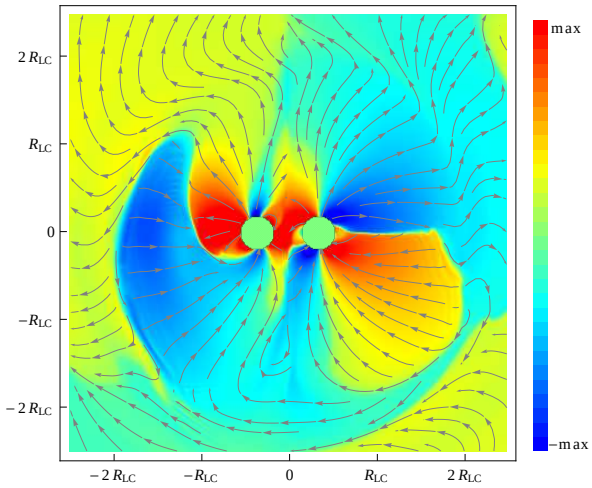

Figure 5.8: Magnetic field lines of orbiting binary neutron stars and μ of left star tilted from $\mathbf{\Omega}$ by angle $\alpha = 45°$. The light cylinder $R_{\rm LC} = c/\Omega$, and color represents out-of-plane field. The stars are spinning rapidly at $\sim$ ms periods, with $R_{\rm LC,*}/R_* = 2.7$. Magnetic fields are determined primarily by stellar spin interior to $\sim 2R_{\rm LC}$.

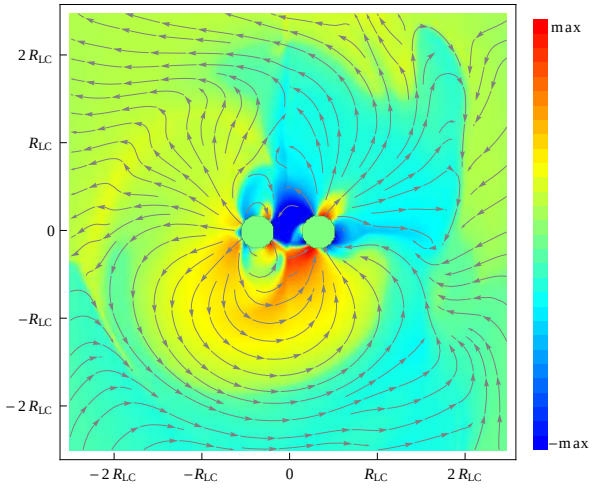

Figure 5.9: Magnetic field lines of orbiting binary neutron stars and μ of left star tilted from $\mathbf{\Omega}$ by angle $\alpha = 90°$. The light cylinder $R_{\rm LC} = c/\Omega$, and color represents out-of-plane field. The stars are not spinning, i.e., $R_{\rm LC,*} = \infty$. Fewer field lines open outwards and more connect between the stars as compared to at lower α.

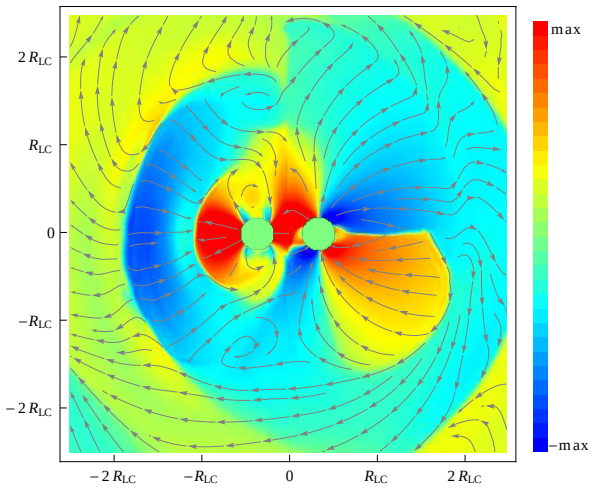

Figure 5.10: Magnetic field lines of orbiting binary neutron stars and μ of left star tilted from $\mathbf{\Omega}$ by angle $\alpha = 90°$. The light cylinder $R_{\rm LC} = c/\Omega$, and color represents out-of-plane field. The stars are spinning rapidly at $\sim$ ms periods, with $R_{\rm LC,*}/R_* = 2.7$. Magnetic fields are dominated by stellar spin interior to $\sim 2R_{\rm LC}$.

orbital light cylinder $R_{\rm LC} = 5.3R_*$, and semimajor axis $r_{\rm orb} = 1.9R_*$. The box is $5R_{\rm LC}$ on a side, and red and green field lines attach to different stars. Field lines are by and large confined to the half of the magnetosphere closer to the star on which they originated, though a few of the trailing field lines do propagate to the other side of the magnetosphere closer to the other star. The equatorial current sheet is demarcated by a light blue surface and has large gaps in the wakes of the two stars. The vertical current sheet extends along the plane consisting of the locus of points equidistant from the two stars. This sheet splits into multiple parts, one of which develops toroidal sweepback due to orbital motion. Figure 5.12, the 3D counterpart to Figure 5.4, shows the field lines in 3D when the aligned neutron stars are spinning rapidly with $R_{\rm LC,*}/R_* = 2.7$. Field lines are now swept backwards by the stellar spin and can propagate to the far side of the magnetosphere closer to the opposing star. The equatorial current sheet has gained in strength and filled in the gaps in the wakes of the stars. The vertical sheet is relatively weaker compared to the equatorial sheet, but still extends along the plane equidistant from the two stars.

Figure 5.13, the 3D counterpart to Figure 5.5, traces field lines in 3D for the case where the neutron star magnetic moments are antialigned. The stars are not spinning, have orbital light

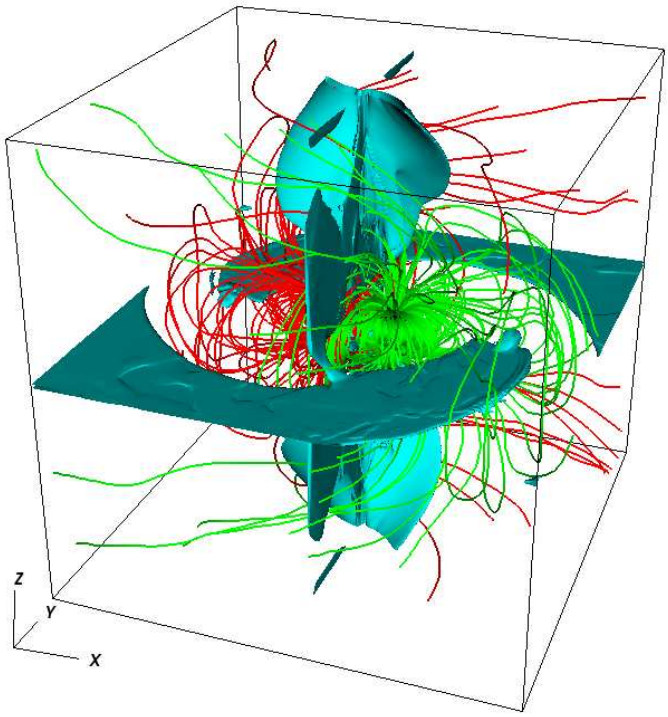

Figure 5.11: Magnetic field lines and current sheets for an orbiting neutron star binary with the magnetic moments of both stars aligned with the rotation axis. The stars are not spinning, i.e., $R_{\mathrm{LC},*} = \infty$. Fields are by and large confined to the half of the magnetosphere closer to their source star. See http://arks.princeton.edu/ark:/88435/dsp01k930bx153 for a movie of this instantaneous field configuration rotating about the axis of orbit.

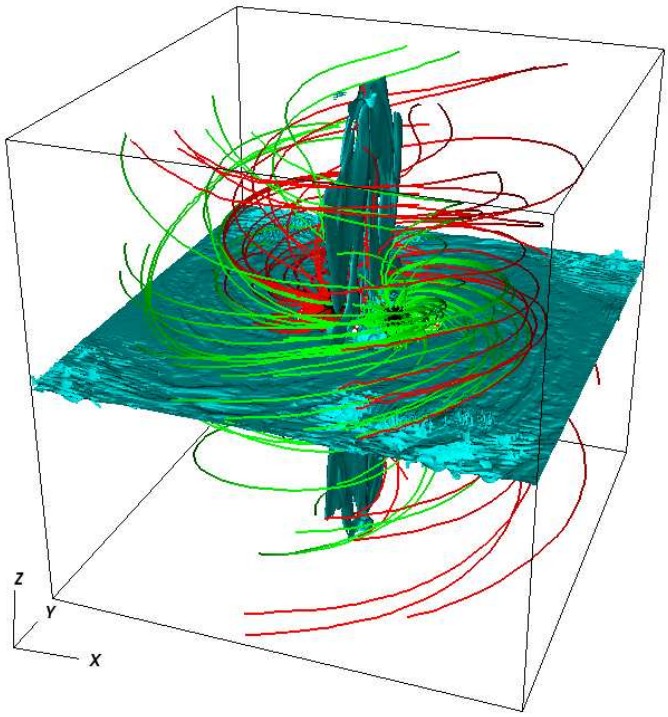

Figure 5.12: Magnetic field lines and current sheets for an orbiting neutron star binary with the magnetic moments of both stars aligned with the rotation axis. The stars are spinning rapidly at $\sim$ ms periods, with $R_{\rm LC,*}/R_* = 2.7$. Stellar spin winds fields backwards toroidally, and they can propagate to the far side of the magnetosphere closer to the opposing star. See http://arks.princeton.edu/ark:/88435/dsp019w032314c for a movie of this instantaneous field configuration rotating about the axis of orbit.

cylinder $R_{\rm LC} = 5.3R_*$, and semimajor axis $r_{\rm orb} = 1.9R_*$. Field lines from one star easily cross to the other side of the magnetosphere closer to the second star, and many of these field lines circle back and reattach to the original star. These field lines form a cocoon with magnetic pressure that forces field lines coming off the second star to wind backwards toroidally. Note that although the field pattern seen here is steady in the frame corotating with the orbital motion, individual field lines are not stationary in this frame. Since the stars are not spinning, both the flux tubes connecting between the stars and the flux tubes encircling the opposing star cannot remain fixed in the corotating frame as the orbit progresses. The flux tube configuration is unstable and fundamentally dynamical, a result previously suggested by a number of authors in the limit of low resistivity and large field line twist (e.g., Lai, 2012; Goldreich & Lynden-Bell, 1969). Indeed, when studying the dynamical behavior of individual field lines, we find a clear cyclical process operating in the magnetosphere. [1] First, field lines from one star can attach to the second star. Second, as the orbit progresses these field lines develop twist and are expelled outward past the second star as closed loops. Third, these loops open up to infinity and then reconnect on the far side of the first star opposite to the second. Fourth, the orbital motion will bring the second star back into contact with the closed loops, and they reattach to the second star.

The illustrated magnetosphere in Figure 5.13 also contains an equatorial current sheet, with gaps carved in the wakes of the two stars. A second sheet extends in the vertical direction and follows roughly the shape of the gap in the equatorial sheet. Figure 5.14, the 3D counterpart to Figure 5.6, illustrates field lines when the stars are spinning rapidly, with $R_{\rm LC,*}/R_* = 2.7$. Field lines now wind back primarily in the toroidal direction rather than in the polar angle direction. There is again a strong equatorial current sheet, and also a hint of a second sheet extending in the vertical direction. It is induced by the orbital motion and follows the shape of the gap in the equatorial current sheet for a short distance. We illustrate also two current-carrying flux tubes connected to the stars and winding toroidally into a helical structure.

[1] See http://arks.princeton.edu/ark:/88435/dsp01xk81jk512 for a movie showing the dynamical behavior of field lines seeded on one of the stars.

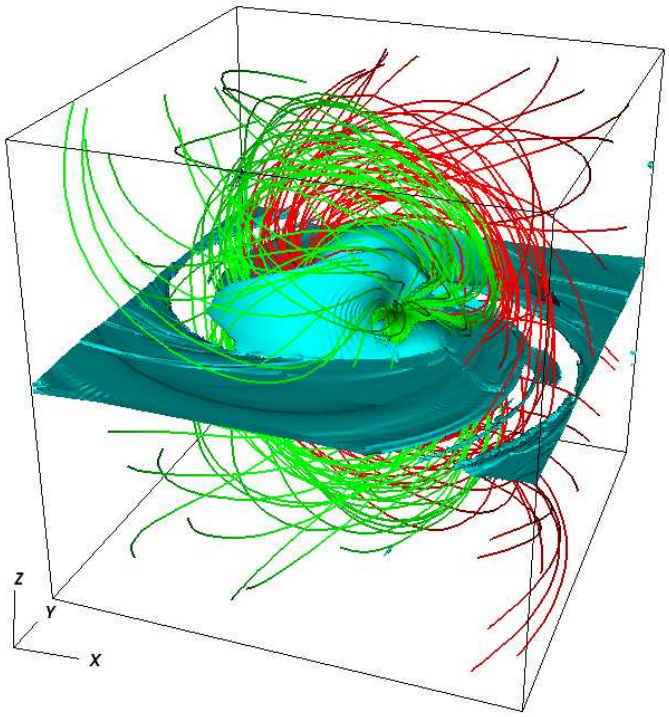

Figure 5.13: Magnetic field lines and current sheets for an orbiting neutron star binary with the magnetic moment of one star aligned with the rotation axis, and the magnetic moment of the other star tilted and antialigned with the rotation axis. The stars are not spinning, i.e., $R_{\mathrm{LC},*} = \infty$. Fields from each star encircle the other star and force fields coming off the second star backwards toroidally. See http://arks.princeton.edu/ark:/88435/dsp01fj2362233 for a movie of this instantaneous field configuration rotating about the axis of orbit.

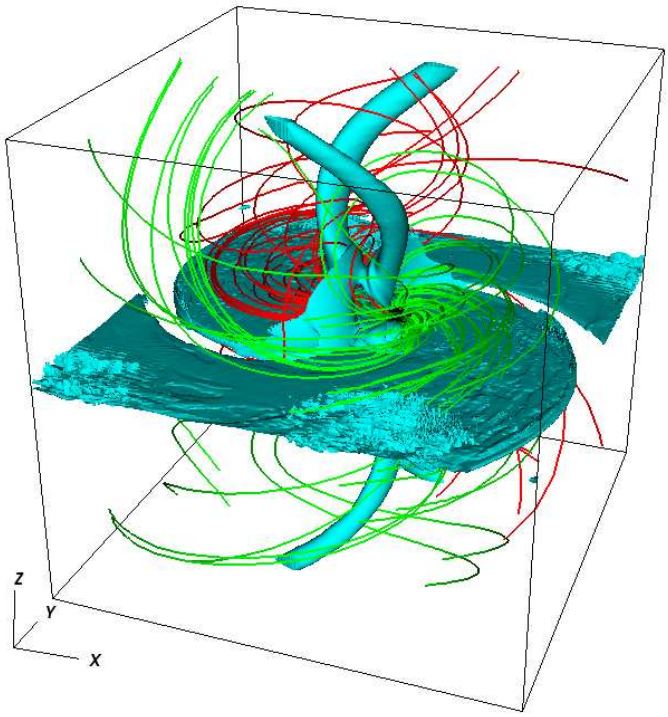

Figure 5.14: Magnetic field lines and current sheets for an orbiting neutron star binary with the magnetic moment of one star aligned with the rotation axis, and the magnetic moment of the other star tilted and antialigned with the rotation axis. The stars are spinning rapidly at $\sim$ ms periods, with $R_{\mathrm{LC},*}/R_* = 2.7$. Stellar spin winds fields backwards toroidally. See http://arks.princeton.edu/ark:/88435/dsp016395w7223 for a movie of this instantaneous field configuration rotating about the axis of orbit.

3.3 Extended Magnetosphere Shape

Having considered the detailed structure of the inner magnetosphere in 2 and 3 dimensions, it is instructive to consider the wind zone of the binary magnetosphere beyond the orbital light cylinder. This section focuses on the 4 canonical cases presented in both Sections 3.1 and 3.2: rapidly spinning and nonspinning, aligned and antialigned dipoles. We plot 2D magnetospheres extending out to $\sim 6R_{\rm LC}$ and at one orbital period, before reflection of waves off the outer boundary can affect the solution. As in Section 3.1, color is representative of out-of-plane field and streamlines trace field lines in the plane containing $\mathbf{\Omega}$ and the stars. The stars have semimajor axis $r_{\rm orb} = 1.9R_*$ and orbital light cylinder $R_{\rm LC} = 5.3R_*$.

Figure 5.15 shows the magnetosphere for nonspinning stars with aligned dipole moments. The features of the inner magnetosphere previously illustrated in Figure 5.3 extend outwards, including both the equatorial and vertical current sheets. Of especial importance is the fact that fields are confined to the half of the magnetosphere closer to the star that they are anchored to. When the orbit has progressed forward by half an orbit, field lines that previously had the freedom to extend outwards in the cylindrical radial direction are now truncated by the magnetic pressure of field lines from the other star. This leads to significant deformation of the field line structure beyond the light cylinder. When the stars are spinning rapidly as in Figure 5.16, the extended magnetosphere illustration of Figure 5.4, a similar deformation truncates the pulsar-like magnetosphere beyond $\sim 2R_{\rm LC}$.

The wind zone of the antialigned dipoles is particularly interesting because field lines can easily propagate to the other side of the magnetosphere closer to the opposing star (c.f. Section 3.2). Figure 5.17 shows the extended magnetosphere counterpart to Figure 5.5. Field lines alternately switch which star they attach to with increasing distance from the stars, forming successive cocoons with confining magnetic pressure. This also causes the direction of currents in the sheets to reverse direction with distance from the stars, giving rise to a type of striped wind pattern. When the stars are spinning rapidly as in Figure 5.18, the extended magnetosphere illustration of Figure 5.6, the fields again switch which star they attach to with increasing

distance from the star. The pulsar-like fields are truncated beyond $\sim 2R_{\rm LC}$, with successive cocoons with magnetic pressure sourced from different stars, and reversing current sheets.

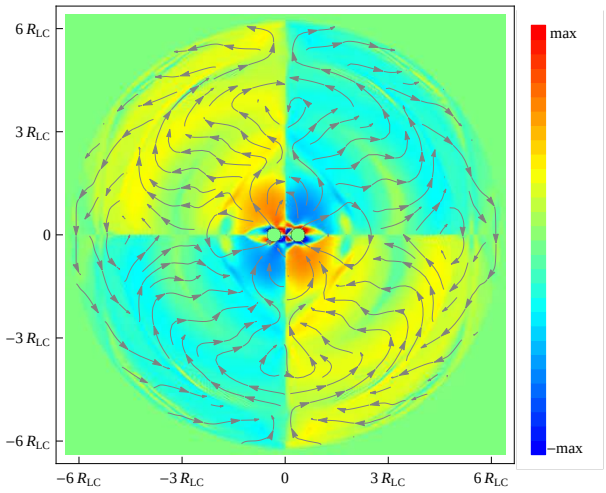

Figure 5.15: Extended wind-zone magnetosphere of orbiting binary neutron stars and μ of both stars parallel to $\mathbf{\Omega}$. Color represents out-of-plane field, and the stars are not spinning, i.e., $R_{\rm LC,*} = \infty$. Vertical and equatorial current sheets extend outwards, and field lines beyond the light cylinder $R_{\rm LC} = c/\Omega$ feel significant pressure from field lines attached to the other star as the orbit progresses.

3.4 Electromagnetic Luminosity

Analytic Guidance

In much the same way that a pulsar ejects a Poynting flux wind and spins down, orbiting magnetized neutron stars should eject a Poynting flux wind tapping the orbital energy. Before calculating electromagnetic luminosities numerically, we present several arguments for how we expect luminosity to scale with the orbital angular velocity. We touch also upon the dependence of luminosity on the relative inclination angle of the magnetic moments of the stars.

First consider point dipoles moving in vacuum, where the radiation fields can be calculated exactly (Heras, 1994; Ioka & Taniguchi, 2000; Medvedev & Loeb, 2013). A magnetic dipole

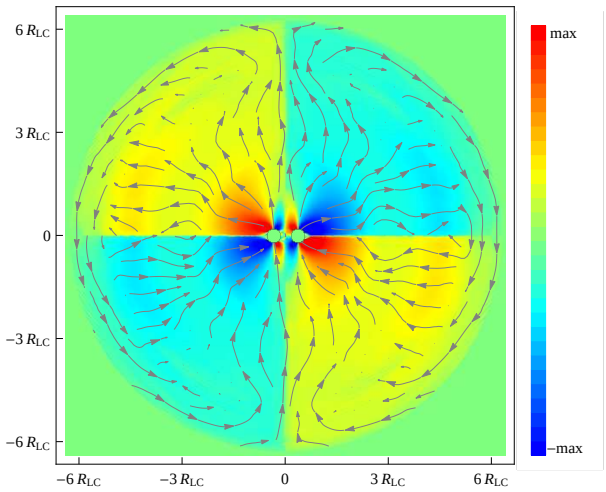

Figure 5.16: Extended wind-zone magnetosphere of orbiting binary neutron stars and μ of both stars parallel to $\mathbf{\Omega}$. Color represents out-of-plane field, and the stars are spinning rapidly at $\sim$ ms periods, with $R_{\mathrm{LC},*}/R_* = 2.7$. The pulsar-like magnetic fields are truncated at $\sim 2R_{\mathrm{LC}} = 2c/\Omega$, and significantly deformed by magnetic from the opposing star beyond this distance as the stars orbit. Equatorial and vertical current sheets extend outwards.

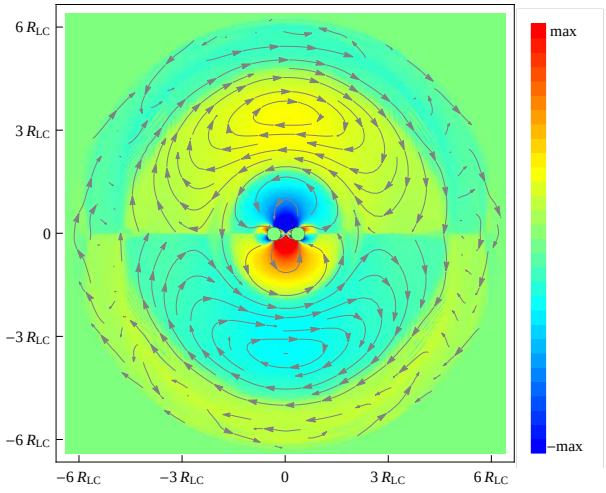

Figure 5.17: Extended wind-zone magnetosphere of orbiting binary neutron stars and μ of left star tilted from $\mathbf{\Omega}$ by angle $\alpha = 180°$. Color represents out-of-plane field, and the stars are not spinning, i.e., $R_{\mathrm{LC},*} = \infty$. Field lines switch which star they attach to with increasing distance from the stars, and current sheets reverse direction, both occurring on a distance scale of the light cylinder $R_{\mathrm{LC}} = c/\Omega$.

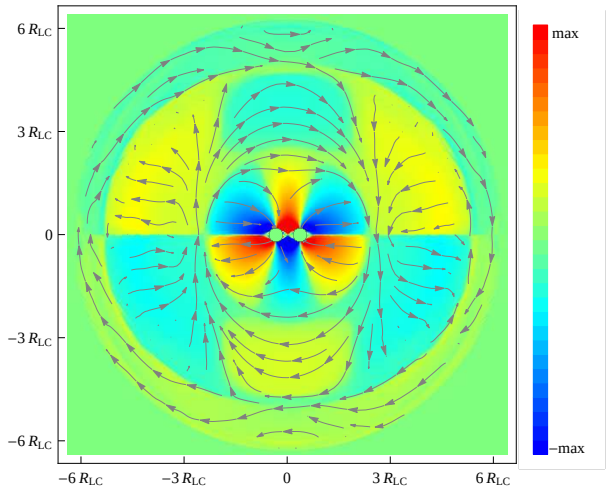

Figure 5.18: Extended wind-zone magnetosphere of orbiting binary neutron stars and μ of left star tilted from $\mathbf{\Omega}$ by angle $\alpha = 180°$. Color represents out-of-plane field, and the stars are spinning rapidly at $\sim$ ms periods, with $R_{\mathrm{LC},*}/R_* = 2.7$. Pulsar-like magnetic fields are truncated at $\sim 2R_{\mathrm{LC}} = 2c/\Omega$, with successive sequences of fields switching which star they attach to and reversing current sheets, as distance from the stars increases.

moving with nonrelativistic velocity $\mathbf{v}$ will induce an electric dipole

$$\mathbf{p} = \mathbf{v}/c \times \mu. \tag{5.4}$$

Hence, there will be electric dipole radiation with

$$L \propto \ddot{\mathbf{p}}^2 \propto v^2\Omega^4 \propto \Omega^{14/3}, \tag{5.5}$$

where we have assumed Keplerian orbital motion. Note that electric dipole radiation cancels for aligned magnetic dipoles since the stars are moving in opposite directions, but adds constructively for antialigned dipoles. Next, there will be no magnetic dipole radiation, as the multipolar field expansion about the center of mass will contain a static dipole plus a time-varying quadrupole. Magnetic quadrupole radiation will scale as

$$L \propto \left(\dddot{r\mu}\right)^2 \propto r^2\Omega^6 \propto \Omega^{14/3}, \tag{5.6}$$

and is again stronger for antialigned dipoles. The magnetic quadrupole radiation component also turns out to have a similar strength to the electric dipole radiation component (Ioka & Taniguchi, 2000), but the main takeaway point is that the overall scaling of luminosity with orbital angular velocity in vacuum will be

$$L \propto \Omega^{14/3}. \tag{5.7}$$

A second argument based on the energy dissipation rate in the magnetospheric current circuits has been presented by a number of authors (see e.g., Lyutikov, 2011; Lai, 2012; Hansen & Lyutikov, 2001; Drell et al., 1965). This argument applies to binary stars on Keplerian orbits in vacuum. The potential drop across the surface of one of the stars is of order

$$\Phi \approx (\Omega r_{\rm orb}/c) B R_*, \tag{5.8}$$

where $B \approx B_0 (R_*/r_{\rm orb})^3$ and B_0 is the surface field strength at the companion star. Assuming a vacuum resistance of free space, the luminosity then scales as

$$L \propto \Phi^2 \propto \Omega^{14/3}. \tag{5.9}$$

It is also possible to extract a similar scaling by considering the Poynting flux crossing the orbital light cylinder. The electric field in a displacement current dominated vacuum magnetosphere is roughly

$$\mathbf{E} \approx -(\mathbf{\Omega} \times \mathbf{r})/c \times \mathbf{B}. \tag{5.10}$$

If we approximate the semimajor axis of the orbit as small, then we can consider the scaling of field quantities with radial distance from the center of the orbit. The poloidal magnetic field falls as $B_p \propto 1/r^3$, the toroidal field $B_\phi \approx B_p$ at $r = R_{\rm LC}$, and the poloidal electric field $E_p \approx B_p$ at $r = R_{\rm LC}$. Hence the luminosity calculated at the light cylinder scales as

$$L \propto \int \mathbf{E} \times \mathbf{B}\, d\mathbf{A} \propto \Omega^4, \tag{5.11}$$

with corrections due to deviations of the electric field from corotation and the displacement of the neutron star from the center of the orbit.

When the stars are moving in a highly conducting plasma, our previous argument for the scaling of luminosity based on Poynting flux crossing the light cylinder is even more accurate. The electric field is exactly the corotation field

$$\mathbf{E} = -(\mathbf{\Omega} \times \mathbf{r})/c \times \mathbf{B}, \tag{5.12}$$

and E_p and B_ϕ again have strength $1/R_{\rm LC}^3$ at the light cylinder, giving luminosity integrated at the light cylinder $L \propto \Omega^4$. This story changes when the stars are allowed to spin, however. If the stars are spinning rapidly, with spin light cylinder $R_{\rm LC,*}$ interior to the orbital light cylinder, then E_p and B_ϕ will reach parity with B_p at $r = R_{\rm LC,*} < R_{\rm LC}$. They will have strength

$$E_p \approx B_\phi \approx 1/R_{\rm LC,*}^3 \tag{5.13}$$

at $r = R_{\rm LC,*}$, but fall as $1/r$ for $R_{\rm LC,*} < r < R_{\rm LC}$. We can parameterize the strength of E_p and B_ϕ at $r = R_{\rm LC}$ as

$$E_p \approx B_\phi \approx 1/R_{\rm LC}^{1+\zeta}, \tag{5.14}$$

where $\zeta \to 2$ when $R_{\rm LC,*} \to \infty$ and $\zeta \to 0$ when $R_{\rm LC,*} \to 0$. The Poynting flux integrated at the orbital light cylinder then gives

$$L \propto \Omega^{2\zeta}. \tag{5.15}$$

This luminosity scales as $L \propto \Omega^4$ for nonspinning stars, and scales very weakly with Ω for rapidly spinning stars.

Numerical Calculations

We calculate luminosities in our numerical solutions by integrating Poynting flux over a spherical surface centered on the center of mass and including the stars. For spinning stars this surface is

separated from the stellar surface at distance of closest approach by 5 cells, and for nonspinning stars this surface is in the asymptotic region beyond the orbital light cylinder. This method does not account for Poynting flux dissipated in the region between the stars, but such dissipation represents a higher order correction to the electromagnetic energy losses. Luminosity is generally calculated after 1 orbital period, unless the spin period is longer and finite, in which case we compute luminosity after 1 spin period. Luminosity has been normalized to $L_0 = \mu^2\Omega_*^4/c^3$, where $\Omega_* = (3/8)c/R_*$, in all the following figures.

We first calculate the luminosity of neutron stars moving in vacuum to compare to analytic expectations. Figure 5.19 gives numerically calculated luminosities as a function of orbital separation for nonspinning neutron stars moving in vacuum. We show luminosity for a single neutron star in orbit with magnetic moment aligned with the orbital angular velocity, as well as aligned and antialigned binaries. The luminosity of the single neutron star scales as Ω^5, very close to the theoretically expected result. The aligned binaries appear to have a slightly stronger scaling, and a higher luminosity than a single star below $r_{\rm orb}/R_* = 4$. The analytic vacuum theory suggests that the radiation fields of aligned point dipoles should cancel to first order because the dipoles are moving in opposite directions at any instant in time (Ioka & Taniguchi, 2000). The fact that we do not obtain this result below $r_{\rm orb}/R_* = 4$ may be due to corrections from the large apparent size of our stars near close contact, a physical effect in real neutron star mergers. Indeed, the aligned binaries luminosity appears to drop below that of a single star above $r_{\rm orb}/R_* = 4$, where the finite star is relatively less important. The antialigned dipoles have higher luminosity than the aligned dipoles because the radiation fields of the oppositely moving dipoles do not cancel, but rather constructively interfere. We explore the dependence of luminosity on the inclination of the tilted star in more detail in Section 3.5.

We now turn to neutron stars moving in a highly conducting plasma. Figure 5.20 shows the radiated Poynting luminosity for nonspinning neutron stars orbiting in a highly conducting plasma. The luminosity of the single neutron star has increased marginally compared to vacuum, but still scales very close to $\Omega^{14/3}$. The similarity to vacuum tells us that displacement currents dominate over conduction currents, and indeed the field lines shown in Figure 5.3 are closed and

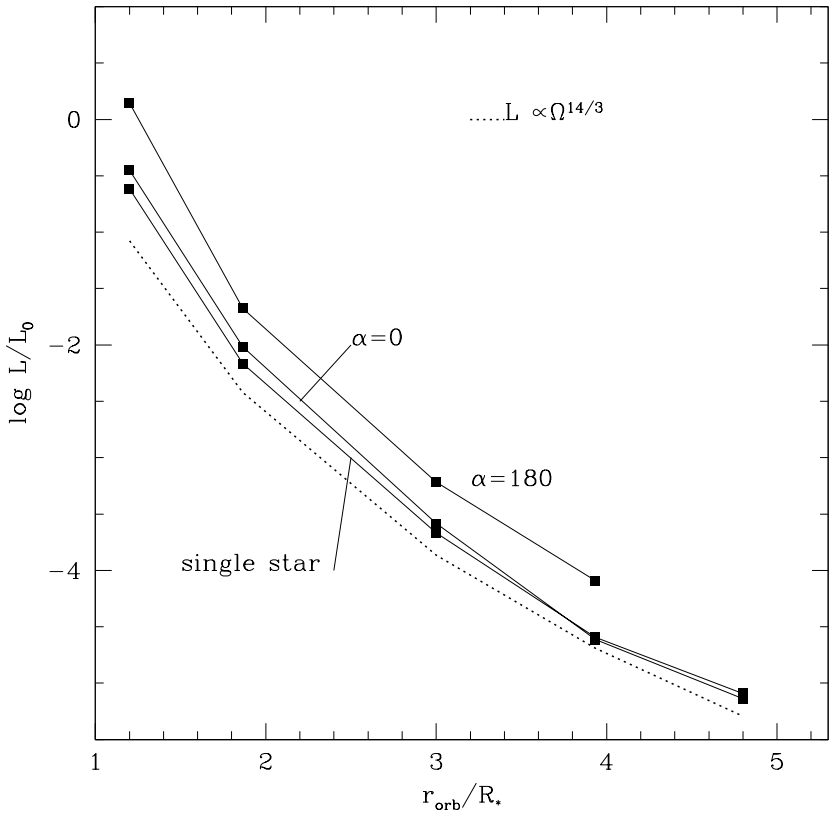

Figure 5.19: Electromagnetic luminosity as a function of the semimajor axis of the neutron star orbits. The neutron stars are moving in vacuum and are not spinning, i.e., $R_{\mathrm{LC},*} = \infty$. Curves are shown for a single star in orbit, an aligned binary, and an antialigned binary. The scaling of L with Ω is close to theoretically expected results.

resemble to first order a point dipole. Note also that the luminosity approaches L_0 at $r_{\rm orb}/R_* = 1.2$, where $R_{\rm LC}/R_* = 2.7$, confirming that the magnitude of the luminosity due to orbital motion is similar to that of a pulsar spinning with the same angular velocity. As described in Sections 3.1, 3.2, and 3.3, an aligned binary force-free magnetosphere is fundamentally different from that of a single star due to the influence of magnetic pressure from each star on the other. Field lines are forced backwards toroidally, and the luminosity is significantly higher than that of a single star. The luminosity of the antialigned binary is higher still because field lines from one star encircling the second force greater sweepback of field lines coming off the second star. Both aligned and antialigned binaries have luminosity scaling as $L \propto \Omega^4$, in rough accordance with our expectations. Our previous analytic arguments are applicable to this system, with the caveat that the strength of E_p and B_ϕ should be considered at several light cylinder radii, rather than at the light cylinder proper. Note also that in the antialigned binary dynamical conduction currents can freely flow between the stars and exert a braking torque on both stars.

The open triangles in Figure 5.20 represent electromagnetic luminosities when the aligned binaries do not have fixed semimajor axis, but instead inspiral due to the radiation of gravitational waves. The orbital angular velocity increases as (Medvedev & Loeb, 2013)

$$\Omega(t) = \Omega_i (1 - t/t_s)^{-3/8}, \tag{5.16}$$

where Ω_i is the initial orbital frequency, the source time is

$$t_s = \frac{5}{64} \left(\frac{\Omega_i}{\Omega_g} \right)^{-8/3} \Omega_g^{-1}, \tag{5.17}$$

and

$$\Omega_g = \frac{c^3}{2.8 G M_\odot}. \tag{5.18}$$

The Poynting flux in this case has a very strong radial dependence, and so it is important to measure luminosities close to the stars to capture the true electromagnetic energy losses. We measure Poynting fluxes just inside the shrinking orbital light cylinder, but there is still a

systematic downward bias to the luminosity because the Poynting flux takes time to propagate out to the light cylinder. Overall, the luminosity of the inspiralling binary is in excellent agreement with luminosities in our steady corotating solutions with fixed semimajor axis, however.

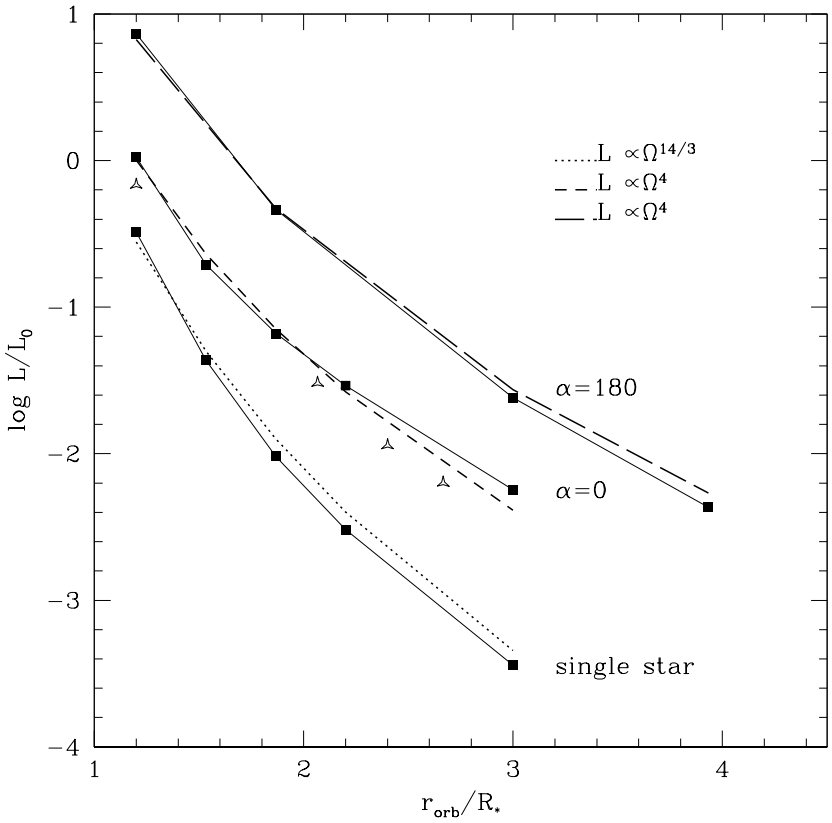

Figure 5.20: Electromagnetic luminosity as a function of the semimajor axis of the neutron star orbits. The neutron stars are moving in a highly conducting plasma and are not spinning, i.e., $R_{\rm LC,*} = \infty$. Curves are shown for a single star in orbit, an aligned binary, and an antialigned binary. Open triangles represent the luminosity of an aligned binary on a dynamically shrinking orbit. Scaling of luminosity with Ω is close to theoretical expectations, but the magnitude of luminosity is much higher in binaries due to interacting pressure of field lines.

Thus far we have considered nonspinning neutron stars orbiting in vacuum and nearly ideal plasma. Neutron star spins can significantly affect the radiated electromagnetic luminosity. Figure 5.21 shows the luminosity of a single neutron star in orbit in a highly conducting plasma for different values of stellar spin. The nonspinning star has luminosity tending to zero at large orbital separations and scaling as $L \propto \Omega^4$. When spinning rapidly, with $R_{\rm LC,*}/R_* = 5.3$, the

luminosity instead asymptotes to the pulsar spin down at large orbital separations. The orbital component of luminosity becomes significant when $r_{\rm orb}/R_*$ drops below $R_{\rm LC,*}/R_*$. At even faster spin, with $R_{\rm LC,*}/R_* = 2.7$, the luminosity asymptotes to $L \approx L_0$ at large orbital separations.[2] The orbital contribution to the electromagnetic luminosity again becomes important when $r_{\rm orb}$ drops below $R_{\rm LC,*}$. Note that the scaling of luminosity with Ω clearly flattens as the stars spin more rapidly. Beyond arguments already presented in the previous subsection, we attribute this to field lines already being swept backward by stellar spin, and hence orbital motion being less effective at sweeping back field lines and radiating electromagnetic energy.

We now consider the binary neutron star problem where the stars are spinning rapidly. Figure 5.22 shows the luminosity of a single neutron star, and aligned and antialigned binaries, all rapidly spinning with $R_{\rm LC,*}/R_* = 2.7$. The single neutron star has luminosity scaling roughly as $\Omega^{3/2}$ for $r_{\rm orb}/R_*$ below $R_{\rm LC,*}/R_*$. The aligned binaries have a very similar scaling in this regime, and are close to twice as luminous as a single star. The antialigned binaries have larger luminosity than the aligned binaries for $r_{\rm orb}/R_* \gtrsim 1.4$, but lower luminosity at very close contact. Evidently, for rapidly spinning stars, the dipolar fields of each star tend to cancel at very close contact and leave weaker radiation fields.

We conclude this section by providing a rough fitting formula for the luminosity of aligned binary neutron stars orbiting with orbital angular velocity Ω and spinning with angular velocity Ω_*. We obtain

$$L = 2\frac{\mu^2\Omega_*^4}{c^3} + \frac{\mu^2}{c^3}\left(1 + 6.5(\Omega_*/\Omega_0)^{1.7}\right)\Omega_0^{2.5\Omega_*/\Omega_0}\Omega^{4-2.5\Omega_*/\Omega_0}, \tag{5.19}$$

where $\Omega_0 = 3/8(c/R_*)$ corresponds to rapid rotation at $\sim$ ms periods. This formula applies during the last few milliseconds before merger of binary neutron stars inspiralling due to gravitational waves (see e.g., Medvedev & Loeb, 2013). It reduces to the pulsar luminosity when $\Omega \to 0$, scales as Ω^4 for nonspinning stars, and scales as $\Omega^{1.5}$ for rapidly spinning stars with $\sim$ ms

[2]The fact that the luminosity drops below L_0 is due to the numerical dissipation in the volume interior to the surface where we measure Poynting flux, and also to the fact that this surface is not a sphere centered on the neutron star itself. If we measure the pulsar's Poynting flux in the same way, on a sphere with center displaced from the star, then the luminosity of a single spinning star at $r_{\rm orb}/R_* = 4$ is 5% higher than the pulsar luminosity.

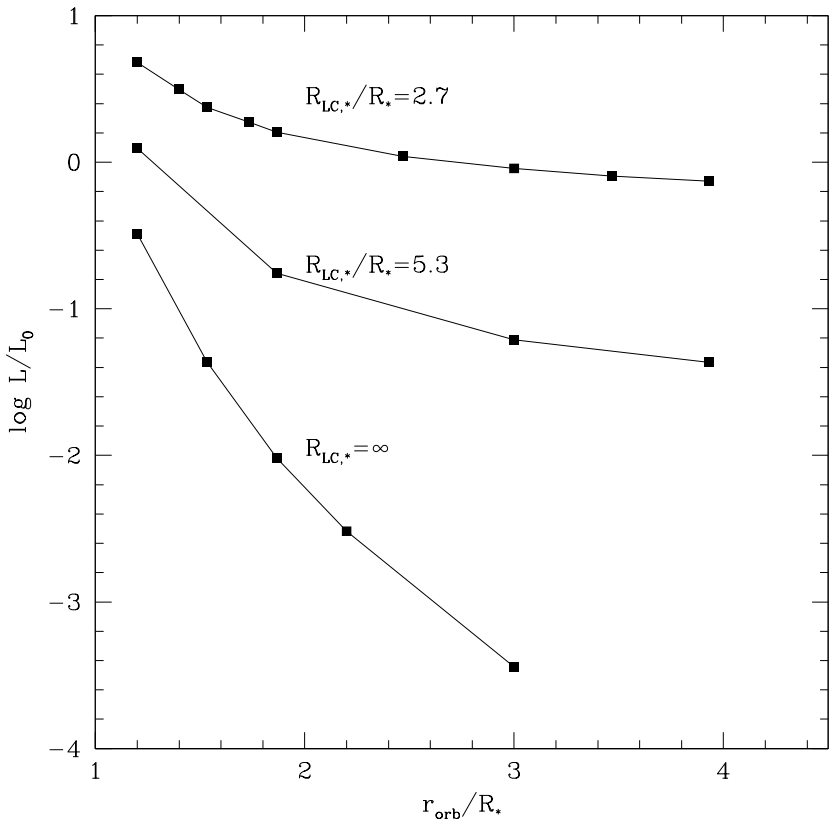

Figure 5.21: Electromagnetic luminosity as a function of the semimajor axis of a single neutron star orbiting a center of mass in a highly conducting plasma. Curves are shown for different stellar spins, with $R_{\rm LC,*}/R_* = 2.7, 5.3, \infty$. The scaling of luminosity with Ω becomes shallower as the stars spin more rapidly.

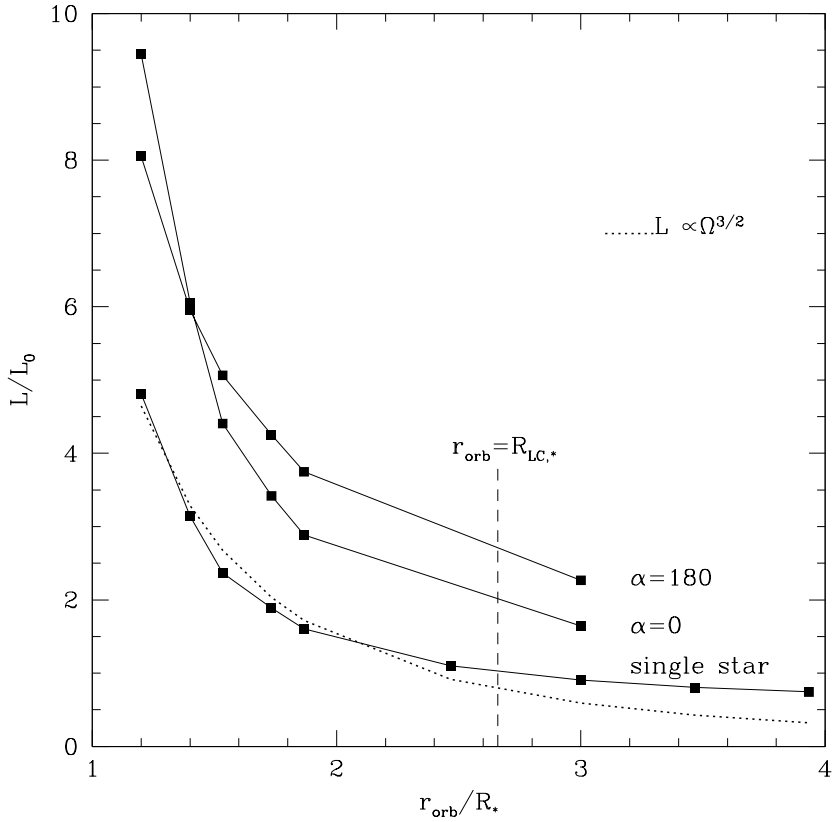

Figure 5.22: Electromagnetic luminosity as a function of the semimajor axis of the neutron star orbits. The neutron stars are moving in a highly conducting plasma and are spinning rapidly at $\sim$ ms periods, with $R_{\rm LC,*}/R_* = 2.7$. Curves are shown for a single star in orbit, an aligned binary, and an antialigned binary. Scaling of luminosity with Ω is significantly weaker than for nonspinning stars.

periods. In terms of $r_{\rm orb}$, nonspinning stars have $L \propto r_{\rm orb}^{-8/3}$, and rapidly spinning stars with $\sim$ ms periods have $L \propto r_{\rm orb}^{-1}$.

3.5 Luminosity Dependence on Inclination Angle

We now explore the dependence of electromagnetic luminosity on inclination angle of the tilted pulsar. Ioka & Taniguchi (2000) argue that the luminosity of orbiting point dipoles should vanish to lowest order when they are aligned and increase monotonically with inclination angle. Figure 5.23 shows the dependence of luminosity on inclination angle for nonspinning neutron stars at $r_{\rm orb}/R_* = 1.9$ and in vacuum. The bottom curve shows the luminosity of a single star in orbit, and the top curve shows the luminosity of a binary with one star tilted from the orbital angular velocity. We see that the luminosity does in fact increase monotonically with inclination angle, but with the luminosities of both a single star and a binary system at a comparable order of magnitude. The radiation fields of the oppositely moving aligned dipoles do not completely cancel, however. We have experimented with using larger and smaller stars, effectively changing our numerical stellar boundary condition, and find similar results. This property appears to be due to the large star size relative to the size of the orbit, that modifies the solution from a superposition of point dipoles. The strength of both the leading order radiation terms, especially electric dipole radiation, and the higher order multipoles can change. We end this discussion by noting that we do have a statistically significant result that the aligned dipoles radiate less than the antialigned dipoles, however.

Results presented in previous sections indicate that two stars immersed in a highly conducting plasma have very different properties from a single star in the same highly conducting plasma. This is borne out in Figure 5.24, which shows the dependence of luminosity on inclination angle for nonspinning neutron stars at $r_{\rm orb}/R_* = 1.9$. The bottom curve shows the luminosity of a single star in orbit, and the top curve shows the luminosity of a binary with one star tilted from the orbital angular velocity. The aligned binary luminosity is significantly higher than a single star due to the magnetic pressure field lines from each star exert on field lines from the other. As

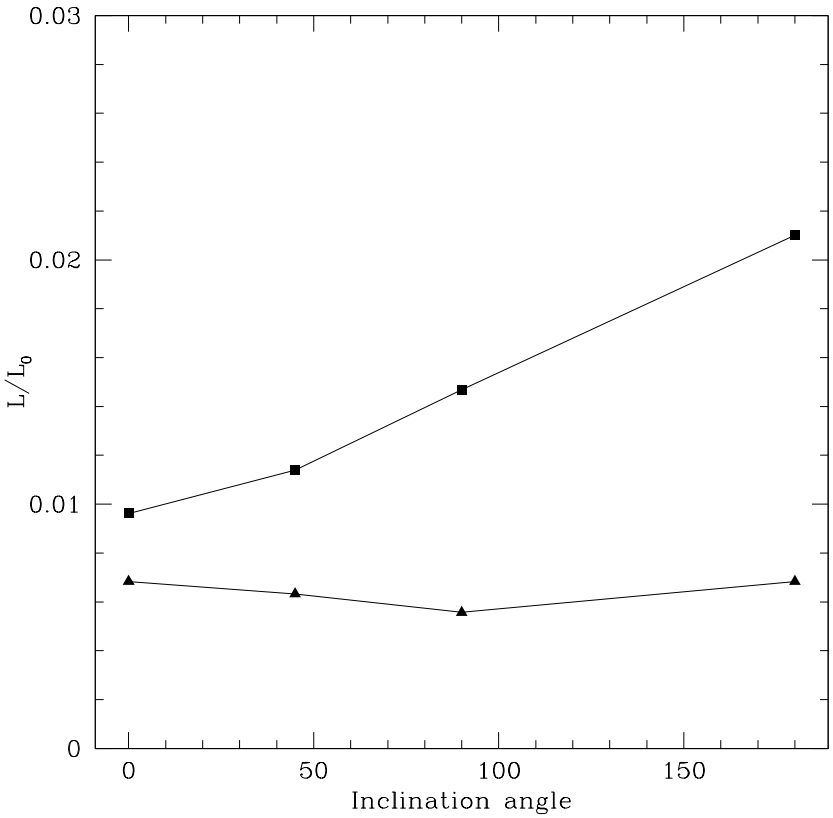

Figure 5.23: Electromagnetic luminosity as a function of inclination angle of the tilted star. The stars are not spinning, moving in vacuum, and have semimajor axis $r_{\rm orb}/R_* = 1.9$. Curves are shown for a single star in orbit (triangles) and an aligned binary (squares). Luminosity of the binary increases monotonically with inclination angle, but does not completely vanish at $\alpha = 0^\circ$ at this orbital separation.

inclination angle increases, more field lines can cross to the other side of the magnetosphere and force field lines coming off the other star to be swept backwards. The end result is that luminosity increases by a factor of 7 as α increases from 0° to 180°.

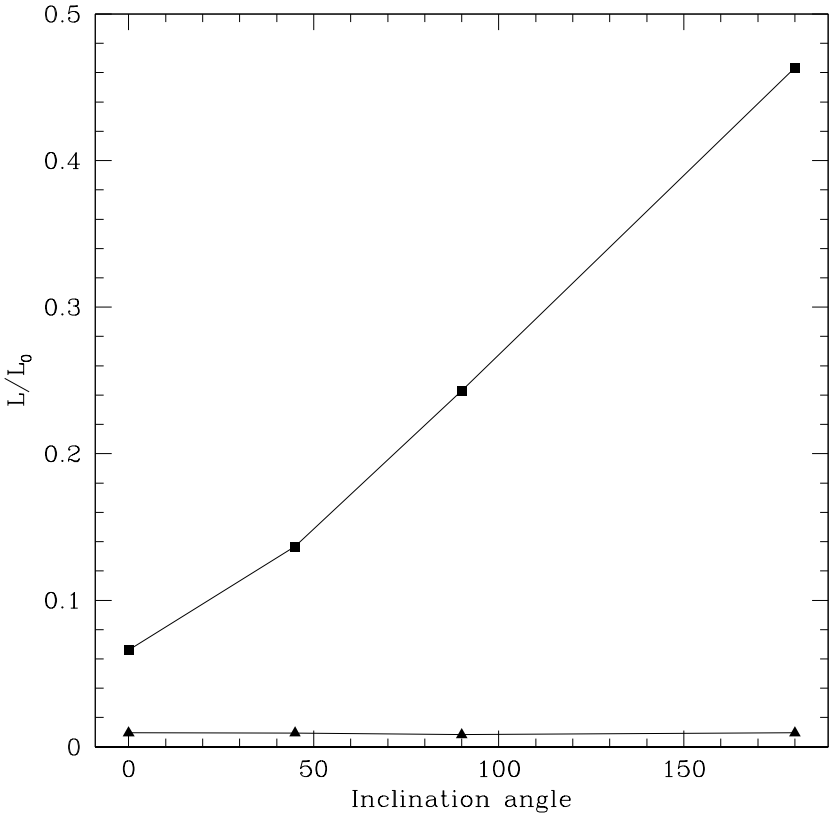

Figure 5.24: Electromagnetic luminosity as a function of inclination angle of the tilted star. The stars are not spinning, moving in a highly conducting plasma, and have semimajor axis $r_{\rm orb}/R_* = 1.9$. Curves are shown for a single star in orbit (triangles) and an aligned binary (squares). Luminosity is much stronger in the binary due to the magnetic pressure that field lines from each star exert on field lines from the other. Luminosity increases with inclination angle as more field lines can cross to the opposite side of the magnetosphere and force field lines coming off the other star backwards toroidally.

Rapidly spinning neutron stars present an entirely different problem. We have seen that the scaling of luminosity with orbital angular velocity is shallower than for nonspinning stars, and the inclination angle dependence of luminosity also differs. Figure 5.25 shows the dependence of luminosity on inclination angle for rapidly spinning neutron stars with $R_{\rm LC,*}/R_* = 2.7$ at

$r_{\rm orb}/R_* = 1.9$ and moving in a highly conducting plasma. The bottom curve shows the luminosity of a single star in orbit, and the top curve shows the luminosity of a binary with one star tilted from the orbital angular velocity. The luminosity of a single star rises with inclination angle due to additional displacement currents, until it is roughly three times as high as the aligned luminosity by $\alpha = 90$. The luminosity of the binary appears to be simply a sum of the luminosities of the two stars individually. Hence the luminosity peaks at $\alpha = 90^\circ$ and has comparable luminosities when $\alpha = 0^\circ$ and $\alpha = 180^\circ$.

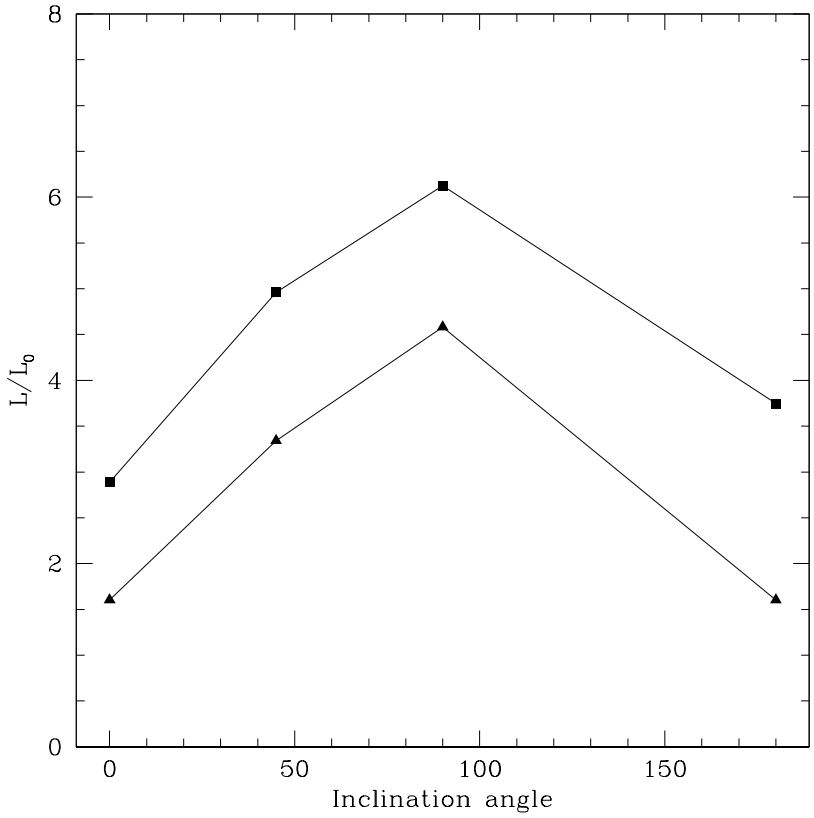

Figure 5.25: Electromagnetic luminosity as a function of inclination angle of the tilted star. The stars are spinning rapidly at $\sim$ ms periods, with $R_{\rm LC,*}/R_* = 2.7$, moving in a highly conducting plasma, and have semimajor axis $r_{\rm orb}/R_* = 1.9$. Curves are shown for a single star in orbit (triangles) and an aligned binary (squares). The luminosity of the binary appears to be a simple sum of the luminosities of the stars orbiting individually.

3.6 Angular Dependence of Poynting Flux

The ejected Poynting flux wind is not isotropic and has a strong angular dependence. Figure 5.26 shows the azimuthally integrated Poynting flux, $dL/d\theta$, as a function of polar angle for nonspinning stars moving in a highly conducting plasma. The semimajor of the orbit is $r_{\rm orb}/R_* = 1.9$ and the Poynting flux is calculated just beyond the orbital light cylinder. Vertical normalization of curves is arbitrary. Aligned and antialigned dipoles have radiation concentrated in two hollow cones several tens of degrees away from the rotation axis. The radiation from the binaries with one dipole tilted by $\alpha = 45°$ and $\alpha = 90°$ is asymmetric and preferentially beamed towards high polar angles $\theta \sim 150°$. Examining Figures 5.7 and 5.9, we see that field sweepback is larger in the bottom halves of the magnetosphere. Exterior pressure from field lines connected to the second star force field lines backwards toroidally, whereas field lines in the top halves can propagate outwards to infinity.

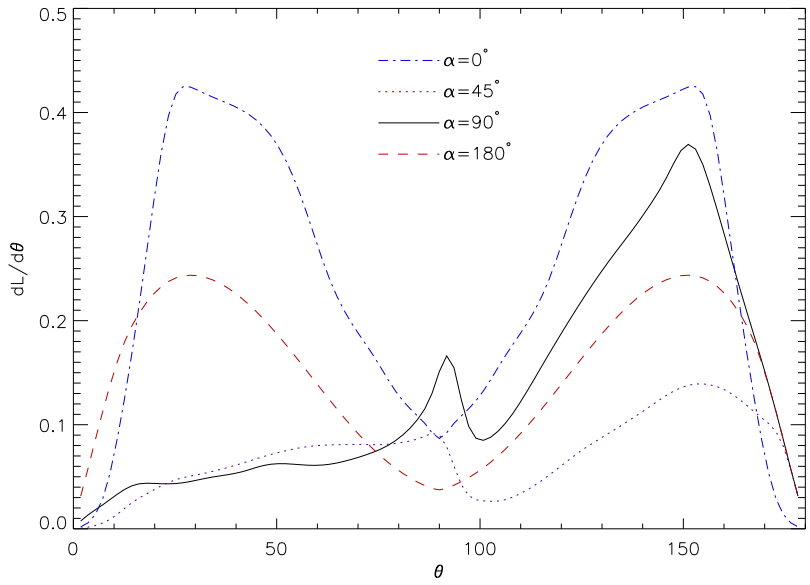

Figure 5.26: Poynting flux as a function of polar angle and integrated over the azimuthal direction. The stars are not spinning, moving in a highly conducting plasma, and have semimajor axis $r_{\rm orb}/R_* = 1.9$. Curves are shown for different inclination angle of the tilted star. Radiation is preferentially beamed towards $\theta \sim 30°, 150°$ for aligned and antialigned dipoles, but asymmetrically beamed towards 150° when $\alpha = 45°, 90°$.

Figure 5.27 shows the azimuthally integrated Poynting flux, $dL/d\theta$, as a function of polar angle for rapidly spinning stars with $R_{\rm LC,*}/R_* = 2.7$. The stars are moving in a highly conducting plasma, the semimajor of the orbits is $r_{\rm orb}/R_* = 1.9$, and the Poynting flux is calculated at the orbital light cylinder. Vertical normalization of curves is again arbitrary. Radiation is now concentrated towards angles near the equator for all inclination angles, as in the case for pulsars (e.g., Tchekhovskoy et al., 2013). The magnetospheres of the binaries with one dipole tilted by $\alpha = 45°$ and $\alpha = 90°$ are again asymmetric through the equatorial plane, resulting in small asymmetries in the radiation fields.

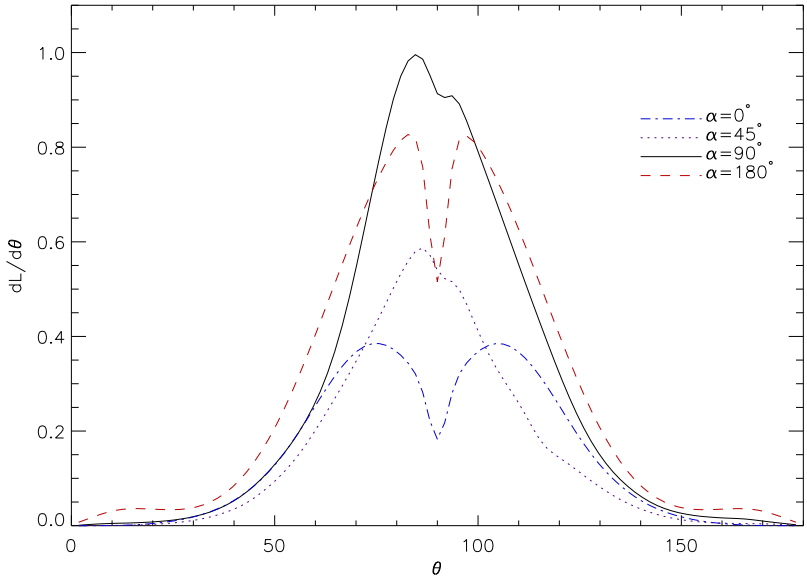

Figure 5.27: Poynting flux as a function of polar angle and integrated over the azimuthal direction. The stars are spinning rapidly at $\sim$ ms periods, with $R_{\rm LC,*}/R_* = 2.7$, moving in a highly conducting plasma, and have semimajor axis $r_{\rm orb}/R_* = 1.9$. Curves are shown for different inclination angle of the tilted star. Radiation is preferentially beamed towards angles near the equator for all inclination angles.

High-energy emission from neutron star magnetospheres need not necessarily be strictly correlated with the bulk Poynting flux outflow, however. If high-energy emission comes from particle acceleration in current sheets, then the geometric and dynamical properties of the currents would determine the properties of such emission. We explore this idea in more detail in Section 4.

4 Discussion

The results from Figure 5.20 have significant differences from those presented by Palenzuela et al. (2013b,a). Specifically, Palenzuela et al. (2013a) find flatter scalings of luminosity for aligned and antialigned binaries, closer to $\Omega^{3/2}$. Their case where one dipole dominates over the other, resembling our single star case, has a steeper scaling of luminosity proportional to Ω^{12} very close to contact. The reason for this discrepancy is due primarily to the way in which we measure electromagnetic energy losses. They measure Poynting flux at a fixed distance from the center of mass, which by the end of the inspiral is many orbital light cylinders. The ejected Poynting flux requires time to propagate to this surface, and so there is an effective time lag in their luminosity measurement. When we run the dynamical gravitational inspiral problem (c.f. Figure 5.20), we measure Poynting flux just inside the shrinking orbital light cylinder. This is more reflective of the actual electromagnetic energy losses. Indeed, the true instantaneous electromagnetic energy losses are probably best measured by fixing the semimajor axis and finding converged corotating solutions, as we do throughout the bulk of this work. Further, we note that our numerical results are in excellent agreement with the analytic expectations derived in Section 3.4.

The electromagnetic luminosity calculations of Paschalidis et al. (2013) for black hole - neutron star binaries also seem to suffer from the same biases associated with measuring Poynting flux at a fixed surface far from the binary. Namely, the luminosity is very flat with time and does not increase appreciably as the binary inspirals. We expect the black hole - neutron star binary problem to be similar to the case of a single orbiting magnetized star presented in this work, and hence have luminosity scaling close to $L \propto \Omega^{14/3}$ for a nonspinning neutron star.

Our fiducial luminosity $L_0 = \mu^2 \Omega_*^4 / c^3 \approx 6 \times 10^{44}$ ergs s^{-1}, where we have assumed $\Omega_* = (3/8)c/R_*$, $R_* = 10$ km, and surface magnetic field strength $B_0 = 10^{12}$ G. Hence, we predict a total electromagnetic energy output rate in the range of $10^{44} - 10^{46}$ ergs s^{-1} just before merger, depending on the inclination angles of the magnetic moments of the stars, the spin angular velocity of the stars, and also the surface dipole field strength. The number of known double neutron star binaries is only of order 10 (Lorimer, 2008), and so we do not have good statistics on

the distribution of stellar spins in these systems. The fastest spinning pulsar in a double neutron star binary has period 22.7 ms (Burgay et al., 2003), but spin periods can in principle range from seconds all the way down to milliseconds, depending on the neutron star and binary formation scenarios. Millisecond pulsars are thought to be neutron stars in Low-Mass X-ray Binaries spun up by accreting matter from a stellar mass companion overfilling its Roche lobe (Alpar et al., 1982; Radhakrishnan & Srinivasan, 1982). Double neutron star systems where one or both stars are spinning at $\sim$ ms periods are thus likely not the most common configuration, though some evidence suggests there are other ways of producing millisecond pulsars (Kiziltan & Thorsett, 2009). If the progenitors are in fact spinning rapidly with $\sim$ ms periods, the luminosity near contact will be close to $L \approx 10^{46}$ ergs s^{-1}. If one or both pulsars are instead spinning more slowly with periods on the order of seconds, as we expect at the evolutionary end stage of a High-Mass X-ray Binary, the luminosity will be closer to $L \approx 10^{44} - 10^{45}$ ergs s^{-1} .

The above electromagnetic energy outputs are still very significant, and give hope for observing electromagnetic signals from the neutron star mergers that will soon be observed in gravitational waves by Advanced LIGO. In fact, neutron star mergers are estimated to have the highest event rate among all candidate sources detectable by Advanced LIGO and Advanced Virgo, ~ 40 / yr (Abadie et al., 2010). Stellar spins are known to affect the gravitational wave templates (Brown et al., 2012), and our results suggest that the Poynting flux wind also depends strongly on the magnitude of the stellar spins. This raises the possibility of constraining both the gravitational physics and the plasma physics processes in the environment surrounding the neutron star binaries. The Poynting flux wind is largely invisible, however, unless converted directly to emission via current sheets, or if it shocks and creates an afterglow at larger radius (Medvedev & Loeb, 2013). At present the efficiency of conversion of the Poynting flux wind to observable radiation is still unknown, but we note that a Poynting luminosity of $L \approx 10^{44}$ ergs s^{-1} corresponds to an isotropic energy flux of 10^{-9} ergs s^{-1} cm^{-2} at 100 Mpc, within the realm of detectability.

Short-duration GRB's generally have redshifts $z < 1$ (Prochaska et al., 2006), and it not known how well collimated the prompt emission is (Grupe et al., 2006; Watson et al., 2006). Precursor

emission (Troja et al., 2010) originating in the magnetosphere would have to be sufficiently energetic and beamed to propagate over large distances to the observer. Particle acceleration in current sheets has been explored in the context of gamma-ray pulsars, and is a possible candidate mechanism to produce precursor emission (e.g., Bai & Spitkovsky, 2010; Li et al., in prep.). The strong magnetic fields surrounding neutron stars provide a large energy reservoir that can be tapped at reconnection sites, potentially accelerating particles to high Lorentz factors. Such emission would be strongly beamed toward the observer, improving its prospects for detection.

In gamma-ray pulsars we have proposed that particles are accelerated to high Lorentz factors along magnetic field lines before entering the sheet, where they are heated, beaming high-energy emission along the direction of upstream magnetic fields (Li et al., in prep.). In the context of this model our results suggest that for neutron stars in orbit around each other with aligned magnetic moments and equal spins, emission is beamed radially outward in the equatorial current sheet and in the vertical direction along the plane equidistant from the two neutron stars. If the prompt GRB emission were also beamed strongly along the rotation axis, then the observer could potentially see precursor emission from this vertical current sheet. For neutron stars with antialigned magnetic moments and equal spins, high-energy emission from both current sheets would be beamed more toward intermediate latitudes centered on the equator. We would not see short-duration GRB precursor emission, but could still potentially see an electromagnetic counterpart to an Advanced LIGO gravitational wave source.

In the results presented in this work up to this point we have restricted the stellar spins of the two stars to be equal to each other for simplicity. We have further experimented with cases where one star is not spinning and the other is spinning rapidly, of observational relevance, and find luminosities intermediate between the cases where both stars are not spinning and both stars are spinning rapidly. The current sheet configuration has more noteworthy changes, however, with a curved vertical sheet in both the aligned and antialigned dipole cases. A discontinuity in magnetic field lines develops where the magnetospheres of the two stars touch or stitch together, possibly generating short-duration GRB precursor emission in these cases. Introducing nonzero spin obliquity angles, as well as allowing for arbitrary orientations of the magnetic axes of both stars,

complicate the problem further. They are straightforward to include but are beyond the scope of this exploratory work, however.

The heuristic arguments for high-energy radiation presented here may represent the limit of how far we can interpret our results. Further details and a microphysical model of precursor emission await more advanced codes that include additional information about particle dynamics in current sheets.

Bibliography

Abadie, J., Abbott, B. P., Abbott, R., Abernathy, M., Accadia, T., Acernese, F., Adams, C., Adhikari, R., Ajith, P., Allen, B., & et al. 2010, Classical and Quantum Gravity, 27, 173001

Alpar, M. A., Cheng, A. F., Ruderman, M. A., & Shaham, J. 1982, Nat, 300, 728

Bai, X.-N. & Spitkovsky, A. 2010, ApJ, 715, 1282

Bérenger, J.-P. 2007, Synthesis Lectures on Computational Electromagnetics, 2, 1

Brown, D. A., Harry, I., Lundgren, A., & Nitz, A. H. 2012, Phys. Rev. D, 86, 084017

Burgay, M., D'Amico, N., Possenti, A., Manchester, R. N., Lyne, A. G., Joshi, B. C., McLaughlin, M. A., Kramer, M., Sarkissian, J. M., Camilo, F., Kalogera, V., Kim, C., & Lorimer, D. R. 2003, Nat, 426, 531

Drell, S. D., Foley, H. M., & Ruderman, M. A. 1965, J. Geophys. Res., 70, 3131

Gedney, S. D. 2011, Synthesis Lectures on Computational Electromagnetics, 6, 1

Goldreich, P. & Lynden-Bell, D. 1969, ApJ, 156, 59

Grupe, D., Burrows, D. N., Patel, S. K., Kouveliotou, C., Zhang, B., Mészáros, P., Wijers, R. A. M., & Gehrels, N. 2006, ApJ, 653, 462

Hansen, B. M. S. & Lyutikov, M. 2001, MNRAS, 322, 695

Heras, J. A. 1994, American Journal of Physics, 62, 1109

Ioka, K. & Taniguchi, K. 2000, ApJ, 537, 327

Jackson, J. D. 1998, Classical Electrodynamics, 3rd Edition

Kalapotharakos, C. & Contopoulos, I. 2009, A&A, 496, 495

Kelley, L. Z., Mandel, I., & Ramirez-Ruiz, E. 2013, Phys. Rev. D, 87, 123004

Kiziltan, B. & Thorsett, S. E. 2009, ApJ, 693, L109

Lai, D. 2012, ApJ, 757, L3

Li, J., Spitkovsky, A., & Tchekhovskoy, A. in prep.

Lipunov, V. M. & Panchenko, I. E. 1996, A&A, 312, 937

Lorimer, D. R. 2008, Living Reviews in Relativity, 11, 8

Lyutikov, M. 2011, Phys. Rev. D, 83, 124035

McWilliams, S. T. & Levin, J. 2011, ApJ, 742, 90

Medvedev, M. V. & Loeb, A. 2013, MNRAS, 431, 2737

Nakar, E. 2007, Phys. Rep., 442, 166

Palenzuela, C., Garrett, T., Lehner, L., & Liebling, S. L. 2010, Phys. Rev. D, 82, 044045

Palenzuela, C., Lehner, L., Liebling, S. L., Ponce, M., Anderson, M., Neilsen, D., & Motl, P. 2013a, Phys. Rev. D, 88, 043011

Palenzuela, C., Lehner, L., Ponce, M., Liebling, S. L., Anderson, M., Neilsen, D., & Motl, P. 2013b, Physical Review Letters, 111, 061105

Paschalidis, V., Etienne, Z. B., & Shapiro, S. L. 2013, Phys. Rev. D, 88, 021504

Piro, A. L. 2012, ApJ, 755, 80

Prochaska, J. X., Bloom, J. S., Chen, H.-W., Foley, R. J., Perley, D. A., Ramirez-Ruiz, E., Granot, J., Lee, W. H., Pooley, D., Alatalo, K., Hurley, K., Cooper, M. C., Dupree, A. K., Gerke, B. F., Hansen, B. M. S., Kalirai, J. S., Newman, J. A., Rich, R. M., Richer, H., Stanford, S. A., Stern, D., & van Breugel, W. J. M. 2006, ApJ, 642, 989

Radhakrishnan, V. & Srinivasan, G. 1982, Current Science, 51, 1096

Spitkovsky, A. 2006, ApJ, 648, L51

Taflove, A. & Hagness, S. 2005, Computational Electrodynamics: The Finite-Difference Time-Domain Method, 3rd edn. (Norwood, MA: Artech House)

Tchekhovskoy, A., Spitkovsky, A., & Li, J. G. 2013, MNRAS, 435, L1

Troja, E., Rosswog, S., & Gehrels, N. 2010, ApJ, 723, 1711

Vietri, M. 1996, ApJ, 471, L95

Watson, D., Hjorth, J., Jakobsson, P., Xu, D., Fynbo, J. P. U., Sollerman, J., Thöne, C. C., & Pedersen, K. 2006, A&A, 454, L123

Chapter 6

Conclusion

In summary, we have formulated a resistive force-free method that allows us to account for variable plasma supply and accelerating electric fields in the magnetospheres of neutron stars. We then use a time-dependent numerical code to evolve Maxwell's equations and explore the neutron star magnetospheric structure. We first applied our method in Chapter 2 to study the magnetospheres of pulsars surrounded by resistive plasma. We find a family of resistive solutions that smoothly bridges the gap between the vacuum and the force-free magnetosphere solutions. The spin-down luminosity, open field line potential drop, and the fraction of open field lines all transition between the vacuum and force-free values as the plasma conductivity varies from zero to infinity. For fixed inclination angle, we find that the spin-down luminosity depends linearly on the open field line potential drop.

In Chapter 3, we used a variable conductivity to construct models for recently discovered intermittent pulsars that switch between two distinct states: an "on", radio-loud state, and an "off", radio-quiet state. Spin-down rates in the two states differ by a large factor, $\sim 1.5 - 2.5$, which is not easily understood in the context of current models. We model the "on" state as a nearly ideal force-free magnetosphere with abundant magnetospheric plasma supply. The lack of radio emission in the "off" state is associated with plasma supply disruption that results in lower plasma density on the open field lines. We model the "off" state using nearly vacuum conditions on the open field lines and nearly ideal force-free conditions on the closed field lines, where plasma can remain trapped even in the absence of pair production. The toroidal advection of plasma in the closed zone in the "off" state causes spin-downs that are a factor of ~ 2 higher than vacuum values, and we naturally obtain a range of spin-down ratios between the "on" and "off"

states, $\sim 1.2 - 2.9$, which corresponds to a likely range of pulsar inclination angles of $30-90^\circ$. We consider also the implications of our model to a number of poorly understood but possibly related pulsar phenomena, including nulling, timing noise, and rotating radio transients.

The parallel electric fields in our method allow us to potentially model the acceleration of particles in the pulsar magnetospheres. In Chapter 4 we examined the possibility that the high-energy emission from γ-ray pulsars comes from reconnecting current sheets and current layers near and beyond the light cylinder. We considered several different physically motivated prescriptions for beaming of particles from inside the current sheets. In our best working model, the reconnected magnetic field provides a reservoir of energy that heats particles, and synchrotron photons may be beamed to GeV energies by relativistic outflow. We find that emitting particles that fly outwards in magnetic flux ropes are confined to the sheet, and the geometric shape of the sheet naturally gives rise to a strong caustic on the skymap and double peaked light curves for a broad range of observer angles. We also conclude that interpulse bridge emission likely arises from interior to the light cylinder, along last open field lines that traverse the space between the polar caps and the current sheet.

Finally, in Chapter 5 we used our code to solve for the electromagnetic field structure surrounding both a single neutron star orbiting a center of mass, and binary neutron star systems that can be observed by the next generation of gravitational wave detectors. We study the magnetospheric field structure, current sheets, and electromagnetic rotational energy losses for arbitrarily inclined and spinning neutron stars. Analytic and numerical results suggest that the scaling of electromagnetic luminosity with orbital angular velocity Ω varies between Ω^4 for nonspinning stars to $\Omega^{3/2}$ for rapidly spinning millisecond pulsars near contact. We note that high-energy emission from current sheets may have a component preferentially beamed towards the poles for neutron stars with equal spins and aligned magnetic moments, or unequal spins and arbitrary magnetic inclinations, possibly generating precursor emission to short-duration Gamma-ray Bursts.

The initial hope of our work was to use the information encoded in the finite parallel electric fields to directly determine particle trajectories, and thus, radiative properties. This goal proved

to be too ambitious, however, and we had to settle for using the improved solutions of gross magnetospheric properties to provide a heuristic picture of particle acceleration and high-energy emission from γ-ray pulsars. The chief ambiguity lies in the fact that the instantaneous velocity of a particle depends on its whole past history of acceleration. We could in theory trace particles in our code using a Boris pusher, but even such a prescription would miss crucial physics in the vacuum gap above the polar cap (Timokhin & Arons, 2013; Chen & Beloborodov, 2013). Particles may be accelerated to Lorentz factors exceeding $\gamma = 10^4$ above the polar caps, and this effect must be included in any self-consistent determination of particle dynamics. Another potential shortcoming is that our method lacks the true backreaction of particle motion on the fields, and it is not entirely clear that tracing particles in our method would give the same trajectories as particle-in-cell (PIC) simulations of relativistic pair plasma current sheets. Obviously a full PIC simulation of the pulsar would be a major step forward, but resolving the relevant current sheet length scales and implementing realistic stellar boundary conditions to capture the polar gaps remain elusive.

An alternate path forward lies with solving the equations of magnetohydrodynamics (MHD) applied to pulsars. Tchekhovskoy et al. (2013) have made initial progress by solving the arbitrarily inclined ideal MHD pulsar magnetospheres, which are very similar to the ideal force-free solutions. The MHD fluid velocity contains important information about emission, however, and injecting particles with non-zero velocity at the stellar surface could capture elements of the polar gap physics. This method is still ideal, however, and necessarily underresolves current sheets. The next step forward would be to implement a resistive MHD method that could potentially resolve microphysical properties of the current sheets, and also model the polar gaps, allowing for particle acceleration and differential rotation of field lines (e.g. Contopoulos & Spitkovsky, 2006).

I would like to conclude by noting that both the PIC and resistive MHD methods offer enormous promise to further illuminate the dynamical properties of neutron star magnetospheres. Microphysical models of emission from pulsar and binary neutron star magnetospheres are now within grasp.

Bibliography

Chen, A. Y. & Beloborodov, A. M. 2013, ApJ, 762, 76

Contopoulos, I. & Spitkovsky, A. 2006, ApJ, 643, 1139

Tchekhovskoy, A., Spitkovsky, A., & Li, J. G. 2013, MNRAS, 435, L1

Timokhin, A. N. & Arons, J. 2013, MNRAS, 429, 20

List of Figures

1.1 Light curves for 7 pulsars in radio through γ-rays. Image courtesy Thompson (2004). 2

1.2 Radio and γ-ray light curves for the Vela pulsar from the Fermi GST (Abdo et al., 2010). γ-ray light curves have a characteristic double-peaked shape. 2

1.3 $P - \dot{P}$ diagram for a large population of ordinary and millisecond pulsars (Cordes et al., 2004). 3

1.4 Vacuum magnetic fields in the equatorial plane of an orthogonal rotator (Michel & Li, 1999). The ejection of wound up toroidal field carries off electromagnetic energy. 4

1.5 Goldreich-Julian model of a pulsar magnetosphere filled with abundant plasma (Goldreich & Julian, 1969). Field lines open up beyond the light cylinder, and the electric field is the corotation field. 6

1.6 Cartesian Yee cell used in FDTD methods. **E** is defined on cell edges and and **B** on cell faces to simplify the calculation of numerical curls. Image courtesy Werner & Cary (2007). 9

2.1 Magnetic field lines in the $\mu - \mathbf{\Omega}$ plane for a 60° inclined dipole. Color represents out-of-plane magnetic field into (red) and out of (blue) the page. The color table shows only values up to 30% of the maximum of the out-of-plane magnetic field, and a square root stretching has been applied to its magnitude. The maximum out-of-plane magnetic field values are given in Table 2.1. Conduction and displacement currents weaken with decreasing conductivity. (a) force-free dipole; (b) resistive dipole at $(\sigma/\Omega)^2 = 40$; (c) $(\sigma/\Omega)^2 = 4$; (d) $(\sigma/\Omega)^2 = 0.4$; (e) $(\sigma/\Omega)^2 = 0.04$; (f) vacuum dipole. 24

2.2 Spin-down luminosity dependence on inclination angle for force-free, a sequence of resistive, and vacuum dipoles. Spin-down is normalized by 3/2 times the spin-down power of the orthogonal vacuum rotator. We see a smooth monotonic transition from force-free to vacuum with decreasing conductivity. 27

2.3 Open field line potential drop with inclination angle for force-free, a sequence of resistive, and vacuum dipoles. Results are normalized to $V_0 = |\mu|/R_{\rm LC}R_*$. For $(\sigma/\Omega)^2 > 0.04$ the potential drop is relatively independent of inclination angle. . . . 30

2.4 Spin down dependence on the open field line potential drop for a sequence of different inclination angles, $\alpha = 0°, 30°, 60°$, and $90°$. Potential drop is normalized to $V_0 = |\mu|/R_{\rm LC}R_*$ and luminosity to 3/2 the spin-down of the orthogonal vacuum rotator. For $V_{\rm drop}/V_0 < 0.2$ spin-down falls linearly with potential drop. 31

2.5 Poynting flux with radius for force-free, a sequence of resistive, and vacuum dipoles inclined at $\alpha = 60°$. The resistive Poynting flux values slope downwards with increasing radius, reflecting magnetospheric dissipation. Results are normalized to the force-free spin-down value on the star. 34

2.6 Magnetic field lines in the $\mu - \mathbf{\Omega}$ plane for a 60° inclined dipole at conductivity $(\sigma/\Omega)^2 = 4$. Color represents the out-of-plane drift velocity in the corotating frame, with blue color representing the out of the page direction. There is retrograde differential rotation about the axis with maximum potential drop, situated roughly halfway between the rotation and magnetic axes when inside the light cylinder, as well as about the boundary of the closed field line region. The maximum value on the color table corresponds to a drift velocity of $0.8c$. 39

3.1 Change in frequency over time and timing residual for the intermittent pulsar from Kramer et al. (2006). The Spin-down rate is different when radio is observed and when no radio is observed. 44

3.2 Magnetic field lines in the $\mu - \mathbf{\Omega}$ plane for inclined dipoles at $\alpha = 30°$ (top), $\alpha = 60°$ (middle), $\alpha = 90°$ (bottom). Color is representative of out-of-plane magnetic field into (red) and out of (blue) the page. The left column shows the "off" state with abundant plasma in the closed zone and vacuum-like conditions along open field lines. The red curves indicate the intersection with the $\mu - \mathbf{\Omega}$ plane of the demarcation surface between these distinct conducting and vacuum-like regions. Gross features of the magnetosphere in the "off" state are vacuum-like, but the "off" states have more magnetic flux passing through the light cylinder and stronger magnetic field sweepback than vacuum solutions. The right column represents the "on" state with abundant plasma everywhere. 48

3.3 Magnetic field lines in the $\mu - \mathbf{\Omega}$ plane for a vacuum inclined dipole at $\alpha = 60°$. Color is representative of out-of-plane magnetic field into (red) and out of (blue) the page. There is large closed field line region, and displacement currents circulate and contribute to spin-down. 49

3.4 Spin-down luminosity dependence on inclination angle for the force-free–like "on" state, the "off" state, and the vacuum solution. The "off" state spin-down naturally lies between the force-free and vacuum spin-down values for all inclination angles. spin-down is normalized by 3/2 times the spin-down power of the orthogonal vacuum rotator. 50

3.5 The ratio of spin-down power between the "on" and "off" states, $f_{\mathrm{on}\to\mathrm{off}}$, as a function of inclination angle. We obtain $f_{\mathrm{on}\to\mathrm{off}} \sim 1.2 - 2.9$ for $\alpha > 30°$. Known intermittent pulsars have $f_{\mathrm{on}\to\mathrm{off}}$ in this range. 52

4.1 Radio and γ-ray light curves for the Vela pulsar from the Fermi GST (Abdo et al., 2010). γ-ray light curves have a characteristic double-peaked shape, with bridge emission seen between the first and second peaks. The first γ-ray peak trails radio emission by 0.13 P. 59

4.2 Current sheet and open field lines with footpoints near the edge of the polar cap. The left panel shows the 60 degree inclined rotator, and the right panel the 90 degree rotator. Red field lines originate on the north polar cap and green field lines in the right panel originate on the south polar cap. 62

4.3 The current sheet shape for a 60 degree inclined dipole (left), and a split monopole (right), extending out to $\sim 25R_{\rm LC}$. Color in the left panel is RB_ϕ, and streamlines trace magnetic fields in the $\mu - \mathbf{\Omega}$ plane. The current sheet shape is similar in both cases, but the dipole sheet extends closer to the rotation axis. 63

4.4 Example of an analytic 1D current sheet in our resistive force-free method. This particular sheet is reconnecting at the speed of light. Current has been normalized arbitrarily. 66

4.5 Skymaps for emission from the current sheet between $r = 1.1 - 1.5R_{\rm LC}$ for a $\alpha = 60^\circ$ rotator. Emission is beamed along $\mathbf{E}_{\rm fluid}$ (top), along $\mathbf{j}$ (2nd panel), along the upstream magnetic field $\mathbf{B}_{\rm up}$ extrapolated into the sheet (3rd panel), a combination of $\mathbf{B}_{\rm up}$ and $[\nabla(j_\sigma/B)]\times\mathbf{B}_{\rm up}$ (4th panel), and a combination of $\mathbf{B}_{\rm up}$ and $-[\nabla(j_\sigma/B)]\times\mathbf{B}_{\rm up}$ (bottom). Of these models, beaming along $\mathbf{B}_{\rm up}$ works best, producing a strong caustic and reasonable phase offset from possible radio emission at the magnetic poles. 70

4.6 Skymaps for radial beaming of emission from the current sheet for a 60 degree inclined rotator. The top panel shows emission from between $r = 1.1 - 1.5R_{\rm LC}$, and the bottom panel shows emission from the wind zone between $r = 2.1 - 2.3R_{\rm LC}$. In both cases there is a strong caustic on the skymap and double peaked light curves for a broad range of inclination angles due to the special geometric shape of the current sheet. 73

4.7 Last open field lines in 3 dimensions, and projected onto the skymap. Pulsar inclination angle is 60 degrees. Field lines satisfy $r_{\rm ov} = 0.98$ and are traced to the light cylinder. These field lines traverse the space between polar cap and the current sheet both in real space and on the skymap. 76

4.8 Skymap for Separatrix Layer model, where pulsar inclination angle is 60 degrees. Emission is taken from $r_{\rm ov} = 0.98$, interior to the light cylinder. There is a weak caustic on the skymap produced by emission from near the light cylinder, and strong bridge emission between the first and second γ-ray peaks. 77

4.9 Skymaps for current layer (top), current sheet (middle), and both the current layer and current sheet (bottom), for a 30 degree inclined pulsar. The combined model has strong double peaks and bridge emission between the first and second γ-ray peaks. Blue light curves in the bottom panel isolate emission from the current layer, while black curves show total emission from both the current layer and current sheet. . . 79

4.10 Skymaps for current layer (top), current sheet (middle), and both the current layer and current sheet (bottom), for a 60 degree inclined pulsar. The combined model has strong double peaks and bridge emission between the first and second γ-ray peaks. Blue curves in the bottom panel show emission only from the current layer. The light curve at $\xi_{\rm obs} = 60^\circ$ has a phase offset from possible radio emission at the north magnetic pole of ~ 0.19 P. 81

4.11 Skymaps for current layer (top), current sheet (middle), and both the current layer and current sheet (bottom), for a 90 degree inclined pulsar. There is a strong caustic on the skymap and double peaked light curves for a broad range of inclination angles. Blue light curves in the bottom panel show emission only from the current layer . . 82

5.1 Magnetic field lines of a single neutron star on an orbit and μ parallel to $\mathbf{\Omega}$. The light cylinder $R_{\rm LC} = c/\Omega$, and color represents out-of-plane field. The star is not spinning, i.e., $R_{{\rm LC},*} = \infty$. Field lines resemble those of a point dipole, but are weakly swept backwards by orbital motion. 95

5.2 Magnetic field lines of a single neutron star on an orbit and μ parallel to $\mathbf{\Omega}$. The light cylinder $R_{\rm LC} = c/\Omega$, and color represents out-of-plane field. The star is spinning rapidly at $\sim$ ms periods, with $R_{{\rm LC},*}/R_* = 2.7$. Field lines resemble those of a force-free pulsar. 96

5.3 Magnetic field lines of orbiting binary neutron stars and μ of both stars parallel to $\mathbf{\Omega}$. The light cylinder $R_{\rm LC} = c/\Omega$, and color represents out-of-plane field. The stars are not spinning, i.e., $R_{{\rm LC},*} = \infty$. Fields from each star feel magnetic pressure of field lines from the other star, forcing magnetic field lines backwards toroidally. Field lines reconnect through a vertical current sheet coincident with the rotation axis. . 97

5.4 Magnetic field lines of orbiting binary neutron stars and μ of both stars parallel to $\mathbf{\Omega}$. The light cylinder $R_{\rm LC} = c/\Omega$, and color represents out-of-plane field. The stars are spinning rapidly at $\sim$ ms periods, with $R_{{\rm LC},*}/R_* = 2.7$. Magnetic fields are pulsar-like interior to $\sim 2R_{\rm LC}$, but feel the orbital effects beyond this distance. Field lines reconnect through a vertical current sheet coincident with the rotation axis. . 97

5.5 Magnetic field lines of orbiting binary neutron stars and μ of left star tilted from $\mathbf{\Omega}$ by angle $\alpha = 180^\circ$. The light cylinder $R_{\rm LC} = c/\Omega$, and color represents out-of-plane field. The stars are not spinning, i.e., $R_{{\rm LC},*} = \infty$. Fields from each star are forced backwards by a confining pressure from field lines attached to the other star. 98

5.6 Magnetic field lines of orbiting binary neutron stars and μ of left star tilted from $\mathbf{\Omega}$ by angle $\alpha = 180^\circ$. The light cylinder $R_{\rm LC} = c/\Omega$, and color represents out-of-plane field. The stars are spinning rapidly at $\sim$ ms periods, with $R_{{\rm LC},*}/R_* = 2.7$. Magnetic fields are pulsar-like interior to $\sim 2R_{\rm LC}$, but feel the orbital effects beyond this distance. 98

5.7 Magnetic field lines of orbiting binary neutron stars and μ of left star tilted from $\mathbf{\Omega}$ by angle $\alpha = 45^\circ$. The light cylinder $R_{\rm LC} = c/\Omega$, and color represents out-of-plane field. The stars are not spinning, i.e., $R_{{\rm LC},*} = \infty$. Most field lines open outwards, but a few connect between the stars. 99

5.8 Magnetic field lines of orbiting binary neutron stars and μ of left star tilted from $\mathbf{\Omega}$ by angle $\alpha = 45^\circ$. The light cylinder $R_{\rm LC} = c/\Omega$, and color represents out-of-plane field. The stars are spinning rapidly at $\sim$ ms periods, with $R_{{\rm LC},*}/R_* = 2.7$. Magnetic fields are determined primarily by stellar spin interior to $\sim 2R_{\rm LC}$. 100

5.9 Magnetic field lines of orbiting binary neutron stars and μ of left star tilted from $\mathbf{\Omega}$ by angle $\alpha = 90°$. The light cylinder $R_{\rm LC} = c/\Omega$, and color represents out-of-plane field. The stars are not spinning, i.e., $R_{{\rm LC},*} = \infty$. Fewer field lines open outwards and more connect between the stars as compared to at lower α. 100

5.10 Magnetic field lines of orbiting binary neutron stars and μ of left star tilted from $\mathbf{\Omega}$ by angle $\alpha = 90°$. The light cylinder $R_{\rm LC} = c/\Omega$, and color represents out-of-plane field. The stars are spinning rapidly at $\sim$ ms periods, with $R_{{\rm LC},*}/R_* = 2.7$. Magnetic fields are dominated by stellar spin interior to $\sim 2R_{\rm LC}$. 101

5.11 Magnetic field lines and current sheets for an orbiting neutron star binary with the magnetic moments of both stars aligned with the rotation axis. The stars are not spinning, i.e., $R_{{\rm LC},*} = \infty$. Fields are by and large confined to the half of the magnetosphere closer to their source star. 102

5.12 Magnetic field lines and current sheets for an orbiting neutron star binary with the magnetic moments of both stars aligned with the rotation axis. The stars are spinning rapidly at $\sim$ ms periods, with $R_{{\rm LC},*}/R_* = 2.7$. Stellar spin winds fields backwards toroidally, and they can propagate to the far side of the magnetosphere closer to the opposing star. 103

5.13 Magnetic field lines and current sheets for an orbiting neutron star binary with the magnetic moment of one star aligned with the rotation axis, and the magnetic moment of the other star tilted and antialigned with the rotation axis. The stars are not spinning, i.e., $R_{{\rm LC},*} = \infty$. Fields from each star encircle the other star and force fields coming off the second star backwards toroidally. 105

5.14 Magnetic field lines and current sheets for an orbiting neutron star binary with the magnetic moment of one star aligned with the rotation axis, and the magnetic moment of the other star tilted and antialigned with the rotation axis. The stars are spinning rapidly at $\sim$ ms periods, with $R_{{\rm LC},*}/R_* = 2.7$. Stellar spin winds fields backwards toroidally. 106

5.15 Extended wind-zone magnetosphere of orbiting binary neutron stars and μ of both stars parallel to $\mathbf{\Omega}$. Color represents out-of-plane field, and the stars are not spinning, i.e., $R_{\mathrm{LC},*} = \infty$. Vertical and equatorial current sheets extend outwards, and field lines beyond the light cylinder $R_{\mathrm{LC}} = c/\Omega$ feel significant pressure from field lines attached to the other star as the orbit progresses. 108

5.16 Extended wind-zone magnetosphere of orbiting binary neutron stars and μ of both stars parallel to $\mathbf{\Omega}$. Color represents out-of-plane field, and the stars are spinning rapidly at $\sim$ ms periods, with $R_{\mathrm{LC},*}/R_* = 2.7$. The pulsar-like magnetic fields are truncated at $\sim 2R_{\mathrm{LC}} = 2c/\Omega$, and significantly deformed by magnetic from the opposing star beyond this distance as the stars orbit. Equatorial and vertical current sheets extend outwards. 109

5.17 Extended wind-zone magnetosphere of orbiting binary neutron stars and μ of left star tilted from $\mathbf{\Omega}$ by angle $\alpha = 180°$. Color represents out-of-plane field, and the stars are not spinning, i.e., $R_{\mathrm{LC},*} = \infty$. Field lines switch which star they attach to with increasing distance from the stars, and current sheets reverse direction, both occurring on a distance scale of the light cylinder $R_{\mathrm{LC}} = c/\Omega$. 109

5.18 Extended wind-zone magnetosphere of orbiting binary neutron stars and μ of left star tilted from $\mathbf{\Omega}$ by angle $\alpha = 180°$. Color represents out-of-plane field, and the stars are spinning rapidly at $\sim$ ms periods, with $R_{\mathrm{LC},*}/R_* = 2.7$. Pulsar-like magnetic fields are truncated at $\sim 2R_{\mathrm{LC}} = 2c/\Omega$, with successive sequences of fields switching which star they attach to and reversing current sheets, as distance from the stars increases. 110

5.19 Electromagnetic luminosity as a function of the semimajor axis of the neutron star orbits. The neutron stars are moving in vacuum and are not spinning, i.e., $R_{\mathrm{LC},*} = \infty$. Curves are shown for a single star in orbit, an aligned binary, and an antialigned binary. The scaling of L with Ω is close to theoretically expected results. 114

5.20 Electromagnetic luminosity as a function of the semimajor axis of the neutron star orbits. The neutron stars are moving in a highly conducting plasma and are not spinning, i.e., $R_{\mathrm{LC},*} = \infty$. Curves are shown for a single star in orbit, an aligned binary, and an antialigned binary. Open triangles represent the luminosity of an aligned binary on a dynamically shrinking orbit. Scaling of luminosity with Ω is close to theoretical expectations, but the magnitude of luminosity is much higher in binaries due to interacting pressure of field lines. 116

5.21 Electromagnetic luminosity as a function of the semimajor axis of a single neutron star orbiting a center of mass in a highly conducting plasma. Curves are shown for different stellar spins, with $R_{\mathrm{LC},*}/R_* = 2.7, 5.3, \infty$. The scaling of luminosity with Ω becomes shallower as the stars spin more rapidly. 118

5.22 Electromagnetic luminosity as a function of the semimajor axis of the neutron star orbits. The neutron stars are moving in a highly conducting plasma and are spinning rapidly at $\sim$ ms periods, with $R_{\mathrm{LC},*}/R_* = 2.7$. Curves are shown for a single star in orbit, an aligned binary, and an antialigned binary. Scaling of luminosity with Ω is significantly weaker than for nonspinning stars. 119

5.23 Electromagnetic luminosity as a function of inclination angle of the tilted star. The stars are not spinning, moving in vacuum, and have semimajor axis $r_{\mathrm{orb}}/R_* = 1.9$. Curves are shown for a single star in orbit (triangles) and an aligned binary (squares). Luminosity of the binary increases monotonically with inclination angle, but does not completely vanish at $\alpha = 0^\circ$ at this orbital separation. 121

5.24 Electromagnetic luminosity as a function of inclination angle of the tilted star. The stars are not spinning, moving in a highly conducting plasma, and have semimajor axis $r_{\rm orb}/R_* = 1.9$. Curves are shown for a single star in orbit (triangles) and an aligned binary (squares). Luminosity is much stronger in the binary due to the magnetic pressure that field lines from each star exert on field lines from the other. Luminosity increases with inclination angle as more field lines can cross to the opposite side of the magnetosphere and force field lines coming off the other star backwards toroidally. 122

5.25 Electromagnetic luminosity as a function of inclination angle of the tilted star. The stars are spinning rapidly at $\sim$ ms periods, with $R_{\rm LC,*}/R_* = 2.7$, moving in a highly conducting plasma, and have semimajor axis $r_{\rm orb}/R_* = 1.9$. Curves are shown for a single star in orbit (triangles) and an aligned binary (squares). The luminosity of the binary appears to be a simple sum of the luminosities of the stars orbiting individually. 123

5.26 Poynting flux as a function of polar angle and integrated over the azimuthal direction. The stars are not spinning, moving in a highly conducting plasma, and have semimajor axis $r_{\rm orb}/R_* = 1.9$. Curves are shown for different inclination angle of the tilted star. Radiation is preferentially beamed towards $\theta \sim 30^\circ, 150^\circ$ for aligned and antialigned dipoles, but asymmetrically beamed towards 150° when $\alpha = 45^\circ, 90^\circ$. 124

5.27 Poynting flux as a function of polar angle and integrated over the azimuthal direction. The stars are spinning rapidly at $\sim$ ms periods, with $R_{\rm LC,*}/R_* = 2.7$, moving in a highly conducting plasma, and have semimajor axis $r_{\rm orb}/R_* = 1.9$. Curves are shown for different inclination angle of the tilted star. Radiation is preferentially beamed towards angles near the equator for all inclination angles. 125

List of Tables

2.1 Maximum out-of-plane magnetic field values, normalized to the maximum vacuum value, for each panel from Figure 2.1. 25

5.1 Maximum out-of-plane magnetic field values, normalized to the field strength at the stellar surface, for Figures 5.1-5.10. 94